DOTTORATO DI RICERCA IN FISICA

XXVIII CICLO

SEDE AMMINISTRATIVA

UNIVERSITA DEGLI STUDI DI MODENA E REGGIO
EMILIA

Vibrational and optical fingerprints in graphene-based nanostructures

---

TESI PER IL CONSEGUIMENTO DEL TITOLO DI
DI DOTTORE DI RICERCA

Candidato:
Marzio DE CORATO

Relatori:
Prof. Alice RUINI
Dr. Deborah PREZZI

Coordinatore del dottorato e Direttore della scuola:
Prof. Marco AFFRONTE

To Erika

"Mind, the ruling power, persuaded necessity to bring the greater part of created things to perfection, and thus and after this manner in the beginning, through necessity made subject to reason, this universe was created"
Plato, Timaeus (Translated by Benjamin Jowett [105])

CONTENTS

INTRODUCTION

Quantization effects are widely used in materials science to modify the properties of a bulk material, making them size dependent. This approach has received much attention also in the graphene field, where graphene nanoribbons or quantum dots are produced by cutting this 2D layered material to form 1D nanostripes or 0D nanoflakes. Since their experimental realizations [39], these systems attracted an increasing interest, not only because at variance with graphene they are semiconductors, but also in view of their tunable band gap [120, 121, 39, 34, 32, 33, 31]. As detailed in Chapter 1, in addition to their width another key-feature governs the properties of these nanostructures, namely their edge morphology: to fully exploit such tuning potential it is thus important to produce structurally well-defined systems with atomically precise edges. In the literature this was efficiently obtained through bottom-up approaches, where nanoribbons are obtained from molecular precursors via chemical processes. This operation can be either cathalized by a metallic substrate [20] or performed by solution-mediated approaches [90, 89].

The latter method, that has the advantage to produce systems that are suitable for a further processing, opened two issues that were object of this thesis work: the first one concerns the role played by π-π coupling of the nanoribbons that are grown in solution in defining their properties; the second one concerns their characterization through the Raman and Infrared spectroscopies.

In addition to the production of isolated GNRs, one can confine 2D electrons also by periodically combining stripes of graphene with stripes of other 2D lattices such as hexagonal boron nitride (h-BN) or transition metal dichalcogenide (TDMC). This idea represent the 2D analogue of what was done in the past for layered superlattices of conventional semiconductors [85, 24]. So far the theoretical studies of such systems are limited only to their electronic properties [106, 143]: this leaves an opened issue concerning their vibrational properties.

The thesis is structured as follows: in the first part, I provide a bird eye view concerning the materials involved in this work as well as on the considered characterization and on the computational techniques, while the second part is devoted to the presentation of my original results. The first chapter contains an overview on the electronic and vibrational properties of the most common 2D lattices, such as graphene, h-BN and TDMC. In the second chapter, the theoretical background of the Raman scattering, UV-VIS and IR absorptions is briefly reviewed. The third chapter, that concludes the background section, is dedicated to an overview of the computational methods used in this thesis work: these include the Hatree-Fock (HF) method , as well as ab-initio density functional theory (DFT) and density functional perturbation theory (DFPT) approaches. In Chapter 4 we present the Raman and IR characterization of the GNRs, obtained in collaboration with different experimental groups: we explain the effects of the edge morphology and of the edge functionalization on the Raman and IR spectra. In chapter 5 we present our analysis of the effects of π-π coupling on the UV-VIS absorption spectrum for graphene nanoflakes. As we will show, this long-range interaction allows for the realizations of macromolecular systems whose optical properties can be tuned by properly choosing components and stacking. Finally in Chapter 6 we present the current developments of our ab-initio investigation on the vibrational properties of 2D superlattices: by now this analysis has been performed on two systems, composed by graphene and h-BN, that differ by the morphology of the interface.

Part I.

Background

1 GRAPHENE AND RELATED MATERIALS: FUNDAMENTAL PROPERTIES

The synthesis of 2D materials represents a very important step for the realization of materials on demand [48, 107, 59, 92, 19, 138]. Among them, the champion role is definitely played by graphene: this system has been object of a wide number of researches since 1947 [132] due to its interesting properties and possible applications [27, 48, 141, 7, 8, 119, 65]. Beside graphene, other 2D materials have drawn the attention of the scientific community, such as hexagonal boron-nitride (h-BN) [98, 138] and transition metal dichalogenides [29, 138]. In order to manipulate their physical properties, one can also consider to further reduce their dimensionality from 2D to 1D: this is the case of nanoribbons [39, 61]. Finally, it is also possible to combine these 2D lattices either as building block into a layered system [47], either in to a 2D superlattice where stripes of each 2D materials are combined in the same plane with a defined periodicity [111, 30]. The goal of the present chapter is to provide a bird-eye view on these low-dimensional materials: we will begin by presenting the main properties of graphene and related nanostructures, i.e. graphene nanoribbons and nanoflakes; after that, we will briefly introduce the main properties of other types of 2D systems: hexagonal boron nitride (h-BN) and transition metal dichalcogenides; finally we will review the main results concerning the coupling of these 2D lattices.

1.1 GRAPHENE

Graphene is nothing but a single layer of graphite, a well known material which is known since the 4th millennium B.C [38] .The first theoretical investigation of this 2D system was performed by Wallace [132]; his main focus, however, was the investigation of the properties of graphite for the realization of a nuclear reactor. At that time, in fact, it was commonly accepted that free-standing 2D systems could not exist because of their unstable structure: a paper wrote by Peierls and Landau [101, 72, 48] pointed out that, for every 2D material at any temperature, the vibrational fluctuations are comparable to interatomic distances, and this makes unstable every 2D lattice; however, in 2004 a single graphene layer was isolated (and characterized) from graphite by means of mechanical cleavage [48]. Theoretically it was pointed out that a 2D lattice can become stable in presence of corrugation [102, 41, 48, 64, 27]. It is worth noting that before 2004 several studies were performed on substrate supported monolayer graphite (see for example [5, 4, 88, 45, 97]).

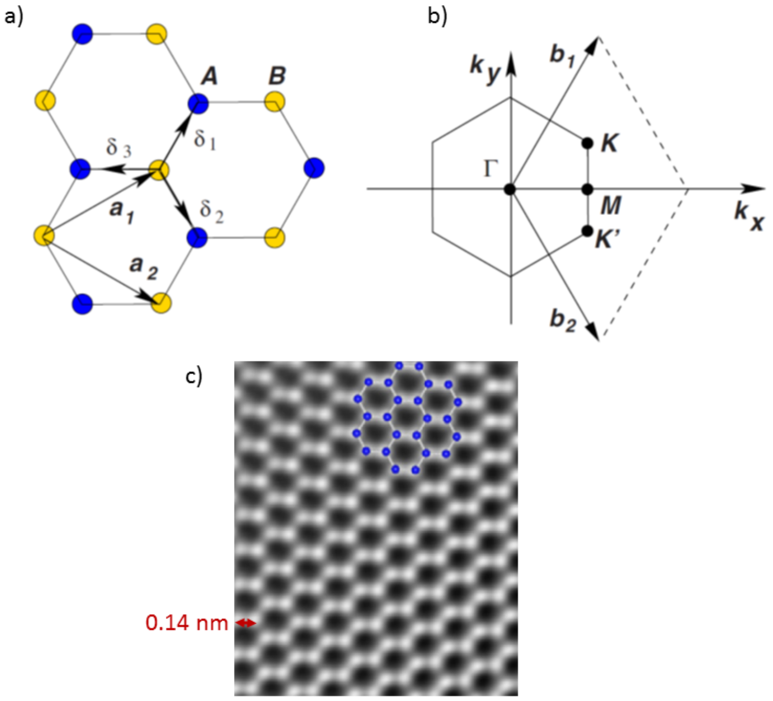

Figure 1.1.: The graphene lattice: a) the honeycomb structure as generated by the two lattice vectors in Eq. 1.1 b) the BZ of graphene; c) TEM image of graphene as grown on B_4C. The a) and b) images are taken from [27] while the c) image is taken from [93]

The geometry of the graphene lattice is illustrated in Fig 1.1 : its hexagonal lattice, with two atoms for unit cell, can be generated with the following vectors [27]

$$a_1 = \frac{a}{2}\left(3, \sqrt{3}\right) \quad a_1 = \frac{a}{2}\left(3, -\sqrt{3}\right) \tag{1.1}$$

where $a = 1.42$ Å is the interatomic distance; the corresponding reciprocal lattice vectors are [27]

$$b_1 = \frac{2\pi}{3a}\left(1, \sqrt{3}\right) \quad b_1 = \frac{2\pi}{3a}\left(1, -\sqrt{3}\right) \tag{1.2}$$

As demonstrated by Wallace, tight binding (TB) calculations of graphene electronic structure leed to the following relations: [27, 132]

$$E_{\pm}(\mathbf{k}) = \pm t\sqrt{3 + f(\mathbf{k})} - t'f(\mathbf{k}) \tag{1.3}$$

where [27, 132]

$$f(\mathbf{k}) = 2\cos\left(\sqrt{3}k_y a\right) + 4\cos\left(\frac{\sqrt{3}}{2}k_y a\right)\cos\left(\frac{3}{2}k_x a\right) \tag{1.4}$$

t is nearest neighbour hopping energy and t' the next nearest neighbour hopping energy. If we consider the BZ region near $\mathbf{K}$[27]

$$\mathbf{k} = \mathbf{K} + \mathbf{q} \quad |\mathbf{q}| << |\mathbf{K}| \tag{1.5}$$

the expression 1.3 can be simplified as [27]

$$E_{\pm}(\mathbf{q}) = \pm v_F|\mathbf{q}| + O\left[(q/K)^2\right] \tag{1.6}$$

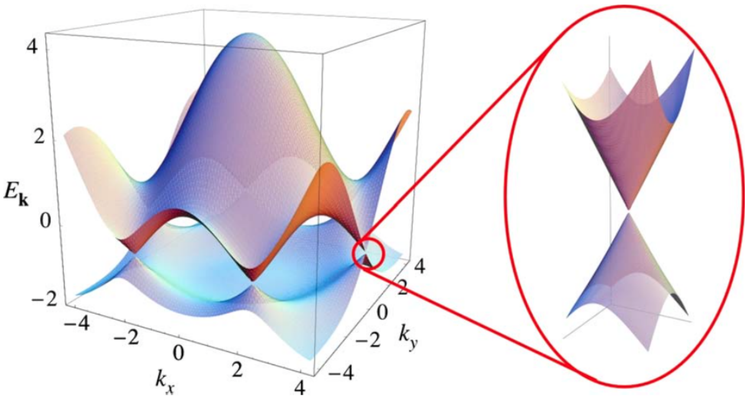

Figure 1.2.: Calculation of the electronic band structure of graphene according to the TB approach. Image taken from Ref. [27]

where the Fermi velocity is $v_f \simeq 1 \cdot 10^6 m/s$. A plot for $t = 2.7$ eV and $t' = -0.2t$ [27] is reported in Fig 1.2. The Eq. 1.6 describes a linear dispersion near **K** and **K′** points which forms the so called *Dirac-cones*. A similar approach can be used to analyse the electronic structure of a bilayer and, in general for a n-layer system: this work was performed by Partoens and Peeters in [99], and their results are reported in Fig 1.3

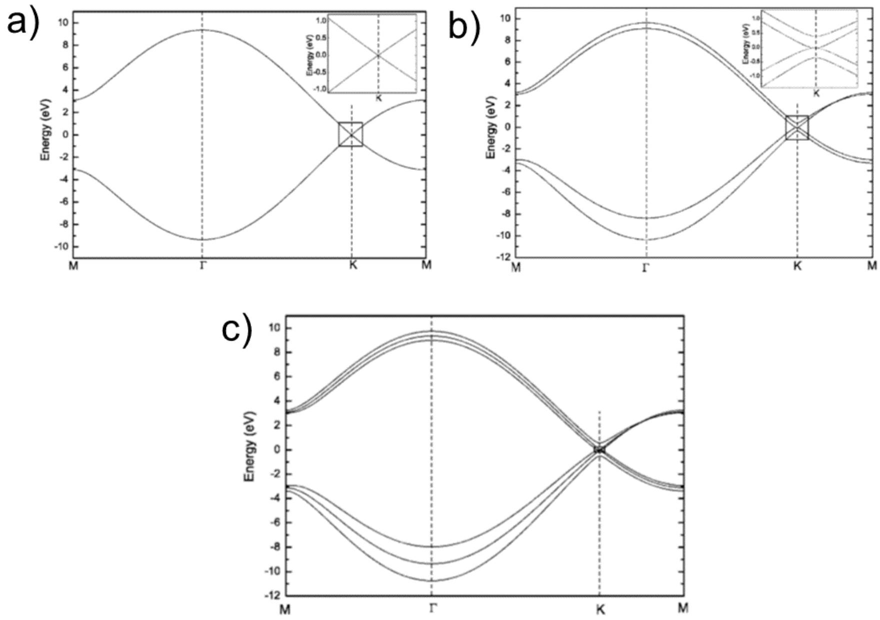

Figure 1.3.: Evolution of the electronic band structure for a single (a), bilayer (b) and trilayer (c) graphene system (with Bernal stacking) within the TB formalism. All images are taken from [99]

As for the electronic properties, also the vibrational properties of graphite and graphene have drawn a great interest [36, 12, 135, 4, 5, 117, 140, 84]

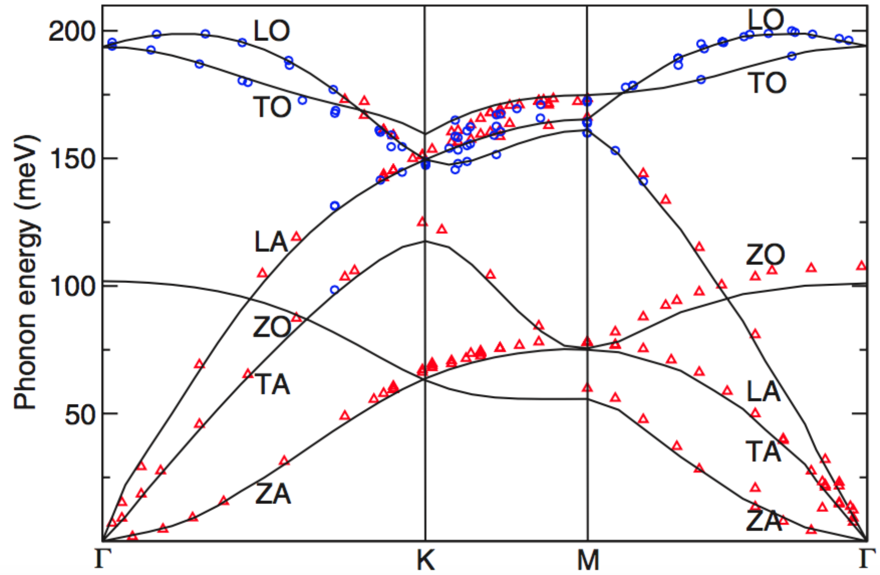

Figure 1.4.: Investigation of the phonon dispersion of graphite as performed by Mohr et al.: the symbols represent the data obtained with x-ray measurements while the solid lines is the dispersion obtained through ab-initio calculations [82]. Image taken from [84]

As it can be noted in Fig 1.4, the dispersion of graphite is characterized by six phonon branches, 3 acoustic and 3 optical ones. The acoustic modes at Γ correspond to displacements in which all atoms move in the same direction; in the optical modes, adjacent atoms have opposite displacement vectors. The three acoustic modes are usually classified as *logitudinal acoustic* (LA), where the displacement has the same direction of the wavevector **q**, *transverse acoustic* (TA), the direction of the displacement is perpendicular to the wavevector **q**, and *Z acoustic* (ZA) where the displacement is perpendicular to the LA-TA plane; in the same way, the optical modes will be classified as *logitudinal optic* LO, *transversal optic* TO and *zeta optic* ZO (see Fig. 1.4).

Looking to the LO bands near Γ, we note that a discontinuity in the curvature is present; a similar behaviour can be found also around **K** for TO bands (see Fig 1.6). Those discontinuities are know as Kohn anomalies [66] and can be found for each vibrational mode with wavevector **q** which satisfy the

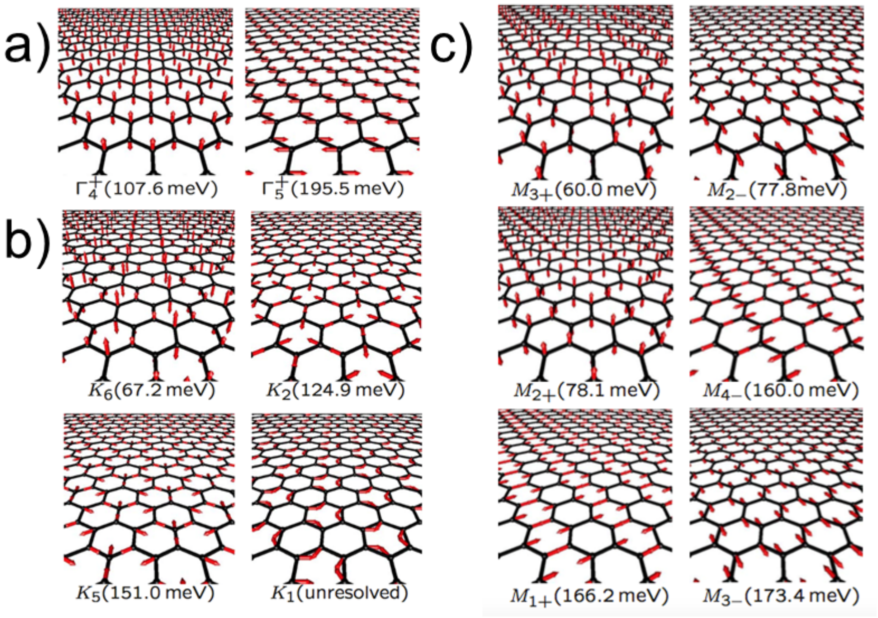

Figure 1.5.: The modes of graphene at Γ (panel a), at **K** (panel b) and at **M** (panel c) accompanied by their energy according to IXS experimental values. Images taken from [84]

relation $\mathbf{k}_2 = \mathbf{k}_1 + \mathbf{q}$, where $\mathbf{k}_1$ and $\mathbf{k}_2$ are two points of the Fermi surface: for these modes, an abrupt variation of the electron screening is found and this produces the typical kink of a Kohn anomaly in the phonon dispersion [66, 81]. In graphene, two equivalent states at **K** and **K'**$(= 2\mathbf{K})$ lie on Fermi surface [104]. As a consequence, there are two ways by which one can connect them: the first one gives $\mathbf{q} = \Gamma$ $(\mathbf{K} - \mathbf{K} = 0 = \Gamma)$ while the second one gives $\mathbf{q} = \mathbf{K}$ $(\mathbf{K'} - \mathbf{K} = 2\mathbf{K} - \mathbf{K} = \mathbf{K})$. Near these two **q** points, as pointed out by Piscanec et al. [104], one can use a linear fit (see also Fig 1.6) :

$$\begin{aligned} \hbar\omega_q &= \alpha_\Gamma q + \hbar\omega_\Gamma + O(q^2) \quad q \simeq 0 \\ \hbar\omega_q &= \alpha_K q + \hbar\omega_K + O(q^2) \quad q \simeq K \end{aligned} \tag{1.7}$$

where $\alpha_\Gamma = 397\ \mathrm{cm}^-1$ and $\alpha_K = 973\ \mathrm{cm}^-1$

A correct evaluation of the slope near **K** is widely used to extract the electron-phonon coupling in graphene [104].

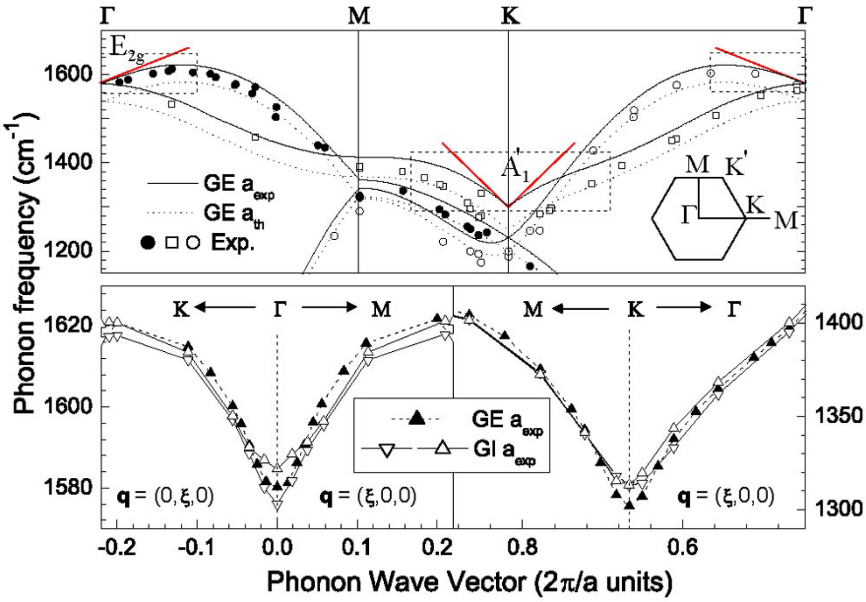

Figure 1.6.: Theoretical calculation of the slope (red lines) near the Kohn anomalies at Γ and **K** in graphene. The solid lines represent the calculated dispersion with DFPT perfomed by Pisanec et al. [104] while the point are the experimental data provided by Maultzsch et al. in [82]. Image taken from [104]

RAMAN FEATURES Raman spectroscopy is one of the most widely used characterization tools for graphene giving a large amount of information in a fast and non destructing way [43, 63]. In this paragraph, we briefly overview the origin of the most relevant Raman peaks of graphene. As shown in Fig. 1.7 only four peaks are present in a defect-free sample. These are the G, 2D, 2D′, and the D+D″ peaks. When defects are introduced, further peaks appear: these are the D peak, the D′ peak and the D′+D peak.

The G peak ($\sim$ 1580 cm^{-1} [42]) is well known to come from the LO and TO modes at Γ, as previously discussed; the D peak ($\sim$ 1350 cm^{-1} [42]), on the contrary, was object of a very long debate since 1970 [127, 131]. Among the different proposed theories, the currently accepted one is that of Thompsen et al. [126] which attribute this peak to the *inter-valley Raman scattering* : in this process, schematically shown in panel I of Fig. 1.8, an electron, that is excited from the valence band to the conduction band by an incoming photon, is scattered to the other valley through a phonon of momentum $\mathbf{K}$; the presence of defects allows the electron to be scattered back and a photon is emitted. Concerning the D peak, the involved phonon comes from the TO band that has a Kohn anomaly in $\mathbf{K}$ (see panel II of Fig 1.8): this explains the strongly dispersive behaviour of the D peak (see the panel III of Fig. 1.8). On the other hand the D′ peak ($\sim$ 1620 cm^{-1} [21]) is produced by the *intra-valley Raman scattering* in which the excited electron is scattered within the same valley: in this case the involved phonon will have momentum close to Γ. A full description of the different scatterings involved in these processes can be found in [130].

In the previously described processes, only one phonon is involved; however, as one considers the two-phonon scattering, further processes are allowed: this is the case of the 2D ($\sim$ 2700 cm^{-1} [42]) and 2D′ peaks ($\sim$ 3200 cm^{-1} [21]) that are, respectively, the overtones of the D and D′ peaks. The fact that these last modes are overtones explains why they are present also in a pure graphene: in fact two phonons of opposite momenta are involved and no defect is required. On the other hand, the D+D″($\sim$ 2450 cm^{-1} [43]) is given by a scattering that involves a phonon near $\mathbf{K}$ from LA and LO branches [43] (see panel II of Fig. 1.8). Finally, in the same process an intervalley and an intravalley transition can combine together: this is the case of D+D′ peak ($\sim$ 2940 cm^{-1} [21]) (see panel I of Fig. 1.8).

Once we have briefly reviewed the nature of these peaks, we can discuss how they can be used to fingerprint the properties of the sample. The G peak is a marker of the sp^2 carbon hybridization: if a strained system is considered, as done in Ref. [71], this peak blueshifts or redshfits in the case of a shorter or larger lattice parameter. Furthermore it is useful to point out that, for a system with an identical lattice, such as the hexagonal boron nitride (h-BN), this peak is still present, although it has a lower energy (1366 cm^{-1} [55]). The D peak fingerprints the presence of defects: as the defect concentration increases, the peak intensity and the broadening increase [79] (see the panel a) of Fig 1.9). In addition to localized defects, the presence of edge represent another way to break the momentum conservation rule in graphene; however, in this case the activation of D peak is strictly dependent on the edge morphology: as shown in panel b) of Fig. 1.9, the phonon momentum $\mathbf{K}$ is allowed when an armchair edge is considered: as a consequence, the D peak will be present in the Raman spectrum; on the other hand, when a zig-zag edge is considered, this momentum is not allowed and so no D peak will be present [22]. This behaviour can thus be used to discriminate between different edge orientations [26, 22, 63]. Finally, as shown in panel c) of Fig 1.9, the 2D peak can be used to fingeprint the number of graphene sheets in a multi-layer system due to the changes in the electronic bands structure [42]. An example concerning bilayer graphene is reported in Fig 1.10. We conclude this paragraph by pointing out that, while the peaks previously discussed for the characterization of a graphitic sample concern displacements that involve only a single plane, there are also other modes that can be used to fingerprint the properties of multilayers. For example the *shear mode* (C), whose displacement is reported in Fig. 1.11, produces a Raman peak whose energy is blueshifted, when the number of graphene layers N is increased according to the expression [122, 43] :

$$\mathrm{Pos}(C)_N = \sqrt{\frac{2\alpha}{\mu}}\sqrt{1+\cos\frac{\pi}{N}} \tag{1.8}$$

where $\alpha = 12.8 \times 10^{18} N \quad m^{-3}$ is the interlayer coupling and $\mu = 7.6 \times 10^{-27} kg \quad A^{-2}$ is the graphene mass for unit area [43, 122].

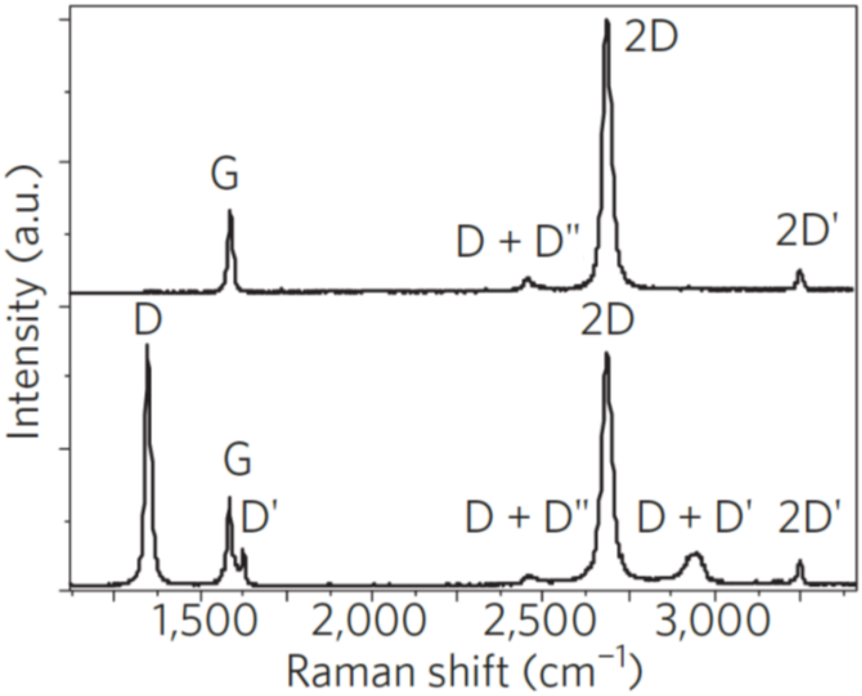

Figure 1.7.: Comparison between the Raman spectrum of a pure (up) and defected (bottom) graphene samples. The image is taken from [43]

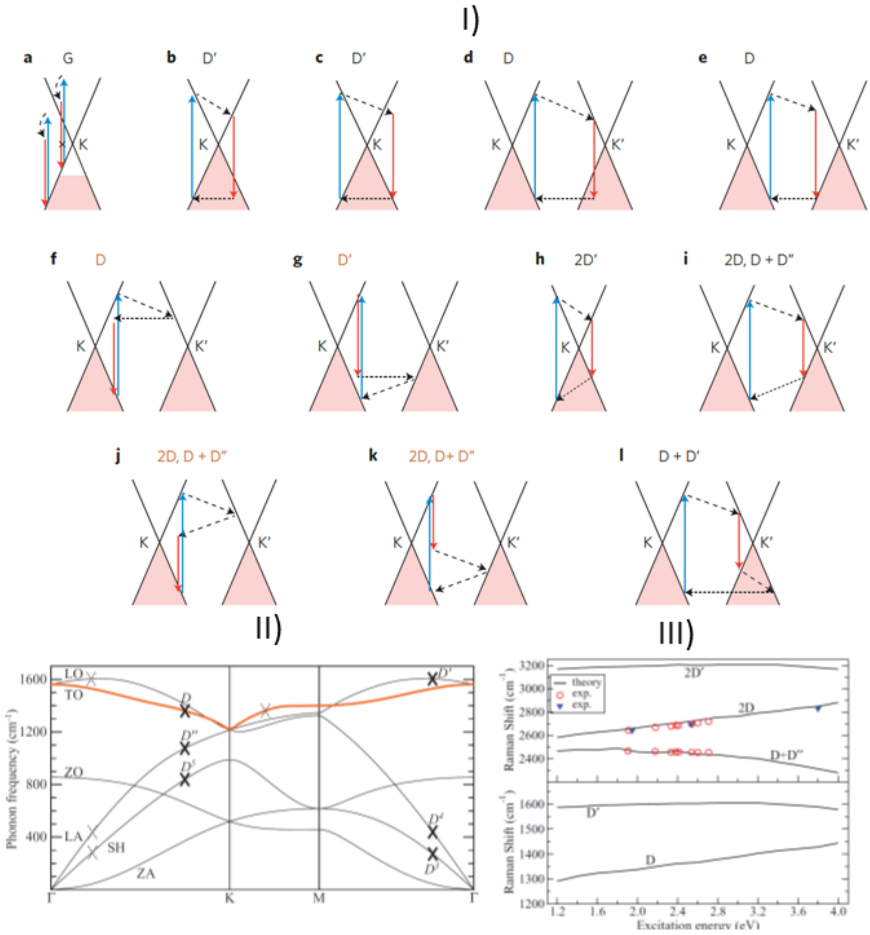

Figure 1.8.: The diagrams of the processes that produce the Raman peaks of graphene shown in Fig 1.7 (panel I), compared with its phonon dispersion (panel II) and with the peaks behaviour as the energy of the incident beam is changed (panel III). In this last panel, the solid lines represent the theoretical dispersion calculated by Venezuela et al. in [130], while the circle and the triangle refer respectively to the experimental data of Mafra et al. [80] and Cong et al.[35]. The blue/red solid lines of panel I) stand respectively for a phonon absorption/emission, while the dashed lines stand for a phonon absorption from the branch reported in panel II); the labels marked in orange in panel I stand for a process that has a lower contribution to the peak with respect to the ones marked in black. The image in panel I) is taken from [43], while the images in panels II and III are taken from [130]

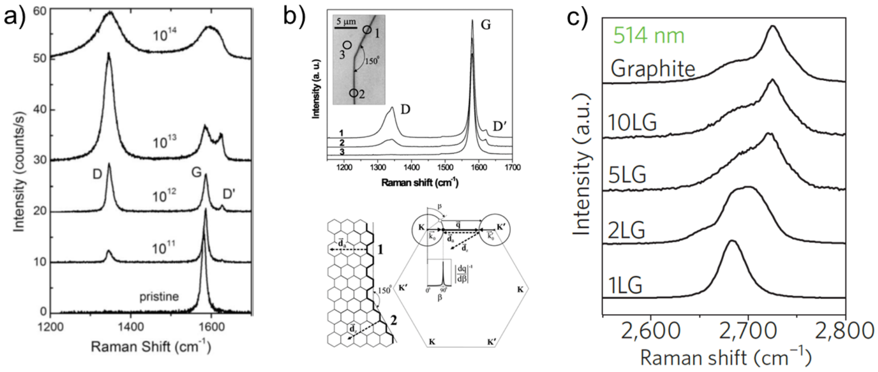

Figure 1.9.: The evolution of the Raman spectrum of graphene as different conditions of the sample are considered. Panel a) reports the experimental investigation of Lucchese et al. of a graphene sheet on a SiO_2 substrate submitted to a Ar^+ bombardment with different intensities (the number reported is in units of Ar^+/cm^{-1}): as the intensity of the bombardment increases the D peak grows. Panel b) reports the Cancado et al. experimental investigation on the Raman spectrum of a graphene sample near the edges: as one can see, for the zig-zag edge no D peak is produced since in the BZ the momentum $\mathbf{K}$ is not allowed; on the contrary for an armchair edge this peak is present due to the different BZ. Panel c) shows the Ferrari et al. investigation on the variation of the 2D peak as a graphene system with a different number of layers is considered (1LG refers to a monolayer graphene, 2LG to a bilayer graphene and so on). Image a) is taken from [79], image b) is taken from [22] and image c) is taken from [43]

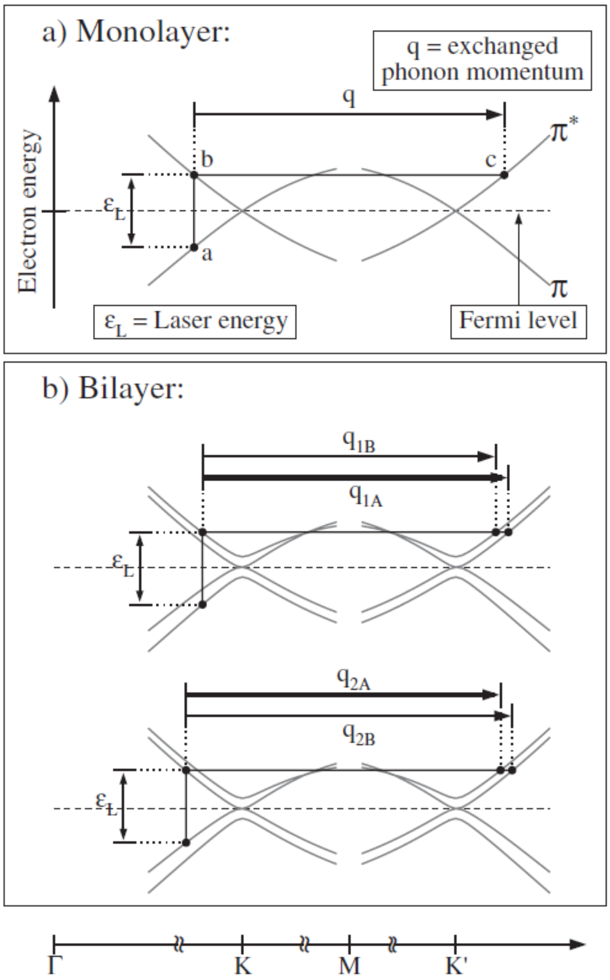

Figure 1.10.: Intervalley scattering for a monolayer (upper panel) and a bilayer graphene (lower panel): as the second layer is introduced the electronic bands split; since the phonon involved in the intervalley scattering can have a slightly different momentum four different 2D subpeaks are produced. The overall effect is a broadening of the 2D peak. Image taken from [42]

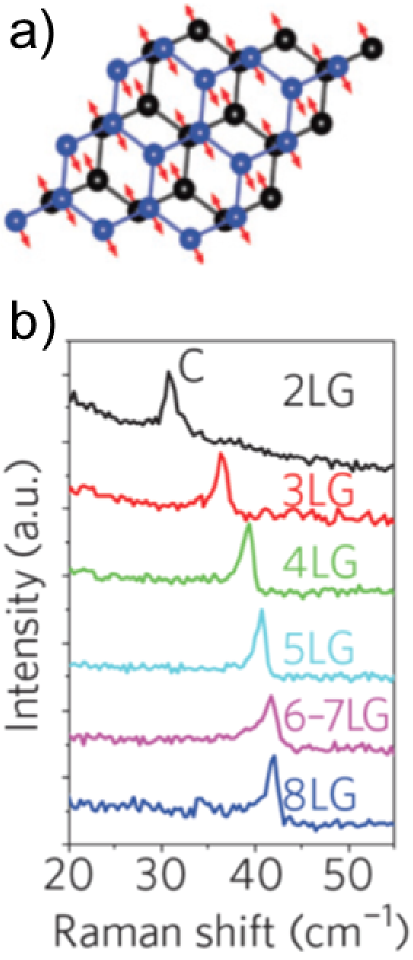

Figure 1.11.: The analysis of the shear mode displacement of a bilayer graphene (upper panel) accompanied the Ferrari et al. investigation on its Raman peak as a larger number of layers is considered (lower panel). Image a) is taken from [122] while imagine b) is taken from [43]

1.2 GRAPHENE NANORIBBONS

The metallic behaviour of graphene represents a weak point in view of possible applications for microelectronic and optoelectronic devices [115, 7]. One option to overcome to this limitation is to use the quantum confinement to induce a band gap opening: this is the idea of graphene nanoribbons (GNRs) which are 1D stripes obtained by cutting the 2D lattice along a given direction. As one can imagine, the physical properties of these systems are strictly correlated to the cutting direction. We will first focus on the geometry of these nanostructures, and then we will review their electronic and vibrational properties; finally, we will describe some of their most promising fabrication routes.

GEOMETRY The structural properties of the nanoribbons are fixed by their width and by their edge morphology. Concerning the latter, it is useful to define, in analogy with the carbon nanotubes, the following vector [113] :

$$\mathbf{C}_h = m\mathbf{a}_1 + n\mathbf{a}_2 \tag{1.9}$$

where $\mathbf{a}_1$ and $\mathbf{a}_2$ stands for lattice vectors of graphene, while m and n are integers. The $\mathbf{C}_h$ defines an ideal cutting line that can produce different edges: the (n, n) direction gives an armchair edge, the $(n, 0)$ direction gives a zig-zag edge and the (m, n) direction gives an hybrid edge (see Fig. 1.12). Once defined the edge morphology, in order to unequivocally define the structure of a nanorribon, it is necessary to fix the distance between its edges, also called width. Concerning an armchair nanoribbon, the latter is fixed by the number of dimeric lines across the ribbon width, while for a zig-zag nanoribbon this distance is measured in units of zig-zag chains [120]. Moreover, as shown in Fig 1.13, one can also consider other 1D lattices which can not be obtained by two lines along high-symmetry directions.

ELECTRONIC PROPERTIES OF GNRS As for graphene, the electronic structure of GNRs can be predicted by using TB approaches [17]. The starting point is that, within a TB formalism, the electronic band structures near the **K** and the **K′** reciprocal lattice points have a linear behaviour; as a consequence, one

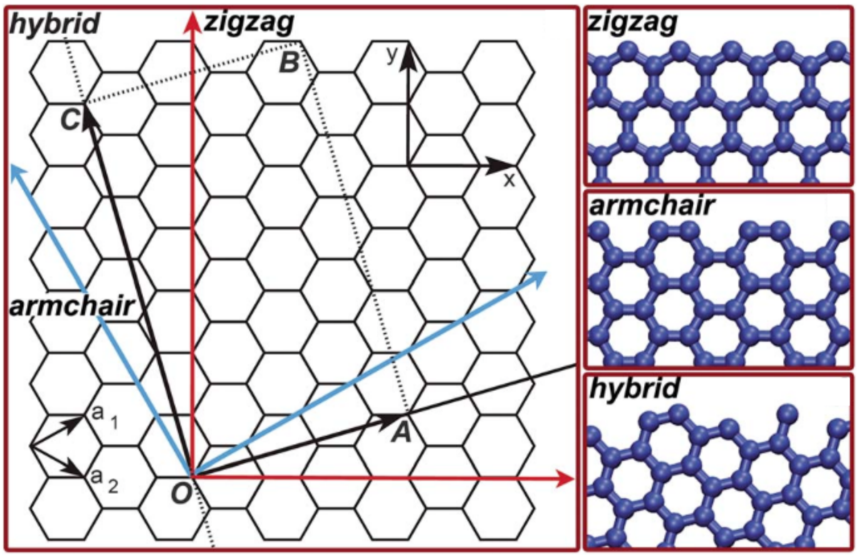

Figure 1.12.: Left panel: The zig-zag line vs the armchair line in the graphene lattices. Right panel: The GNR generated by cutting the graphene on these two lines are showed in the right panel. Image taken from [144]

can write the wave function of graphene near these two points as eigenstates of the Dirac equation [17]

$$\begin{aligned} H\Psi =& \varepsilon\Psi \\ H =& \gamma a_0 \begin{pmatrix} 0 & -k_x + ik_y & 0 & 0 \\ -k_x - ik_y & 0 & 0 & 0 \\ 0 & 0 & 0 & k_x + ik_y \\ 0 & 0 & k_x - ik_y & 0 \end{pmatrix} \\ \gamma =& \sqrt(3)t/2 \end{aligned} \quad (1.10)$$

where t is the hopping parameter, as previously illustrated. According to Ref. [37], the wavefunctions at $\mathbf{k} = \mathbf{K} + \overline{\kappa}$ can be written as the superposition of two periodic wavefunctions, which are respectively localized on one of the two atoms (A,B) of the unitary cell [37]:

$$\psi(\mathbf{k}, \mathbf{r}) = f_1(\overline{\kappa})\, e^{i\overline{\kappa}\mathbf{r}} \phi_A + f_2(\overline{\kappa})\, e^{i\overline{\kappa}\mathbf{r}} \phi_B \quad (1.11)$$

Finally, the electronic band structures of ZGNRs and AGNRs are obtained by imposing the appropriate boundary conditions of the edges (see Fig. 1.14). However, this simple approach incorrectly predicts that all ZGNRs and some AGNR are metallic. As pointed out by Son et al. in 2006 [121], this is due to

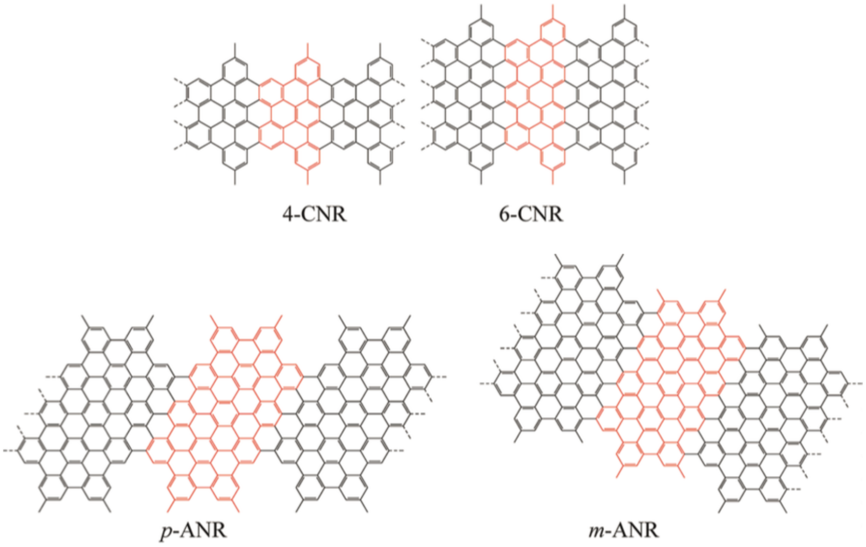

Figure 1.13.: GNRs which can not be obtained by performing two parallel cuts as for the ZGNR and AGNR lattices. Image taken from Ref. [96]

the fact that, in the first case, the spin degree of freedom was not considered, while, in the second case, the parameters of the TB for the edge atoms have to be different with respect to the bulk ones [120]. Here we will briefly review the main results for these two classes of systems [17, 121, 120].

ZGNR In this case, the TB electronic band structure has the form reported in Fig. 1.15. As one can note, a degenerate ground state at Fermi level is present: this situation is very similar to the case of a monoatomic linear chain in which the bonds are all equal. It is well known that in this case the system lowers its energy by introducing an alternation of the bonds lengths: with this new configuration the degeneracy is removed. In the ZGNR the degeneracy is removed, instead of by the bond alternation, by the spin alternation; however in order to see this effect the spin degree of freedom has to be introduced. This was done by Son et al. [120, 121]; by considering a spin resolved ZGNR, they found that the ground state of this system is magnetic and then that the antiferromagnetic configuration is favoured with respect to the ferromagnetic case. This last consideration could be also achieved by considering the Lieb theorem which states that a system described by the Hubbard

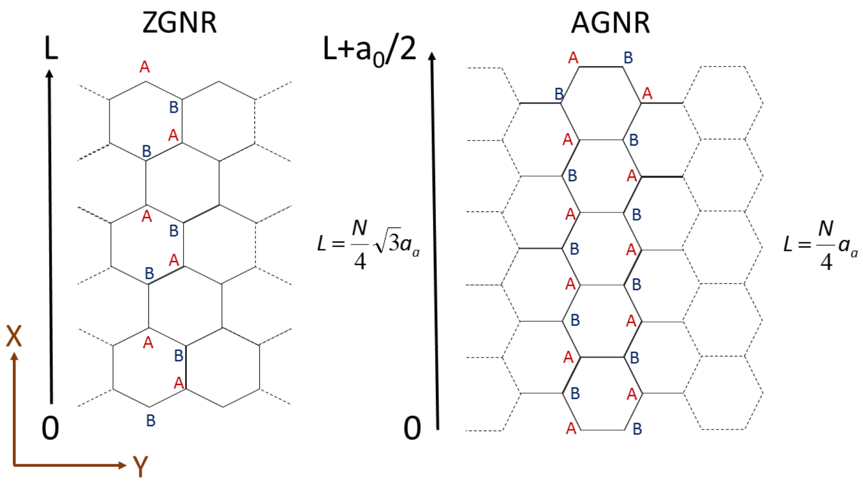

Figure 1.14.: A schematic view of the different boundary conditions which have to be imposed on the wavefuntions of GNRs: in the ZGNR case the wavefunction ϕ_A has to be null at L while ϕ_B has to vanish at 0; in the AGNR the wave function must be null for ϕ_A and ϕ_B at 0 and at $L + a_0/2$

hamiltonian, in which a bipartite lattice is present, has a non-degerate ground state with total spin given by the following relationship [76, 124]

$$S_{tot} = ||A| - |B|| \tag{1.12}$$

where A and B indicate the number of sublattices of type A and type B. As reported in Fig. 1.16, since the degeneracy close to the Fermi energy is removed, a gap is opened whose amplitude is inversely proportional to the nanoribbon width [121]. Furthermore, Son et al. [121] showed that the gap of the ZGNRs can be even closed by applying an electric field in the direction perpendicular to the GNR axis (see Fig 1.16): the electric field shifts the bands of the two spins in two opposite directions, making the system half-metallic .

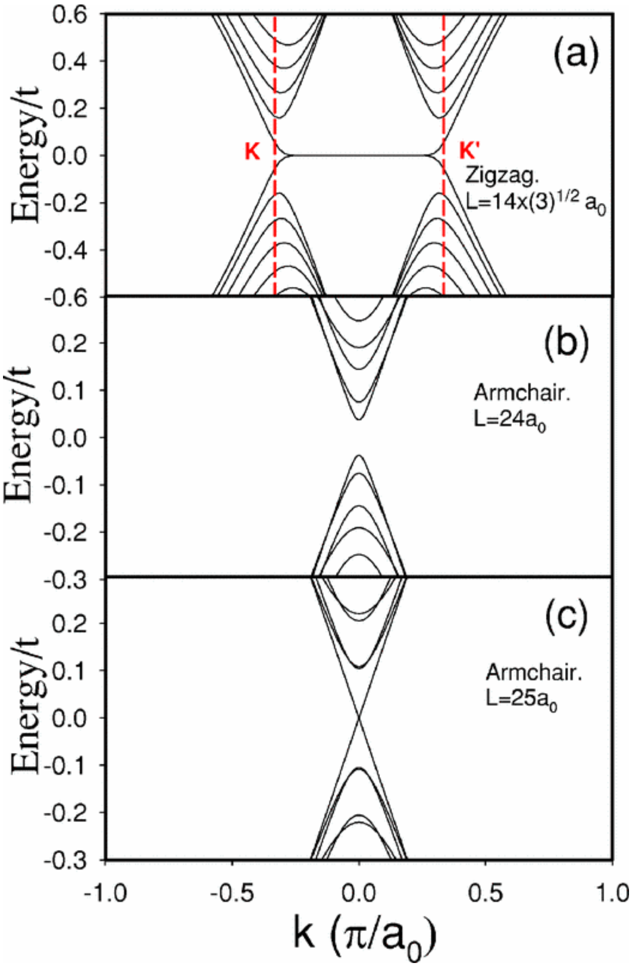

Figure 1.15.: Tight binding investigation of the electronic bands of ZGNR a) and AGNR b) and c). Note that according to their approach a metallic behaviour is predicted for ZGNR and for AGNR whose width is equal to $L = (3M + 1)a_0$ where M is an integer. Image taken from [17]

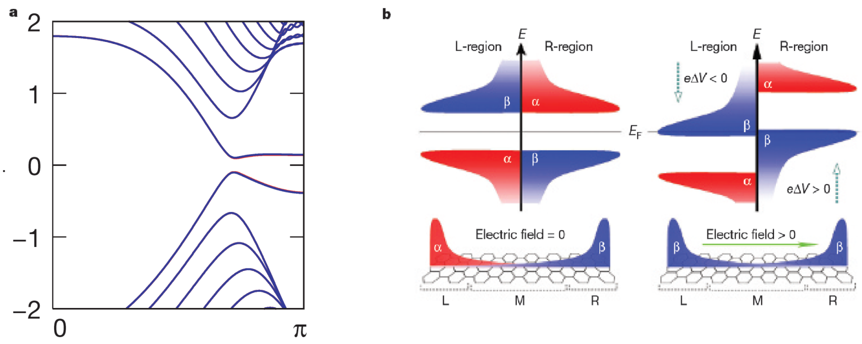

Figure 1.16.: Spin polarized investigation on the electronic properties of a 16ZGNR: a) the band structures b) effect induced by the application of an electric field. Image taken from [121]

AGNR In this case the Brey et al. [17] TB calculations show that for a AGNR that satisfies the relation $N_a = 3p + 2$ (being p an integer) a metallic behaviour is found. Later, Son et al. in [120] calculated the electronic structure of this system with DFT and they found that all the AGNR families have a finite gap: the weak point of the tight binding prediction for AGNR lies in the fact that the carbon-carbon bonds at the edges are different with respect to the ones at the core of the GNR (see 1.17). A good agreement with DFT data can be obtained, as shown in Ref. [120], with a TB hamiltonian in which a different parametrization for the edge carbon atoms is considered. It is worth noting that, as shown in Fig 1.17, also in this case the electronic band gap is inversely proportional to the width, but, differently to the zig-zag case, an oscillating behaviour within the three families $L_1 = 3Ma_0$, $L_2 = (3M+1)a_0$ and $L_3 = (3M+2)a_0$, is present.

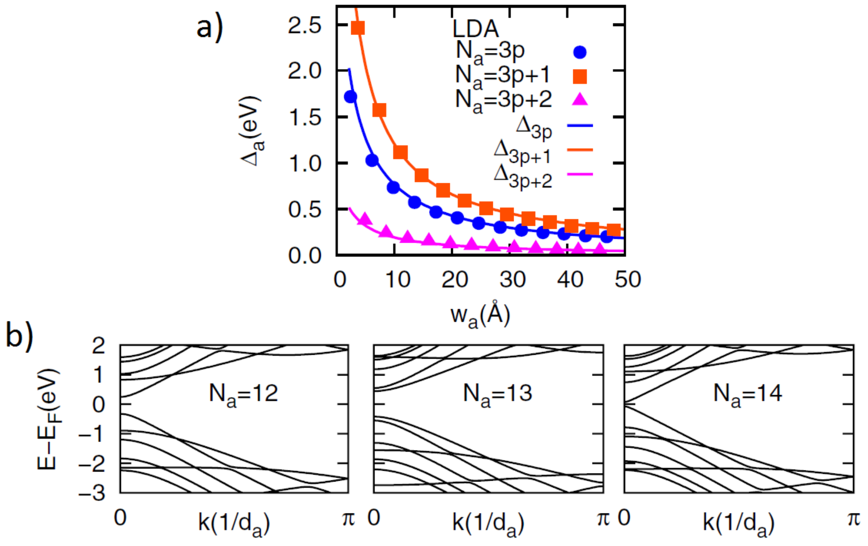

Figure 1.17.: LDA investigation of the electronic properties of the AGNR systems: a) the band gap of the three different families of AGNR b) the band structures of a three different GNRs. Images taken from [120]

VIBRATIONAL PROPERTIES OF GNRS As for the electronic properties, the lattice dynamics of a GNR is characterized by the confined wavefunctions, which will now describe the effect of the confinement on the motion of the nuclei. For a system confined in a particular direction, the wave-vector of a vibration must respect the well-know relation of a standing wave [53]

$$\begin{aligned} k_{\perp,n} \cdot w_{\text{ribbon}} &= n\pi \\ k_{\perp,n} &= \frac{\pi}{w_{\text{ribbon}}} n \end{aligned} \tag{1.13}$$

where $k_\perp$ is the component of wave-vector k along the confined direction, and n is an integer. In the realm of GNR vibrations, there are three classes of modes: the C-H modes, the fundamental C-C modes, and the overtone modes. The C-H modes involve the H atoms that passivate the C atoms of the edge: these vibrations are independent from the nanoribbon width but some of them are strongly correlated to the nanoribbon edge morphology [28]. The fundamental C-C modes, which can be acoustic or optical, can be seen as the fundamental modes of a infinite potential well where no nodes are present. Following this analogy, one can have also the excited states, which are called the hypertones, in which the nodes are present (see Fig 1.18); for GNRs, their number is fixed by the width of the system: for a N-AGNR/ZGNR, $3(N-1)$ acoustic and optical overtones are expected (the factor 3 is due to the dimensionality of the space while the -1 term is due to the presence of the fundamental mode).

It can be shown that, in a confined system, the frequency of a confined mode at Γ is given by the following expression [85]

$$\begin{aligned} \omega_m &= \omega_{\text{bulk}}(q_m) \\ q_m &= \frac{m\pi}{d_a} \end{aligned} \tag{1.14}$$

where d_a is the width of system along the confinement direction, m an integer and q_m the wavevector. With this so called Zone-Folding (ZF) approach, one can in principle reproduce the whole vibrational spectrum at Γ for a confined system once the bulk dispersion is known. We have to stress the fact that here we assume that the confined system is in vacuum: if the confinement is obtained with other materials (superlattices) this ZF approach is valid only for optical modes, since, usually, the acoustic modes are not confined (see [85, 24]).

As one can point out from Fig 1.19, the confinement directions for AGNRs and ZGNRs are different also in the recipro-

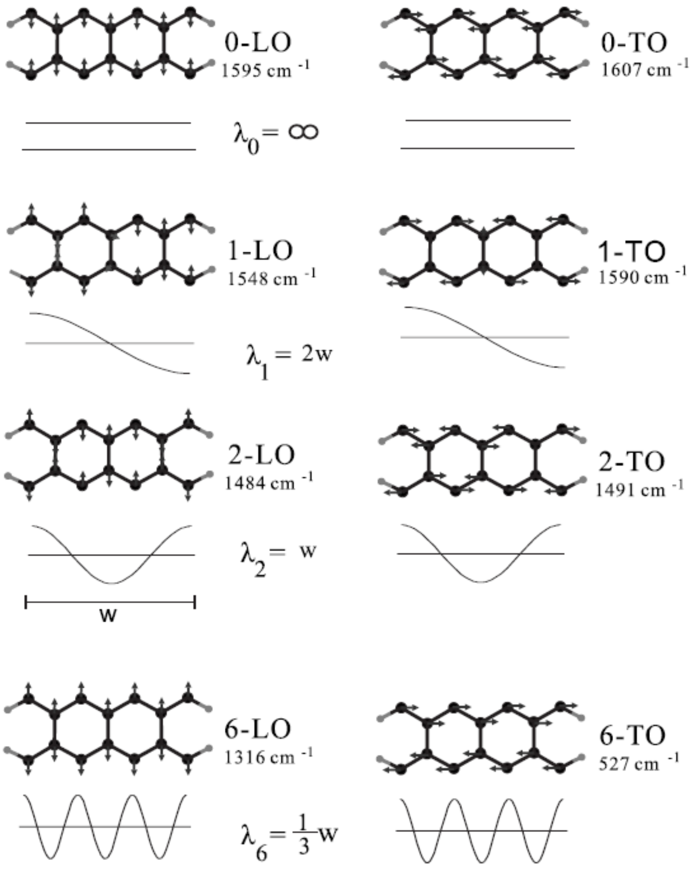

Figure 1.18.: The fundamental longitudinal and transversal optical modes (respectivly 0-LO and 0-TO) of 7AGNR accompanied by their overtone modes. Note that the number of the phase changes (nodes) defines the number of the overtone mode. Image taken from Ref. [53]

cal space: $\overline{\Gamma K M}$ for AGNRs and $\overline{\Gamma M}$ for ZGNRs. Consequently, the whole BZ of graphene is needed in order to describe the vibrational spectrum at $q = 0$ for AGNRs, while only the $\overline{\Gamma M}$ direction is required for ZGNRs. In Fig 1.20 the frequencies of 15-AGNRs and of 8-ZGNR calculated from first principles are folded on the vibrational band structure of graphene: as it can be noted an excellent agreement is found.

RAMAN FEATURES Previously, we showed that the two key properties of a GNR which shape its electronic band structure are the edge morphology and the width: we are now going to discuss how both these features can be fingerprinted through the Raman spectroscopy.

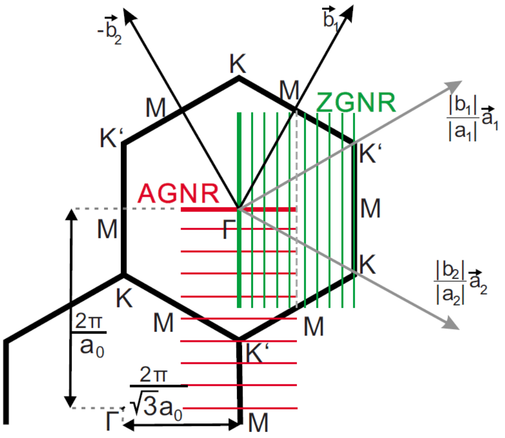

Figure 1.19.: The BZ of 10ZGNR (green) and of 10AGNR (green). Image taken from [53]

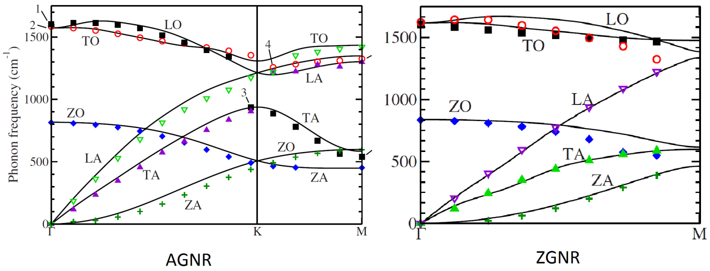

Figure 1.20.: The frequency of vibrations at Γ of 15AGNR (left panel) and of 8ZGNR folded on the graphene dispersion as done by Gillen et al. Images taken from [53]

Width As one expects, in analogy with the levels of an infinite quantum well, the frequency of the transverse acoustic modes reported in Fig 1.18 is strictly connected to the width of the GNR. Among all the transverse acoustic overtones, the first one, known as the *radial like breathing mode* (RLBM) in analogy with the *radial breathing mode* of the carbon nanotube [63], has the highest Raman intensity with respect to the higher transverse acoustic overtones. Now, looking to the shapes of the TA branches in Fig. 1.21, it can be pointed out that these are linear near Γ; moreover the slope of these branches is well known (the speed of sound in graphene). Since the RLBM folds on these branches according to the expression 1.14, a linear relation can be achieved for a GNR with a sufficiently large width (see Fig. 1.21) [52]:

$$\omega_{\text{RLBM}} = \frac{\alpha\pi}{w} \tag{1.15}$$

where a is the speed of sound in graphene. This approach, first proposed by Yamada et a et al. [139] and then by Gillen et al. in [52, 51], allows to easily fingerprint the width of a GNR through the frequency of this peak.

Edge morphology In the previous section we showed that the morphology of graphene edges can be fingerprinted through the presence of the D peak in the Raman spectrum due to the different BZ of armchair and zig-zag edges. Here we remark that this argument can be also applied for the probing of the edges of a GNR [51] .

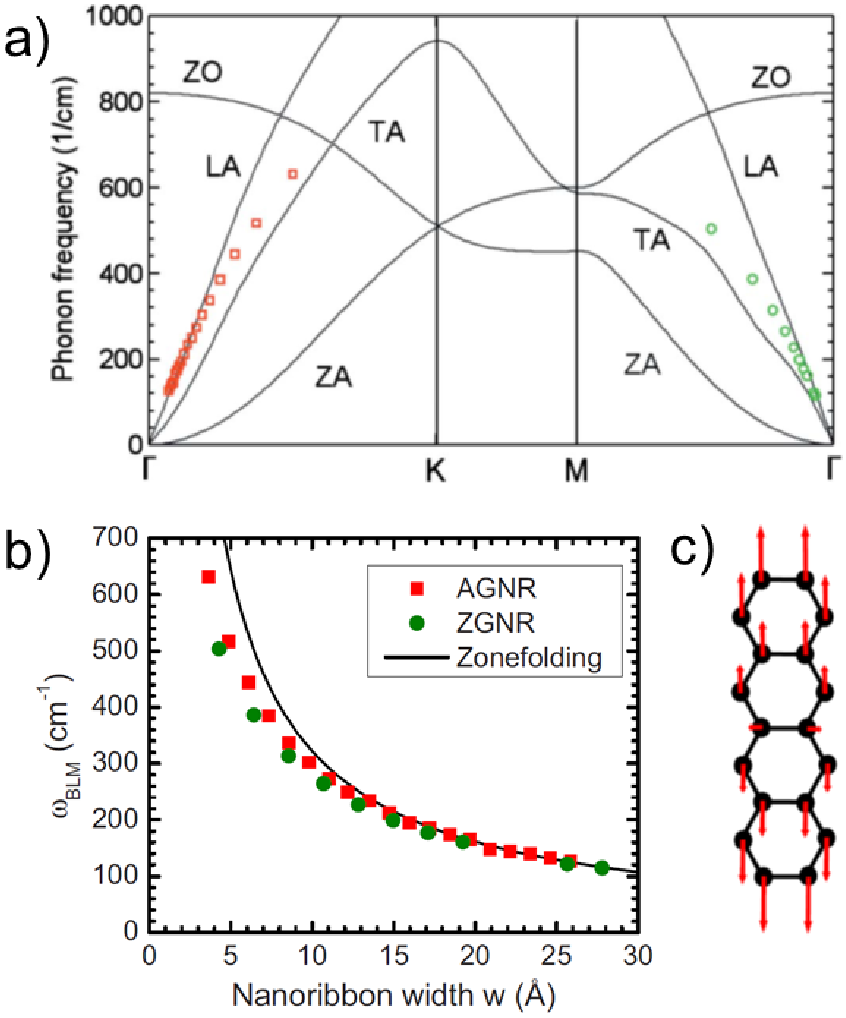

Figure 1.21.: Theoretical investigation on the relation between the frequency of the RLBM and the width of AGNRs and ZGNRs: a) the frequency of the RLBM of GNR with different width folded on the linear braches of graphene; b) the zonefolding relation 1.15 (solid line) vs the RLBM of AGNRs and ZGNRs with different widths calculated through ab-initio methods (points); c) the displacement of the RLBM for an AGNR. All images are taken from [52]

FABRICATION/PRODUCTION TECHNIQUES Before concluding this section, we want to mention the most important fabrication techniques of GNRs. These can be subdivided in two classes: the top-down approaches, where one obtains the GNR by cutting down another graphitic structure, such as a nanotube or a graphene sheet, and the bottom-up approaches, in which the GNRs are chemically grown starting from a molecular seed. In the realm of top-down methods, an important role is played by the lithography and by the nanotube unzipping: in the first case a template is put on a graphene sheet, then the overall system is etched with plasma[134]; this process leaves only the portions covered with the template(see Fig 1.22); the nanotube unzipping, instead of starting from a graphene sheet moves from a single or a multi walled nanotube [62]: as shown in Fig 1.23, different techniques were considered in the literature to perform this process [69, 62, 23, 40].

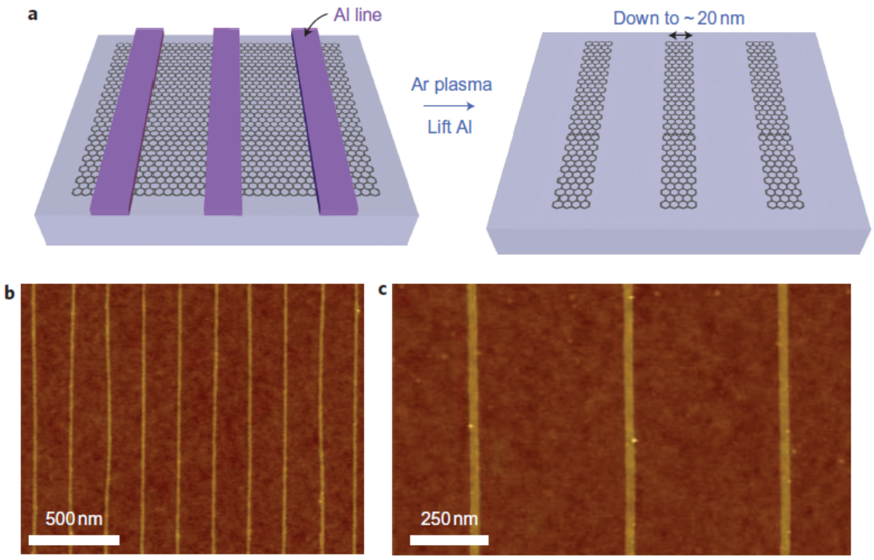

Figure 1.22.: Lithography method to produce GNRs: a) after covering the sheet with Al lines, the overall system is submitted to the plasma etching; only the parts covered by the Al lines will remain: these are the GNR nanoribbons; b) and c) AFM images of the GNR obtained. Image taken from [134]

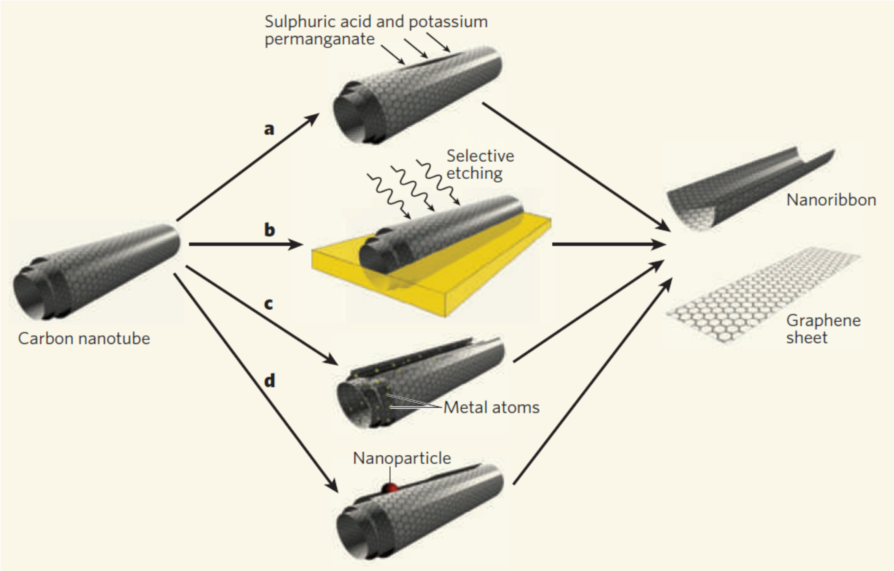

Figure 1.23.: Different methods to obtain a GNR from the unzipping of a multi walled nanotube: a)the nanotube is treated with sulphuric acid and potassium permanganate [69] b) the nanotube is previously embedded in a polymer film and then etched by argon plasma [62] c) the nanotube is unzipped through alakli-metal atoms [23] d) the nanotube is opened through a catalitic metal nanoparticle [40]. Image taken from [125]

These approaches have the advantage to produce long nanoribbons in a relatively simple way. However, there are two important drawbacks: first the nanoribbons produced in this way have a very large width ($>$ 10 nm [134]) and consequently they have a gap which is too low for microelectronic and optoelectronic applications; moreover their edges are rough and defected. This can be troublesome as one considers that the electronic properties of GNR are deeply influenced by the edge morphology. To overcome these problems, one can follow a bottom-up approach [75] : in this case one starts from a molecular seed, which is either deposited on a substrate, as done by Cai et al.[20], or immersed in a solution, as done by Narita et al. [89]; then this seed, through chemical reactions, is transformed into a GNR. One important point is that the GNR is fixed by the geometry of the precursor: for example, as reported by Cai et al. [20], the chevron-type nanoribbon and the 7-AGNR require two different molecular precursor (see Fig 1.24). A further example of a bottom up approach for the solution based growth of GNRs is provided in Fig 1.25.

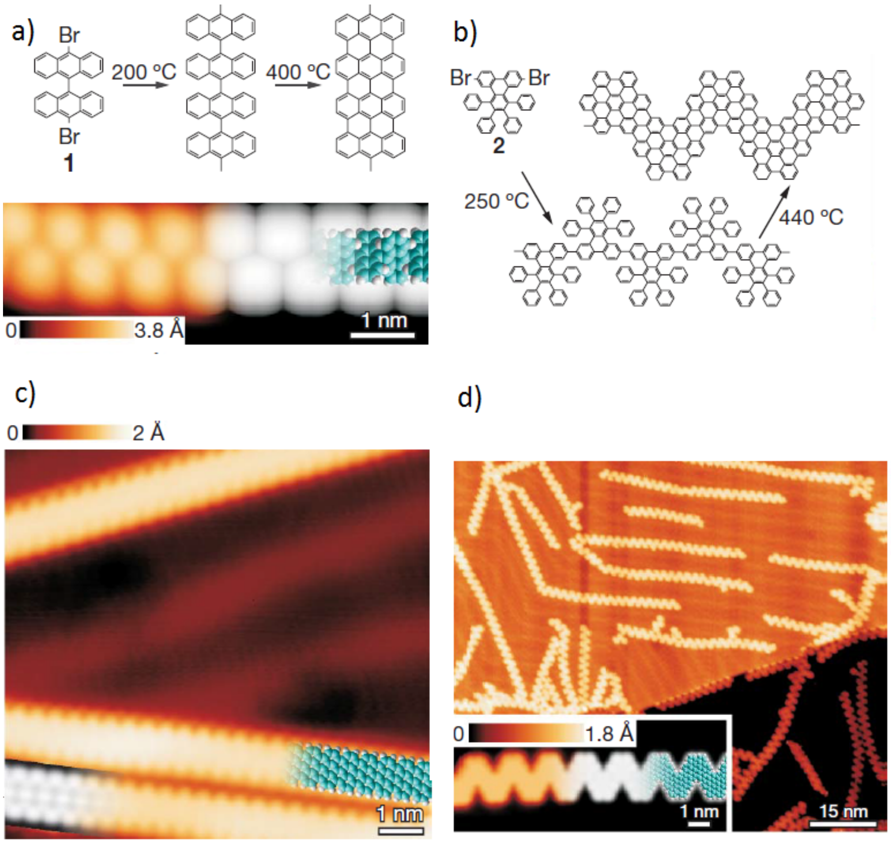

Figure 1.24.: Cai et al bottom-up approaches to obtain a GNR with atomically precise edges: in a) and b) panels the paths from the precursors to the 7-AGNR / chevron-type nanoribbon are shown, while in c) and d) panels the a STM images of the GNRs obtained are reported. Note the different morphology of the precursors. Image taken from [20]

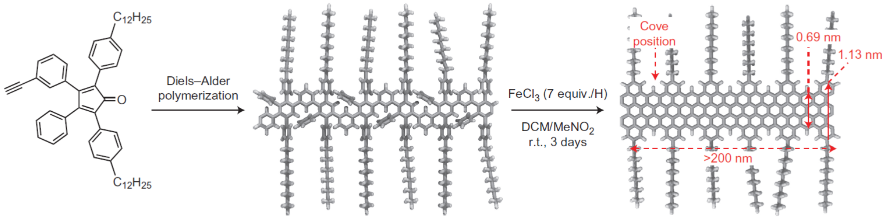

Figure 1.25.: Narita et al. bottom-up method for the synthesis of GNRs. Image taken from [89]

1.3 BEYOND GRAPHENE: H-BN AND TMDC

In addition to graphene, there are other layered materials constituted by atomically thin sheets: the most common examples are the hexagonal BN (h-BN) and the transition metal dichalcogenides (TMDCs). As we will show in this section, these materials present the same hexagonal lattice of graphene but the two sublattices are occupied by different atoms. This is sufficient to open up a gap and have a semiconductor behaviour.

HEXAGONAL-BN Within all possible phases of BN, reported in Fig 1.26, the hexagonal (h) and the cubic (c) ones are the most stable [98]. The h-BN is a layered structure composed by monolayers which have the same lattice of graphene, where the unitary cell is formed by an atom of boron and by an atom of nitrogen; furthermore, differently with respect to graphene, the h-BN sheets present an AA staking (see Fig 1.27). As for graphene, the fabrication of nanoribbon (BNNR) was demonstrated [98]. The h-BN, as for the other phases of BN, is an insulator with large gap: ab-initio investigations based on the GW approximation [14] predict an indirect gap of 5.4 eV for the bulk system and of 6.0 eV for the monolayer (see Fig 1.28). Concerning the vibrational properties, the phonon bands have some common features with those of graphite, as discussed in Refs [116, 87, 83] (see Fig. 1.29), and display the well-known Raman peak at 1373 cm^{-1} that is the h-BN analogue to G peak of graphene previously discussed [46, 55]. This material, due to its cathodoluminescence emission in deep ultraviolet, is appealing to produce laser devices for sterilization, ophthalmic surgery and nanosurgery [98]. Other applications can be obtained by combining it with other layered materials, as we will show in the last part of this chapter dedicated to the interfaces.

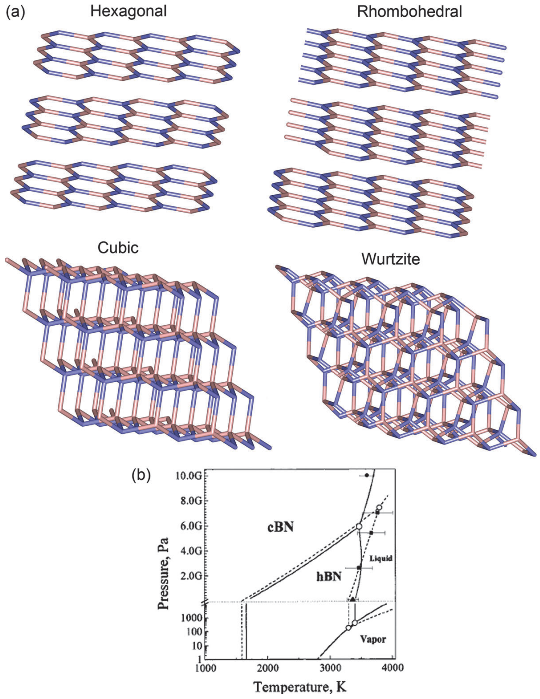

Figure 1.26.: Schematic of the different phases of BN accompained by the phase diagram. Image taken from [98]

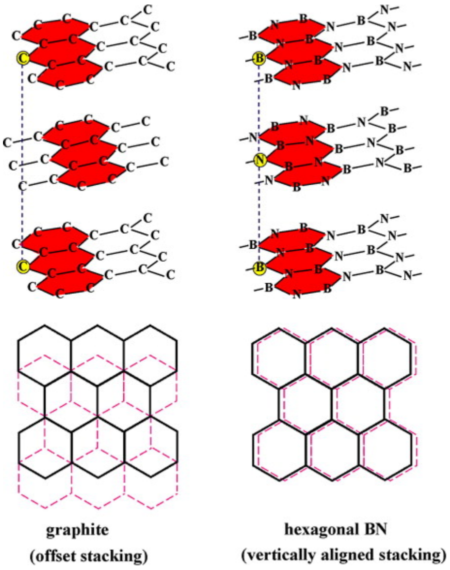

Figure 1.27.: Comparison between the piling of graphene layers (AB stacking) and of h-BN layers (AA stacking.). Image taken from [123]

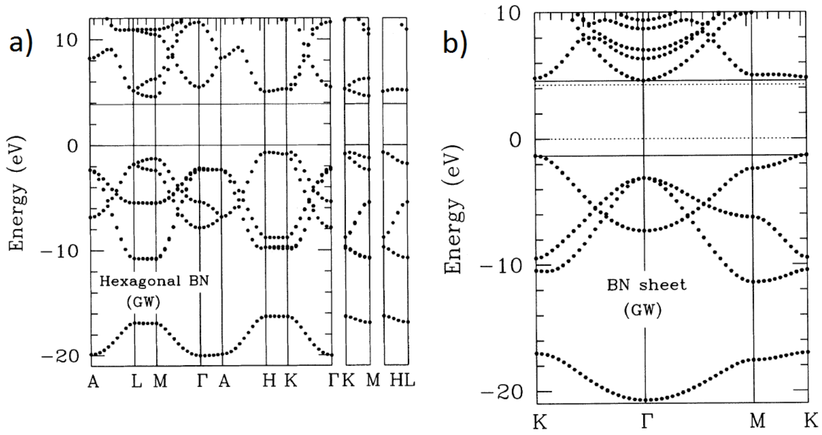

Figure 1.28.: Ab-initio investigation of the electronic band structure of bulk h-BN (left panel) and of a single monolayer (right panel). Images taken from [14]

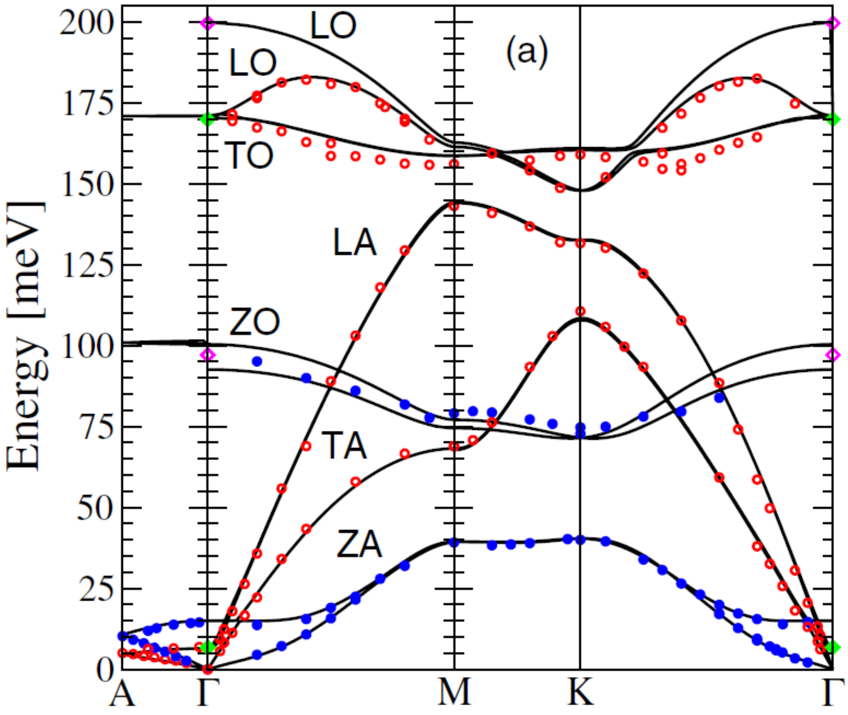

Figure 1.29.: Investigation of the phonon dispersion of h-BN as performed by Serrano et al. The red points stands for the X-ray data, the green and purple diamonds stands for the Raman and IR data [46, 91, 108] while the solid lines represent the dispersion calculated from ab-initio principles. Image taken from [116]

TRANSITION METAL DICHALCOGENIDES These materials are labelled by the formula MX_2 in which M stays for the element of the transition metal of the 4^{th}-10^{th} groups and X stays for the chalcogen atom (S,Se,Te) (see periodic table in panel a) Fig. 1.30). These atoms, as reported in Fig 1.30, can display two phases: the trigonal prismatic one or the octahedral one. As for graphite and for h-BN, TMDC monolayers can be easily obtained with the exfoliation method from their bulk [94]. In the realm of TMDCs, both metallic and semiconducting behaviour were found: NbX_2 and TaX_2 compounds are generally metallic, while MoX_2 and WX_2 are generally semiconducting [133]. Considering the latter, it is interesting to note that, while the bulk system has an indirect gap, for the monolayer systems a direct gap is found (see Fig 1.31). As pointed out in different papers [70, 133, 29], this can be recognized as an effect of quantum confinement.

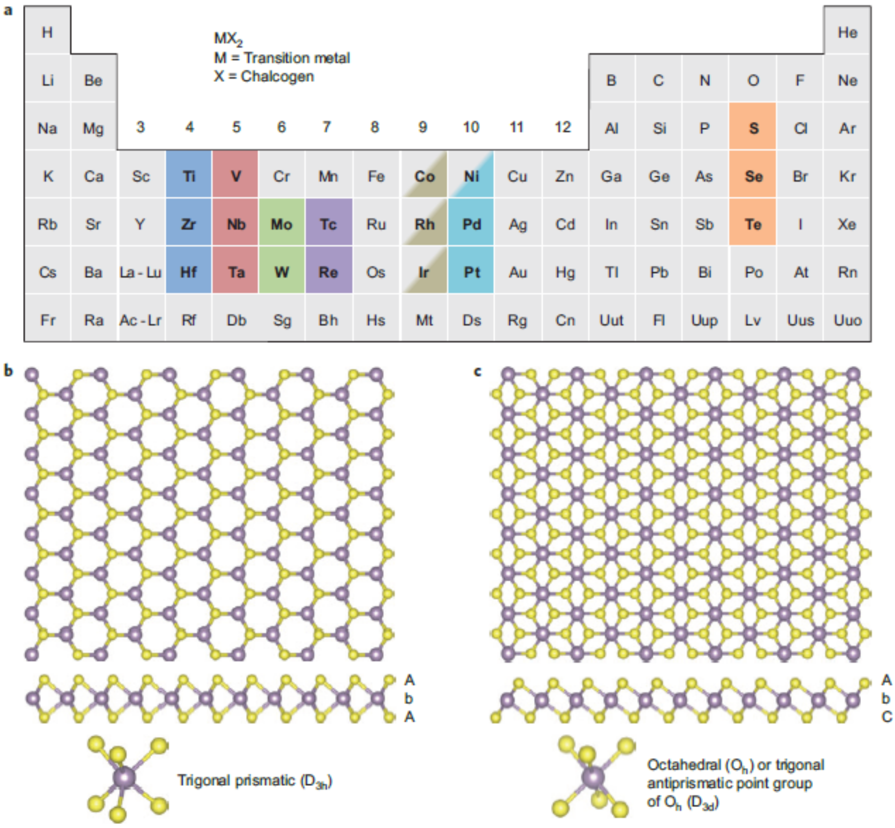

Figure 1.30.: a) The elements of the periodic table which can compose the TMDC b) The two possible lattices of a TMDC. Image taken from [29]

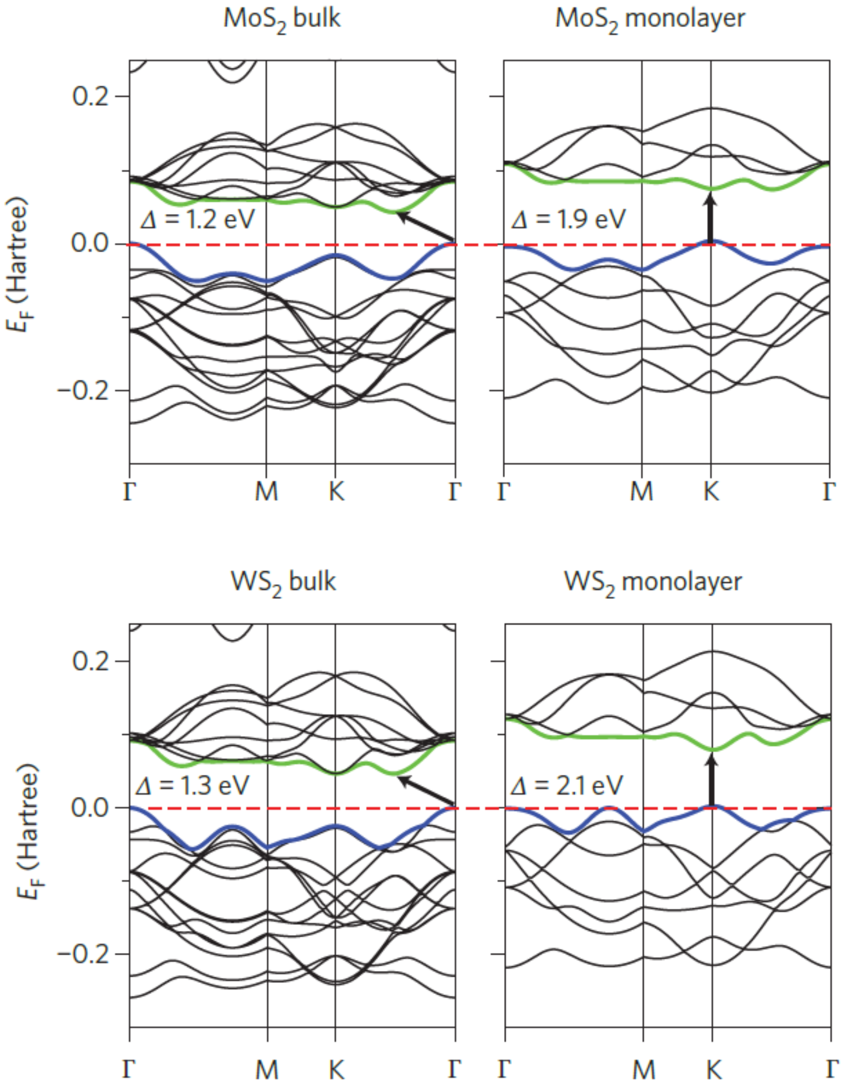

Figure 1.31.: Monolayer vs bulk electronic structure for two TMDC. Images taken from [70]

1.4 HETEROSTRUCTURES

The previously presented 2D materials can be coupled in order to obtain a heterostructure, whose overall properties are different with respect to its single components. This coupling can be performed in two ways : the first option is to combine stripes of different 2D material in order to form a *2D superlattice*; the second option is to couple the 2D layers via the Van der Waals interaction in order to form a stack, called *Van der Waals heterostructure* [47];

2D SUPERLATTICES The idea of confining electrons in low dimension by coupling different materials was widely applied in the past for semiconductors. The most important case of bulk superlattice is the GaAs/AlAs whose properties and characterization were deeply investigated in the literature [85, 24]. Recently, this idea was considered also for 2D systems: for example a theoretical study performed by Pruneda et al. [106] investigated the electronic properties a 2D superlattice composed by graphene and h-BN. As shown in Fig.1.33, the electronic properties of this superlattice are strongly dependent on the width of each subsystem. This type of superlattice has not remained a theoretical speculation: in 2013 Liu et al. [77] were able to grow such system by first etching a h-BN monolayer and then filling the etched region with graphene through the CH_4 as carbon source. Their results are reported in Fig 1.32. 2D TMDC superlattices are also promising: a recent theoretical study performed by Zaho et al. [143] on $MoS_2/MoSe_2$ superlattices pointed out the high tunability of electronic bands structure when the composition of the superlattice is changed (Fig 1.34).

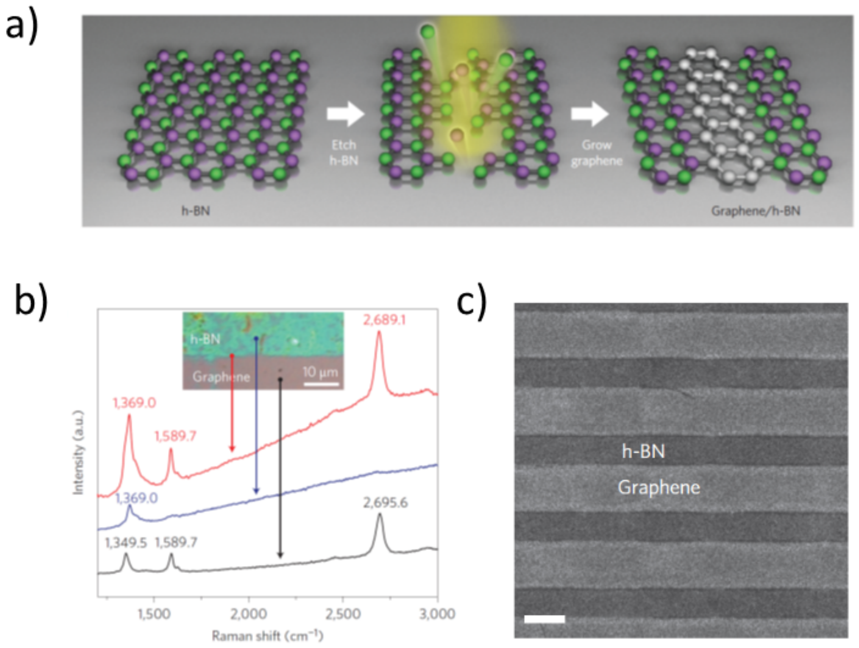

Figure 1.32.: Experimental realization of a Graphene/h-BN 2D superlattice [77]: a) a schematic picture of the method used to produce the superlattice b) the Raman spectra used to fingerprint its components c) a SEM image of the whole system. Images taken from [77]

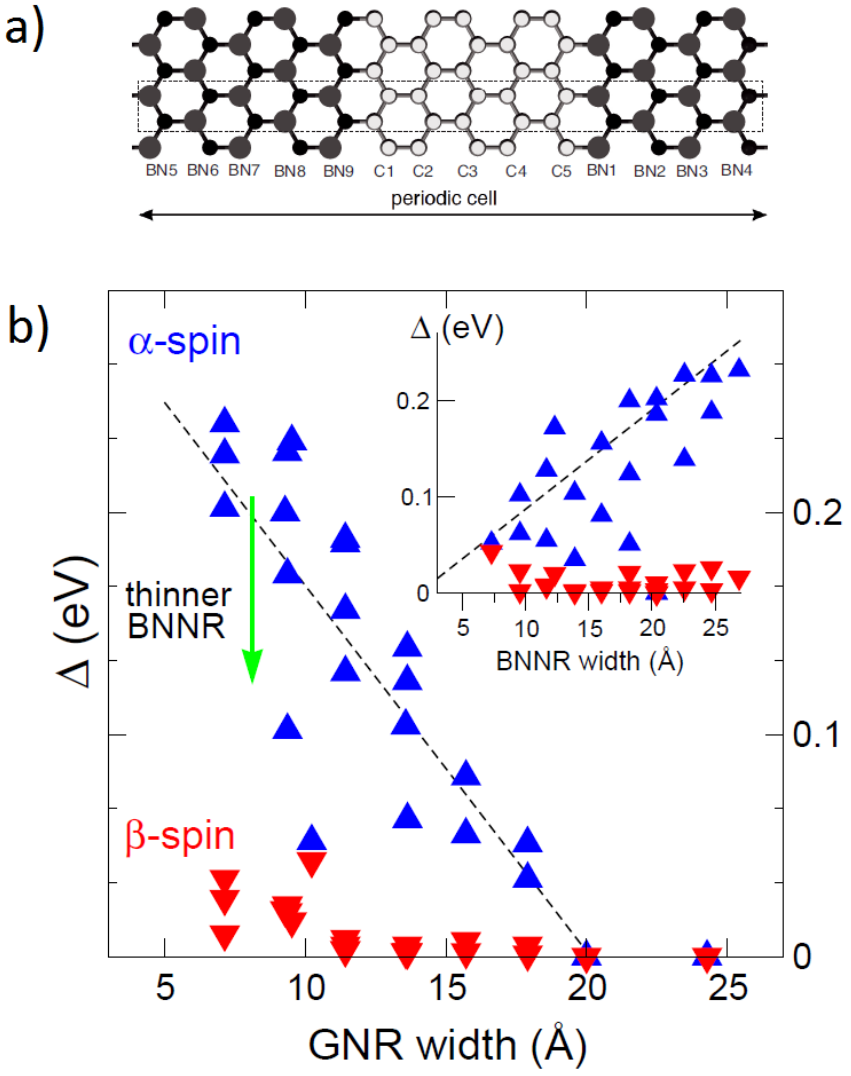

Figure 1.33.: Theoretical investigation of the electronic properties of the h-BN/Gr 2D superlattices: a) an example of a superlattice formed by 5 C zigzag chains and 9 BN zigzag chains b) electronic direct gap calculated with DFT as function of the width of the GNR and of the BN nanoribbon (BNNR). Images taken from [106]

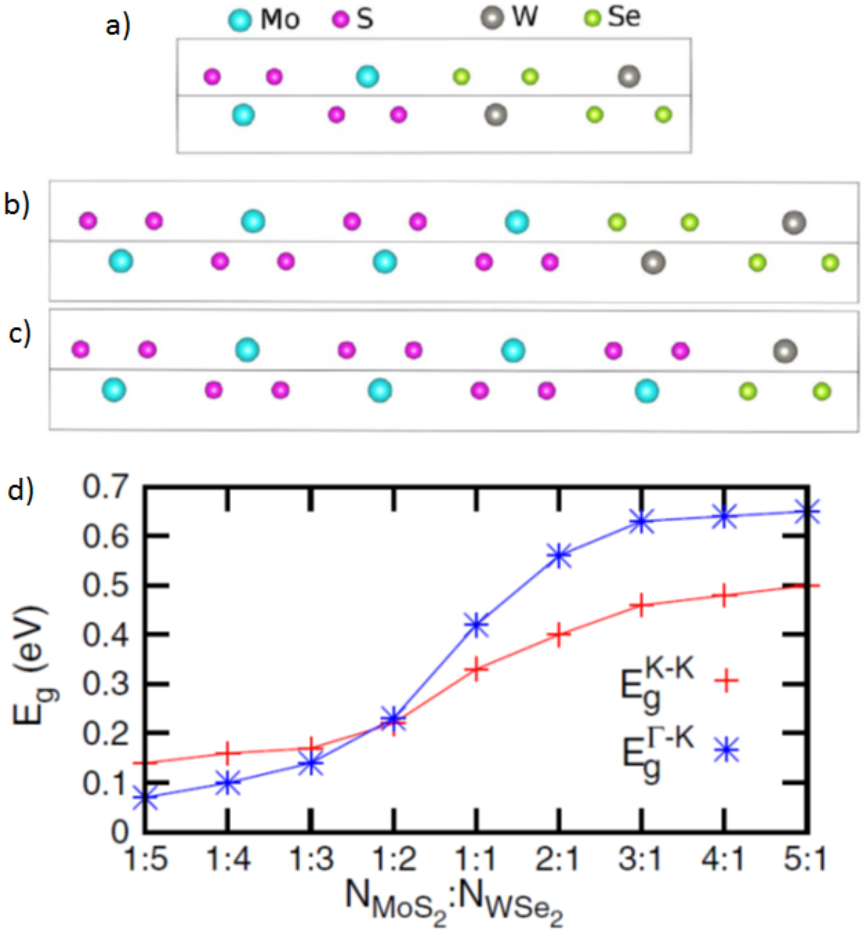

Figure 1.34.: Theoretical investigation of TDMC 2D superlattices [143]: a-d) side view of different MoSWSe superlattice d) Direct and indirect electronic gaps as function of the composition of the superlattice. Images taken from [143]

VAN DER WAALS HETEROSTRUCTURES Another way to manipulate the electronic properties of 2D materials is the staking into vertical Van der Waals heterostructures. Since this coupling can modify the properties of the materials involved, one, can use this approach for instance to manipulate the electronic structure of graphene. This is the case of the graphene/h-BN interface, where, as pointed out by Giovanetti et al. in [54], the presence of the h-BN lattice makes the graphene semiconducting because its two sublattices are no longer equivalent. In their paper, Giovanetti et al. calculated with ab-initio methods the relative stability and the electronic structure of different configuration of the h-BN/Graphene interface: as it can be seen in Fig 1.35, the width of the gap is highly dependent on the registry. It is worth noting that the most stable configuration, according to these calculations, is the one in which a carbon atom is superimposed onto a boron atom which in turn is superimposed onto a nitrogen atom. Unfortunately, it is quite difficult by now to experimentally grow perfect lattices such as the simulated ones: usually the orientation of the graphene lattice on the h-BN substrate is random and this does not change the metallicity of graphene, since the symmetry of the lattices is not broken [107]. However, the transport properties of this interface are very interesting: as pointed out by Dean at al., in this configuration graphene shows much larger mobilities with respect to the graphene/SiO_2 interface.

More than two lattices can be involved in a heterostructure: a recent work performed by Withers et al. [136] pointed out the realization of a layered system in which graphene was combined with h-BN and TMDC in order to form single and multi quantum-wells. The importance of this type of system, that can be used as diodes, relies both on their quantum efficiency (8.4 %) and on their high flexibility.

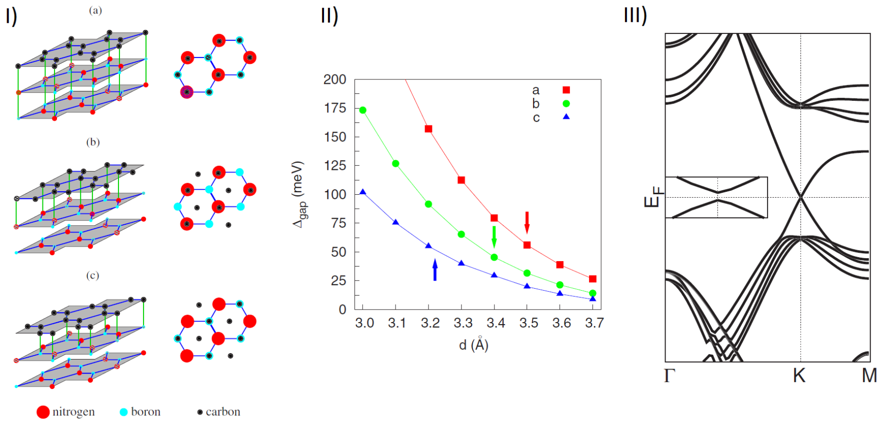

Figure 1.35.: The main results of the theorical work performed by Giovannetti et al. on the graphene/h-BN interface: I) Possible configurations of the interface; II) behaviour of the electronic gap for the configurations reported in I) when the distance between the h-BN and graphene is changed; III) electronic band strucutre for the relaxed structure c). Images taken from [54]

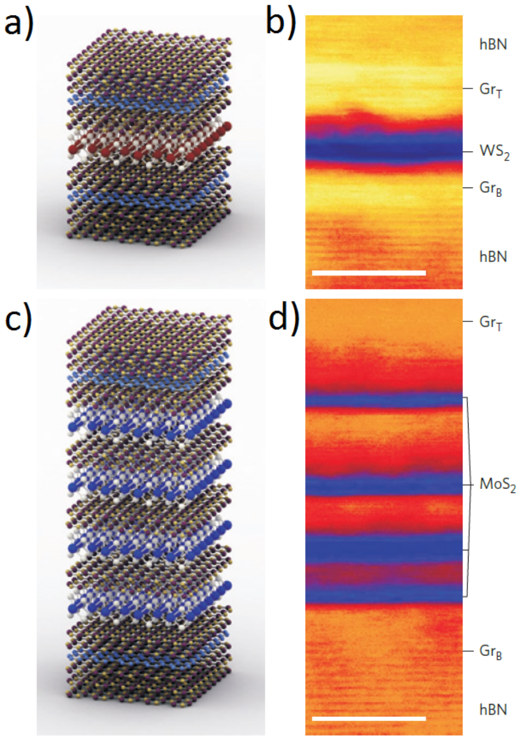

Figure 1.36.: The heterostructure proposed by Withers et al.: a) a schematic view of the piling sequence of the different materials (h-BN, MoS2 and graphene) used for the realization of a single QW; b) accompanied by a TEM image of the corresponding experimental system; c) and d) same as a) and b) but for a multiple QW. Images taken from [136]

2 VIBRATIONAL AND OPTICAL SPECTROSCOPIES

In the research of the different growing and engineering processes that involve the low dimensional materials, a fundamental role is played by the characterization techniques. Among the different methods available, a crucial role is played by the Raman and the absorption spectroscopies, due to the fact that they provide very useful informations about the sample in a non destructive way. Concerning the latter, depending on the frequency of the incident radiation, two properties can be probed: in the IR range the absorbed light excites the vibrational levels, while in the UV-VIS range the electronic levels are involved. As already shown in the previous chapter, the Raman spectroscopy provides useful information about graphene-based low dimensional systems, such as the presence of defects in a graphene sheet, the number of layer in a multi-layered graphene system, the diameter of a carbon nanotube, the width and the edge morphology of a GNR. On the other side, the UV-VIS spectroscopy and infrared (IR) spectroscopy are two efficient techniques for the investigation, respectively, of the electronic properties of the sample an on its functional groups. All these techniques provide a formidable characterization tool for the nanostructures that are growth in solution through the chemical addition. In this chapter we are going to briefly review the basic physical principles of these light-mediated spectroscopies.

2.1 RAMAN SCATTERING

In the Raman effect, the light matter interaction is declined in an inelastic scattering process where the incident light indirectly interacts with the lattice vibrations of the sample. We first introduce the description of the Raman process through a classical approach, as proposed by Cardona in [25], and then we move to a quantum approach as proposed by Bruesch in [18].

CLASSICAL MODEL We consider an infinite and isotropic medium interacting with a light beam with electrical field component [25]:

$$\mathbf{F}\left(\mathbf{r},t\right)=\mathbf{F}_i(\mathbf{k}_i,\omega_i)\cos\left(\mathbf{k}_i\cdot\mathbf{r}-\omega_i t\right) \tag{2.1}$$

where ω_i and k_i are respectively the frequency and the wavevector of the incident beam. As consequence, the polarization of the medium will be [25]

$$\mathbf{P}\left(\mathbf{r},t\right)=\mathbf{P}_i(\mathbf{k}_i,\omega_i)\cos\left(\mathbf{k}_i\cdot\mathbf{r}-\omega_i t\right) \tag{2.2}$$

the incident field $\mathbf{F}$ and the polarization $\mathbf{P}$ are related by the following expression [25]

$$\mathbf{P}\left(\mathbf{k}_i,t\right)=\chi(\mathbf{k}_i,\omega_i)\mathbf{F}_i\left(\mathbf{k}_i,\omega_i\right) \tag{2.3}$$

in which $\chi(\mathbf{k},\omega_i)$ is the electric susceptibility, a scalar quantity since the material is assumed to be isotropic. The electric susceptibility is modified by the lattice vibrations $\mathbf{Q}\left(\mathbf{r},t\right)$. Within the adiabatic approximation it can be written as $\chi(\mathbf{k},\omega_i,\mathbf{Q})$, which can be expanded on the atomic displacements: [25]

$$\chi(\mathbf{k}_i,\omega_i,\mathbf{Q})=\chi_0\left(\mathbf{k}_i,\omega_i\right)+\left(\partial\chi/\partial\mathbf{Q}\right)_0\mathbf{Q}\left(\mathbf{r},t\right)+\dots \tag{2.4}$$

where

$$\mathbf{Q}\left(\mathbf{r},t\right)=\mathbf{Q}\left(\mathbf{q},\omega_0\right)\cos\left(\mathbf{q}\cdot\mathbf{r}-\omega_0 t\right) \tag{2.5}$$

As a consequence, the overall polarization of the system will consist in two part: one derived by the electric component of the incident wave $\mathbf{P}_0$ and another one $\mathbf{P}_{ind}$ which is induced by the lattice vibrations [25]

$$\mathbf{P}\left(\mathbf{r},t,\mathbf{Q}\right)=\mathbf{P}_0\left(\mathbf{r},t\right)+\mathbf{P}_{ind}\left(\mathbf{r},t,\mathbf{Q}\right) \tag{2.6}$$

$$\mathbf{P}_0\left(\mathbf{r},t\right)=\chi_0\left(\mathbf{k}_i,\omega_i\right)\mathbf{F}_i\left(\mathbf{k}_i,\omega_i\right)\cos\left(\mathbf{k}_i\cdot\mathbf{r}-\omega_i t\right) \tag{2.7}$$

$$\mathbf{P}_{ind}\left(\mathbf{r},t,\mathbf{Q}\right)=\left(\partial\chi/\partial\mathbf{Q}\right)_0\mathbf{Q}\left(\mathbf{r},t\right)\mathbf{F}_i\left(\mathbf{k},\omega_i\right)\cos\left(\mathbf{k}_i\cdot\mathbf{r}-\omega_i t\right) \tag{2.8}$$

By inserting the expressions 2.1 and 2.5 in this last equation one obtains [25]

$$\begin{aligned}\mathbf{P}_{ind}\left(\mathbf{r},t,\mathbf{Q}\right)=&\frac{1}{2}\left(\partial\chi/\partial\mathbf{Q}\right)_0\mathbf{Q}\left(\mathbf{q},\omega_0\right)\mathbf{F}_i\cdot\\&\cdot\{\cos\left[\left(\mathbf{k}_i-\mathbf{q}\right)\cdot\mathbf{r}-\left(\omega_i-\omega_0\right)t\right]\\&+\cos\left[\left(\mathbf{k}_i+\mathbf{q}\right)\cdot\mathbf{r}-\left(\omega_i+\omega_0\right)t\right]\}\end{aligned} \tag{2.9}$$

This identity for the induced polarization states that two waves, with frequencies and wavevectors different with respect to the incident one, emerge due to the interaction of the incident beam with the lattice vibrations, represented by a phonon of wavevector q and energy ω_0. The first one has a redshifted frequency $(\omega_i - \omega_0)$ and it is called Stokes wave: in this case part of the energy of the incident light was converted in vibrational energy; the second one has a blueshifted frequency $(\omega_i + \omega_0)$ and it is called anti-Stokes wave: in this case the vibrational energy of the lattice was converted in to a part of the outgoing light.

QUANTUM MODEL The Raman scattering can be also described within a quantum formalism as reviewed, for example, by Bruesch in [18] : in this approach, the states of the sample are described by the vibronic levels while the incident light is described by photons. In such a formalism, the Stokes process is rewritten in the following way: firstly the incident photon is destroyed and the energy of the system is increased, then the system relaxes into a state which has a higher vibrational energy with respect to the starting state; during this last process a photon whose energy is lower with respect to the incident one is produced (see Fig 2.1). On the other side, in the anti-Stokes process, an incident photon is absorbed by the sample that lies into an excited state, then this system relaxes into a state with a lower vibrational energy: this last process produces a photon whose energy is blueshifted with respect to the incoming one. The predicted intensity of the Raman scattering is given by the Kramers-Heisemberg-Dirac expression [16] which describes the interaction of a photon with an atom [18]:

$$I_{km} = \frac{1}{c^3}\left(\omega_L + \omega_{km}\right)^4 \left|\left(c_{\rho\sigma}\right)_{km}\right|^2 I_0 \tag{2.10}$$

$$\left(c_{\rho\sigma}\right)_{km} = \frac{1}{\hbar}\sum_r \left(\frac{\left(M_\sigma\right)_{kr}\left(M_\rho\right)_{rm}}{\omega_{rk} - \omega_L} + \frac{\left(M_\rho\right)_{kr}\left(M_\sigma\right)_{rm}}{\omega_{rm} + \omega_L} \right) \tag{2.11}$$

where I_0 is the intensity of the incident light, ω_0 its frequency, M the transition dipole moment, ρ and σ the polarizations of the incident and outgoing beams and k,r,m are respectively the initial, intermediate and final levels (see Fig 2.1) . The quantity $\left(c_{\rho\sigma}\right)_{km}$ is called Raman tensor. Note that, by now, the direct evaluation of the intensity represents a very difficult task, since the perfect knowledge of the excited states is required. As shown by Placzek [78, 18], the evaluation of the tensor $(c_{\rho\sigma})_{km}$ is strongly simplified if the frequency of the exciting laser is lower with respect to the electronic transitions (with the additional requirements of non-degenerate ground state and validity of adiabatic approximation), so that the ions can be considered fixed in to a nuclear coordinate Q during the electronic transition. Consequently, the dynamic polarizability c, which is in principle dependent on the electronic and vibrational coordinates, can be replaced with the adiabatic dynamic polarizability which is dependent only by the nuclear coordinates Q [18]:

$$(c_{\rho,\sigma 0n,0n'}) = \int \psi^*_{0n'}(Q)\alpha_{\rho,\psi}(Q)\psi_{0n'}(Q)dQ = (\alpha_{\rho,\sigma}(Q))_{0n,0n'} \tag{2.12}$$

where $\psi_{0n}(Q)$ indicates a vibrational wavefunction in an electronic ground state 0 and in a vibrational state n.This allows to expand the matrix element $(c_{\rho\sigma})_{km}$ in terms of normal coordinates Q [18]:

$$(\alpha_{\rho\sigma}) = (\alpha_{\rho\sigma})^0_{\rho\sigma} + \sum_s \alpha_{\rho\sigma,s}Q_s + \frac{1}{2}\sum_{s,s'} \alpha_{\rho\sigma,ss'}Q_sQ_{s'} + \dots \tag{2.13}$$

where

$$\alpha_{\rho,\sigma,s} = \left(\frac{\partial\alpha_{\rho\sigma}}{\partial Q_s}\right)_0 \tag{2.14}$$

Within these approximations, the Stokes and anti-Stokes intensities will be described by the following expressions [18]

$$I_{Stokes} \propto (\omega_L - \omega_s)^4 \frac{\hbar}{2\omega_s}\alpha^2_{\rho\sigma,s}(1+\overline{n}) \tag{2.15}$$

$$I_{anti-Stokes} \propto (\omega_L + \omega_s)^4 \frac{\hbar}{2\omega_s}\alpha^2_{\rho\sigma,s}(\overline{n}) \tag{2.16}$$

$$\overline{n} = [\exp(\hbar\omega_s/K_BT) - 1]^{-1} \tag{2.17}$$

If the energy of the exciting laser is close to the gap or if the system is a metal, the so-called resonant Raman scattering process occurs and the vibrational and electronic degree of freedom cannot be decoupled. The description of the resonant Raman is beyond the aim of this thesis work, a treatment on it, in which the Herzeberg-Teller vibronic coupling is considered, will be found in [6, 78]. Finally, it is worth noting that the previously reviewed classical and quantum Raman scattering models are limited to one-phonon process: as a consequence, only the lattice vibration at Γ will be probed; however, one can go beyond the first order expansion in the equations 2.4 and 2.13: in this case, since two phonons are involved, the entire BZ can be probed. The scattering process where more then one phonon is involved is called overtone.

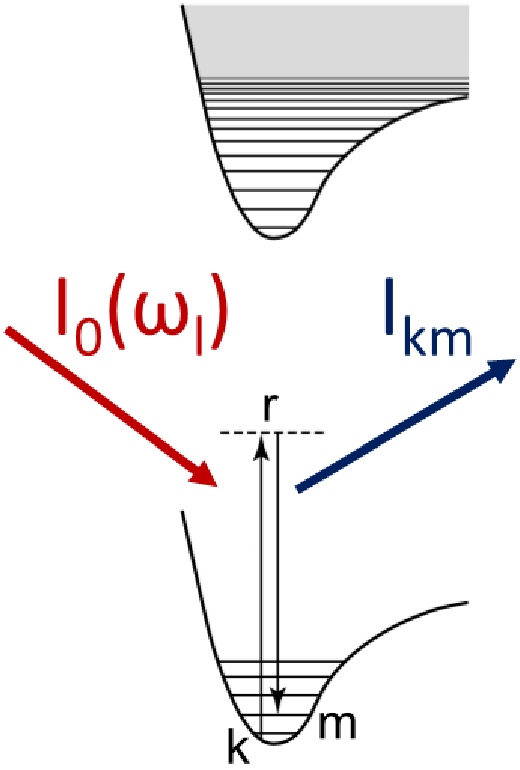

Figure 2.1.: A schematic view of the transitions involved in the off-resonance Stokes process according to a quantum description. The image is taken from [78]

2.2 OPTICAL ABSORPTION

Besides Raman spectroscopy, there is another spectroscopic technique that uses the light to probe the characteristics of the sample: this is the optical absorption spectroscopy. Differently from the Raman spectroscopy the incident light in this case is absorbed by the medium.

LIGHT ABSORPTION Following the Wooten approach [137] we start by considering an isotropic medium where the following relations holds [137]

$$\mathbf{D} = \epsilon\mathbf{E} \tag{2.18}$$

$$\mathbf{B} = \mu\mathbf{H} \tag{2.19}$$

$$\mathbf{J} = \sigma\mathbf{E} \tag{2.20}$$

here **E** and **B** are the incident electric and magnetic fields, μ the magnetic permeability, ϵ dielectric tensor, **J** the current density and σ the conductivity. When an incident radiation impact this medium a part of it may be absorbed. In this case, the Maxwell equations have the following form [137]

$$\begin{aligned}\nabla\cdot\mathbf{E} &= 0\\ \nabla\times\mathbf{E} &= -\frac{\mu}{c}\frac{\partial\mathbf{H}}{\partial t}\\ \nabla\cdot\mathbf{H} &= 0\\ \nabla\times\mathbf{H} &= \frac{\epsilon}{c}\frac{\partial\mathbf{E}}{\partial t}+\frac{4\pi\sigma}{c}\mathbf{E}\end{aligned} \tag{2.21}$$

By handling the Maxwell equations, the following form of the wave-equation can be obtained [137]

$$\nabla^2\mathbf{E} = \frac{\epsilon\mu}{c^2}\frac{\partial^2\mathbf{E}}{\partial t^2}+\frac{4\pi\sigma\mu}{c^2}\frac{\partial\mathbf{E}}{\partial t} \tag{2.22}$$

If one considers an incident monocromatic wave [137]

$$\mathbf{E} = \mathbf{E}_0\exp\left(i\left(\hat{\mathbf{q}}\mathbf{r}-\omega t\right)\right) \tag{2.23}$$

and put this last equation into Eq. 2.22, one obtains [137]

$$\hat{q}^2 = \mu\frac{\omega^2}{c^2}\left(\epsilon+i\frac{4\pi\sigma}{\omega}\right) \tag{2.24}$$

Looking to this last equation, it seems useful to define the complex refractive index $\hat{n}$ [137]

$$\hat{q} = \frac{\omega}{c}\hat{n} = \frac{\omega}{c}(n + ik) \tag{2.25}$$

Here n is the refractive index and k the extinction coefficient. Using the complex refractive index, Eq 2.23 can be recast as [137]

$$\mathbf{E} = \mathbf{E}_0 exp\left(-\frac{\omega}{c}\mathbf{k}\cdot\mathbf{r}\right) exp\left(i\left(\frac{\omega}{c}\mathbf{n}\cdot\mathbf{r} - \omega t\right)\right) \tag{2.26}$$

The first term on the left side governs the absorption of the incident beam, while the second term describes a travelling wave with velocity c/n. It is useful to define a new quantity, called the absorption coefficient, that is defined as [137]:

$$\alpha = -\frac{1}{I}\frac{dI}{dr} \tag{2.27}$$

where I is the intensity of the electric field [137]

$$I = \frac{1}{2}|E| \tag{2.28}$$

If we put Eq. 2.26 into Eq. 2.27 the following identity is obtained [137]

$$\alpha = 2\omega k/c = 4\pi k/\lambda \tag{2.29}$$

where λ is the wavelength of the incident light in vacuum. Through Eq. 2.24 and 2.25 one can recast ϵ and σ in the following form [137]

$$\epsilon = \left(n^2 - k^2\right)/\mu \tag{2.30}$$

$$4\pi\sigma/\omega = 2nk/\mu \tag{2.31}$$

Considering ϵ as a complex function [137]

$$\epsilon = \epsilon^{Re} + i\epsilon^{Im} \tag{2.32}$$

one can write the real and imaginary part as [137]

$$\epsilon^{Re} = \left(n^2 - k^2\right)/\mu \tag{2.33}$$

$$\epsilon^{Im} = 2nk/\mu = 4\pi\sigma/\omega \tag{2.34}$$

In order to link these theoretical expressions to the absorption quantities obtained in an experiment, it useful to evalute the time average power absorbtion per unit volume by the medium. For this propose we recall that [18]

$$\bar{W} = \mathbf{J}\bar{\mathbf{E}} \tag{2.35}$$

$$\mathbf{J} = \sigma \mathbf{E} \tag{2.36}$$

$$\sigma = \frac{\omega}{4\pi}\epsilon^{Im} \tag{2.37}$$

Consequently the power absorbed will be [18]

$$\begin{aligned}\bar{W}(\omega) &= \frac{1}{4\pi}\omega\epsilon^{Im}E_0^2\overline{cos^2\omega t} \\ &= \frac{1}{8\pi}\omega\epsilon^{Im}E_0^2(\omega)\end{aligned} \tag{2.38}$$

The key quantity is the dielectric function: depending on its frequency the incident radiation can excite the electronic levels (UV-VIS) or vibrational levels (IR absorption). As a consequence, for these two absorption ranges, the dielectric function will have two different forms that we are now going to review.

2.3 DIELECTRIC FUNCTION: UV-VIS RANGE

Following the classical approach described in [137], we start by considering the atoms as composed by an electron bounded through an ideal spring to a fixed nucleus [137]:

$$m\frac{d^2\mathbf{r}}{dt^2} + m\Gamma\frac{d\mathbf{r}}{dt} + m\omega_0^2\mathbf{r} = -e\mathbf{E}_{loc} \tag{2.39}$$

here m labels the electronic mass, e the electronic charge, Γ the damping factor that accounts the energy loss due to the internal scatterings and ω_0 the oscillating frequency of the electrons in absence of external local field E_{loc}. This differential equation has the following solution [137]:

$$\mathbf{r} = \frac{-e\mathbf{E}_{loc}/m}{\omega_0^2 - \omega^2 - i\Gamma\omega} \tag{2.40}$$

so the induced dipole moment will be [137]:

$$\mathbf{p} = \frac{e^2 \mathbf{E}_{loc}}{m} \frac{1}{(\omega_0^2 - \omega^2) - i\Gamma\omega} \tag{2.41}$$

From this last expression we can introduce the atomic polarizability α [137]:

$$\mathbf{p} = \alpha \mathbf{E}_{loc} \tag{2.42}$$

so that [137]:

$$\alpha(\omega) = \frac{e^2}{m} \frac{1}{(\omega_0^2 - \omega^2) - i\Gamma\omega} \tag{2.43}$$

The macroscopic polarization of a solid composed by N atoms per unit volume is [137]:

$$\mathbf{P} = N \langle \mathbf{p} \rangle = N\alpha \langle \mathbf{E}_{loc} \rangle = \chi_e \mathbf{E} \tag{2.44}$$

Taking advantage of the isotropic approximation $\langle \mathbf{E}_{loc} \rangle = \mathbf{E}$, the macroscopic polarization can be rewritten as [137]:

$$\mathbf{P} = N\alpha \mathbf{E} = \chi_e \mathbf{E} \tag{2.45}$$

where χ_e is the electronic electric susceptibility. Finally the dielectric function ϵ can be obtained using the following identity [137]

$$\mathbf{D} = \epsilon \mathbf{E} = \mathbf{E} + 4\pi \mathbf{P} \tag{2.46}$$

so that [137]

$$\epsilon = 1 + \frac{4\pi N e^2}{m} \frac{1}{(\omega_0^2 - \omega^2) - i\Gamma\omega} \tag{2.47}$$

The previous equation can be extended to a many electron system [137]

$$\epsilon = 1 + \frac{4\pi N e^2}{m} \sum_j \frac{N_j}{\left(\omega_j^2 - \omega^2\right) - i\Gamma_j \omega} \tag{2.48}$$

where N_j is the density of electron with resonance frequency ω_j. A similar expression can be obtained using a quantum mechanical model (the details can be found in [137]):

$$\epsilon = 1 + \frac{4\pi N e^2}{m} \sum_m \frac{f_{m0}}{(\omega_{m0}^2 - \omega^2) - i\Gamma\omega} \tag{2.49}$$

where in this case ω is the transition frequency between two electronic states that differ by $\hbar\omega_{m0}$ and f_{m0} is the corresponding oscillator strength; this quantity, that measures the probability of an electronic transition, is defined as [137]

$$f_{m0} = \frac{2m\hbar\omega_{m0}}{\hbar^2}|x_{m0}|^2 \tag{2.50}$$

where x_{m0} labels the square modulus of the trasition dipole matrix element.

2.4 DIELECTRIC FUNCTION: IR RANGE

In the case of IR absorption, the lattice vibrations have to be taken into account. This can be done by considering the following model, as done by Cardona [25], in which an incident electromagnetic wave [25]

$$\mathbf{E}(\mathbf{r}, t) = \mathbf{E}_0 \exp i \left(\mathbf{k} \cdot \mathbf{r} - \omega t\right) \tag{2.51}$$

crosses a collection of n identical and charged simple hamonic oscillators (SHO), isotropically distributed in space. Their equation of motion will be [25] :

$$M\left(\frac{d^2\mathbf{u}}{dt^2}\right) = -M\omega_T^2\mathbf{u} + Q\mathbf{E} \tag{2.52}$$

where M, Q and ω_T are respectively the mass, the charge and the frequency of the SHO. The general solution has the following form [25] :

$$\mathbf{u} = \mathbf{u}_0 \exp\left[i\left(\mathbf{k} \cdot \mathbf{r} - \omega t\right)\right] \tag{2.53}$$

Replacing this last expression in Eq. 2.52, one obtains [25]:

$$\mathbf{u}_0 = \frac{Q\,\mathbf{E}}{M\left(\omega_T^2 - \omega^2\right)} \tag{2.54}$$

On the other hand, the polarization will be equal to [25]:

$$\mathbf{P} = nQ\mathbf{u} \tag{2.55}$$

By considering Eq. 2.46, one can obtain the following expression for the dielectric function of such system [25]:

$$\epsilon = 1 + \frac{4\pi n Q^2}{M\left(\omega_T^2 - \omega^2\right)} \tag{2.56}$$

By now, we have considered only the contribution due to phonons; however, also the valence electrons have to be taken in to account: if an incident radiation with frequency ω such that $E_g \gg \hbar\omega$ is considered (E_g labels the electronic gap amplitude), the dielectric function of electrons (see Eq. 2.49) reduces to $\epsilon_{el}(0)$. Setting [25]:

$$\epsilon_\infty = \epsilon_{el}(0) + 1 \tag{2.57}$$

the overall dielectric function will be [25]

$$\epsilon = \epsilon_\infty + \frac{4\pi n Q^2}{M\left(\omega_T^2 - \omega^2\right)} \tag{2.58}$$

According to the Gauss theorem if no charge excess is present in the medium: [25]

$$\nabla \cdot \mathbf{D} = 0 \tag{2.59}$$

$$\epsilon\left(\mathbf{k} \cdot \mathbf{E}\right) = 0 \tag{2.60}$$

There are two ways by which Eq. 2.60 can be satisfied: the first one is given by $\epsilon = 0$ and concern the longitudinal fields. The second one correspond to $(\mathbf{k} \cdot \mathbf{E}) = 0$, which means that a transverse field is considered; here, at the ω_T frequency, we have an IR absorption since the dielectric function diverges. This model can be generalized for a crystal with n atoms in the unitary cell (the details of this derivation can be found in ref. [18]) [128]:

$$\epsilon\left(\omega\right)^{Re} = \epsilon^{\infty} + \frac{4\pi}{3\Omega}\sum_n \frac{|\mathbf{f}^n|^2}{\omega^2 - \omega_n^2} \tag{2.61}$$

$$\epsilon\left(\omega\right)^{Im} = \frac{4\pi^2}{3\Omega}\sum_n \frac{|\mathbf{f}^n|^2}{\omega_n^2}\delta\left(\omega - \omega_n\right) \tag{2.62}$$

where Ω is the volume of the unit cell, χ the dielectric susceptibility tensor, ω_n is the frequency of the n vibrational mode and $\mathbf{f}^n$ is the oscillator strength of the n mode whose components along the k directions are given by the following expression [128]:

$$f_k^n = \sum_{I,i} Z^*_{I,ki} u^n_{I,i} \tag{2.63}$$

here I labels the nucleus of the system, i the direction of the displacement u and Z^* the Born effective charges. These are defined as [128]:

$$Z^*_{I,ij} = \Omega \frac{\partial P_i^{el}}{\partial r_{Ij}} \tag{2.64}$$

where P_i^{el} is the electronic polarization along the direction i produced by a unitary displacement of the atom I in the direction j.

RULE OF MUTUAL EXCLUSION We want to conclude this chapter by remarking the fact that Raman and the infrared activities are mutually exclusive for a system in which a center of a symmetry is present: this is due to the fact that a mode must have a variable dipole moment in order to be infrared active, while it needs to have a variable polarization in order to be Raman active. As shown in Fig 2.2 when a center of symmetry is present this two conditions are mutually exclusive. This principle is known in the literature as *rule of mutual exclusion* [13].

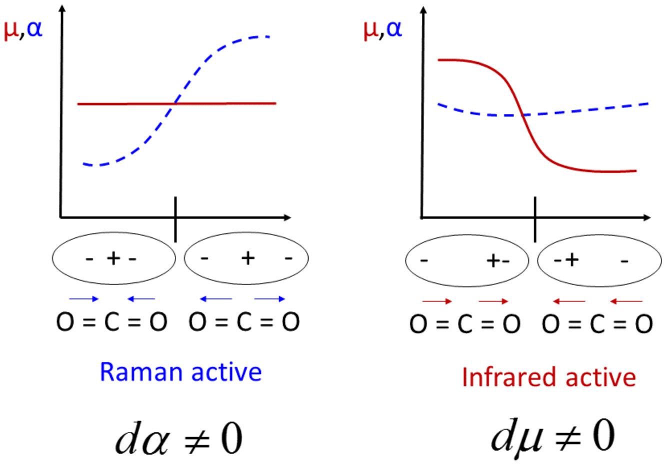

Figure 2.2.: A schematic explanation of the rule of mutual exclusion for the CO_2 molecule. All images are adapted from [3]

3

METHODS

In the previous chapters we reviewed a set of very important physical properties of condensed-matter systems, such as the electronic and vibrational band structure. Furthermore we showed how the latter can be probed through the Raman and the IR spectroscopy. Here, we will introduce two computational techniques, as proposed by Leach [74], Martin [81] and Jensen [60], by which the previously discussed properties can be predicted: these are the Hartree-Fock (HF) method and the density functional theory (DFT) scheme. Furthermore, following the Martin [81] approach, we are going to review the density functional perturbation theory (DFPT); this technique, developed by Baroni et al. [10] within the DFT formalism, allows to predict, in a very efficient way, the vibrational properties of a system.

THE MANY BODY PROBLEM The starting point for the calculation of the properties of a material is the well known many-body hamiltonian [81]

$$\begin{aligned}\hat{H} = &-\frac{\hbar^2}{2m_e}\sum_i \nabla_i^2 - \sum_{i,I}\frac{Z_I e^2}{|\mathbf{r}_i - \mathbf{R}_I|} + \frac{1}{2}\sum_{i\neq j}\frac{e^2}{|\mathbf{r}_i - \mathbf{r}_j|} \\ &-\sum_I \frac{\hbar^2}{2M_I}\nabla_I^2 + \frac{1}{2}\sum_{I\neq J}\frac{Z_I Z_J e^2}{|\mathbf{R}_I - \mathbf{R}_J|}\end{aligned} \tag{3.1}$$

Where $\mathbf{r}_i$ indicates the coordinate of electron i with mass m_e, while $\mathbf{R}_I$ stands for the coordinates of the nucleus I of mass M_I and charge Z_I. This formidable problem can be slightly simplified if one considers that the mass of the nuclei is very large with respect to the mass of the electrons: this is the foundation of the *adiabatic* or *Born-Oppenheimer approximation* that allows to decouple the nuclear degrees of freedom with respect to the electronic ones [15]. Neglecting the nuclear kinetic energy, one can rearrange the previous hamiltonian in the following form [81]

$$\begin{aligned}
\hat{H} &= \hat{T} + \hat{V}_{ext} + \hat{V}_{int} + E_{II} \\
\hat{T} &= \sum_i -\frac{1}{2}\nabla_i^2 \\
\hat{V}_{ext} &= \sum_{i,I} V_I\left(|\mathbf{r}_i - \mathbf{R}_I|\right) \\
\hat{V}_{int} &= \frac{1}{2}\sum_{i\neq j}\frac{1}{|\mathbf{r}_i - \mathbf{r}_j|}
\end{aligned} \tag{3.2}$$

where the constants $\hbar$,m_e,e and $4\pi/\epsilon$ were set equal to one and E_{II} is the classical electrostatic interaction between the nuclei. We are going to review now the two most used methods to solve this problem.

3.1 HARTREE-FOCK APPROACH

BASIC ASSUMPTIONS The simplest functional form by which one can write an anti-symmetrical wavefunction for a many electrons system is the Slater determinant [118, 74] :

$$\Phi = \frac{1}{(N!)}\begin{vmatrix} \chi_1(1) & \chi_2(1) & \dots & \chi_N(1) \\ \chi_1(2) & \chi_2(2) & \dots & \chi_N(2) \\ \chi_1(3) & \chi_2(3) & \dots & \chi_N(3) \\ \vdots & \vdots & \vdots & \vdots \\ \chi_1(N) & \chi_2(N) & \dots & \chi_N(N) \end{vmatrix} \tag{3.3}$$

where $\chi_n(m)$ is a n spin orbital function dependent on the spatial and spin coordinate of the electron m. The main assumption of the HF method is that an electronic wave function of the many body problem 3.2 can be approximated as the Slater determinant.

HF EQUATIONS If the electronic wavefunction is written as Eq. 3.3, the total energy for a closed shell system will be [74]

$$E = 2\sum_{i=1}^{N/2} H_{ii}^{core} + \sum_{i=1}^{N/2}\sum_{j=1}^{N/2}\left(2J_{ij} - K_{ij}\right) \tag{3.4}$$

where [74]

$$H_{ii}^{core} = \int d\tau_1 \chi_i(1)\left(-\frac{1}{2}\nabla_i^2 - \sum_{I=1}^{M}\frac{Z_I}{r_{iI}}\right)\chi_i(1) \tag{3.5}$$

$$J_{ij} = \int\int d\tau_1 d\tau_2 \chi_i(1)\chi_j(2)\left(\frac{1}{r_{12}}\right)\chi_i(1)\chi_j(2) \tag{3.6}$$

$$K_{ij} = \int\int d\tau_1 d\tau_2 \chi_i(1)\chi_j(2)\left(\frac{1}{r_{12}}\right)\chi_i(2)\chi_j(1) \tag{3.7}$$

The first term takes into account the kinetic and potential energy of an electron that interacts with the nuclei of charge Z_I; on the other hand the second term is the Coulomb repulsive contribution between a pair of electrons; finally the last term is the exchange interaction which has no classical analogy. Once the total energy is known, it is possible to minimize it with the orthogonality constraint [74]

$$\delta E + \delta \sum_i \sum_j \lambda_{ij} S_{ij} = 0 \tag{3.8}$$

where S_{ij} is the overlap integral [74]

$$S_{ij} = \int \chi_i \chi_j d\tau = \delta_{ij} \tag{3.9}$$

and λ_{ij} are the Lagrange multipliers. This procedure brings to the HF equations which, through some algebraical manipulation, can be rewritten as [74]

$$\left[H^{core}(1) + \sum_{j=1}^{N} \{G_j(1) - K_j(1)\} \right] \chi_i(1) = \sum_{j=1}^{N} \epsilon_{ij}\chi_j(1) \tag{3.10}$$

where G is the Coulomb operator [74]:

$$G_j(1) = \int d\tau_2 \chi_j(2) \frac{1}{r_{12}} \chi_j(2) \tag{3.11}$$

and K the exchange operator [74]:

$$K_j(1)\chi_i(1) = \left[\int d\tau_2 \chi_j(2) \frac{1}{r_{12}} \chi_i(2) \right] \chi_j(1) \tag{3.12}$$

The equation 3.10 can be also written in a more compact form [74]:

$$F_i \chi_i = \sum_j \epsilon_{ij} \chi_i \tag{3.13}$$

where the Fock operator defined as [74]

$$F_i(1) = H^{core}(1) + \sum_{j=1}^{N/2} \{2G_j(1) - K_j(1)\} \tag{3.14}$$

Through a unitary transformation [74, 60], equation 3.13 can be transformed in to a more useful form [74]

$$F_i \chi_i = \epsilon_i \chi_i \tag{3.15}$$

These are the HF equations: as one can note the form of the potentials is dependent on the form of the solution; consequently, this set can not be solved directly but instead have to be solved with the so called *self-consistent field* (SCF) method. In this approach one starts with a test wavefunction which fixes the form of the potentials and then solves the HF equation; a new more refined wavefunction will be obtained, which in turn will give a new form of the potentials. This iterative algorithm is repeated until the energy of the final wavefunction converges to the energy of the entering one within a certain threshold. It is worth noting that the HF equations are not usually solved in the here presented form; a common strategy to undertake these equations is to recast them within the linear combination of atomic orbitals (LCAO) approximation such that the Eq. 3.15 is transformed in to a matrix form; this approach, known as the Roothan Hall method, is reviewed in the Appendix A.

CONFIGURATION INTERACTION As previously reviewed in the HF theory, the main approximation lies in the fact that the many-electrons wave-function can be approximated with a single Slater determinant; unfortunately in this approach the electronic correlation is not correctly taken in account since the only correlation considered is the one due to the Pauli exclusion principle. Different techniques were proposed to go beyond this limitation: here we are going to focus on the *configuration interaction* (CI) approach in which also the excited states of the many-electron system are considered. In this method the many-body wavefunction of N electrons in K orbitals is written as the linear combination of the ground state Ψ_0, as calculated with the HF method, as well as of the excited states Ψ_1,Ψ_2,... (see Fig 3.1) [60]:

$$\begin{aligned} \Psi_{CI} &= a_0 \Phi_{HF} + \sum_S a_s \Phi_S + \sum_D a_D \Phi_D + \sum_T a_T \Phi_T + \ldots \\ &= \sum_{i=0} a_i \Phi_i \end{aligned} \tag{3.16}$$

where Φ_S,Φ_D,Φ_T represented the determinants that are singly, doubly and triply excited with respect to the HF configuration.

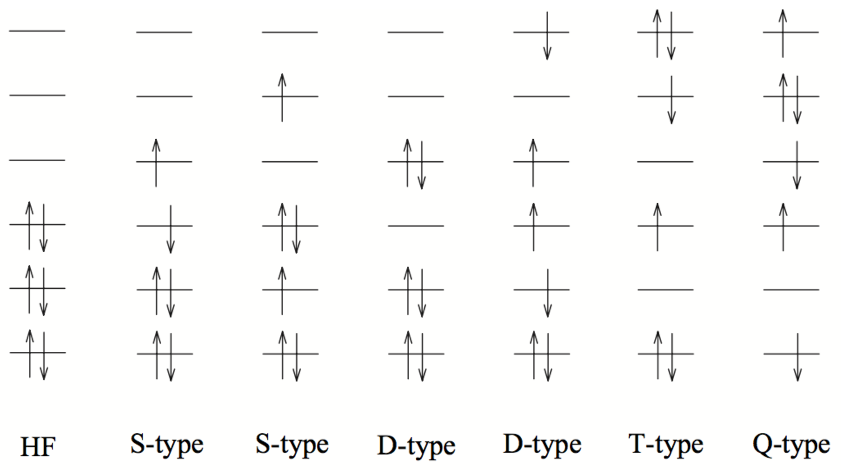

Figure 3.1.: Jensen schematic representation of excited Slater determinants which contribute to the CI wavefunction. Image taken from [60]

In principle one has to consider all the possible excited states (full configuration interaction) but this makes huge the computational effort. A first option to make this problem computationally solvable is to consider only the configurations in which the excited state differs from the ground state, only by a single spin orbital (CIS) ; furthermore one can consider only the double substitutions (CID) or perhaps the single substitution combined with the double substitution (CISD). Once chosen the suitable approximation, the energy will be obtained through the variational method [60]:

$$L = \langle \Psi_{CI} | H | \Psi_{CI} \rangle - \lambda \left(\langle \Psi_{CI} | \Psi_{CI} \rangle - 1 \right) \tag{3.17}$$

$$\frac{\partial L}{\partial a_i} = 0 \tag{3.18}$$

$$a_i \left(E_i - \lambda \right) + \sum_{j \neq 0} a_j \langle \Psi_{CI} | H | \Psi_{CI} \rangle = 0 \tag{3.19}$$

These expressions can be recast into a matrix form [60]:

$$\left(\mathbf{H} - E\mathbf{I} \right) \mathbf{a} = \mathbf{0} \tag{3.20}$$

$$\mathbf{Ha} = E\mathbf{a} \tag{3.21}$$

$$\begin{array}{c|ccccccc} & \Phi_{\mathrm{HF}} & \Phi_{\mathrm{S}} & \Phi_{\mathrm{D}} & \Phi_{\mathrm{T}} & \Phi_{\mathrm{Q}} & \Phi_{5} & \cdots \\ \hline \Phi_{\mathrm{HF}} & E_{\mathrm{HF}} & 0 & x & 0 & 0 & 0 & 0 \\ \Phi_{\mathrm{S}} & 0 & E_{\mathrm{S}} & x & x & 0 & 0 & 0 \\ \Phi_{\mathrm{D}} & x & x & E_{\mathrm{D}} & x & x & 0 & 0 \\ \Phi_{\mathrm{T}} & 0 & x & x & E_{\mathrm{T}} & x & x & 0 \\ \Phi_{\mathrm{Q}} & 0 & 0 & x & x & E_{\mathrm{Q}} & x & x \\ \Phi_{5} & 0 & 0 & 0 & x & x & E_{5} & x \\ \vdots & 0 & 0 & 0 & 0 & x & x & \ddots \end{array}$$

Figure 3.2.: The CI matrix as reported by Jensen. Note that up to the single excitation the matrix is block diagonal so there will be no change in the ground state energy. Image taken from [60]

$$\mathbf{H} = \begin{pmatrix} H_{00} - E & E_{01} & \dots & H_{0j} & \dots \\ E_{10} & H_{11} - E & \dots & H_{1j} & \dots \\ \vdots & \vdots & \ddots & \vdots & \dots \\ E_{j0} & \vdots & \dots & H_{jj} - E & \dots \\ \vdots & \vdots & \dots & \vdots & \ddots \end{pmatrix} \tag{3.22}$$

$$\mathbf{a} = \begin{pmatrix} a_0 \\ a_1 \\ \vdots \\ a_j \\ \vdots \end{pmatrix} \tag{3.23}$$

It is worth noting, that due to the Brillouin theorem [60, 74] the energy of the ground state will not change if only the single excitations (CIS) are considered (see Fig 3.2); however, through this approach, the energies of the single excited states will be obtained. This point is useful as one is interested in the prediction of the absorption spectrum.

3.2 DENSITY FUNCTIONAL THEORY

Beside the HF method there is a different way to attack the many electron Hamiltonian in Eq. 3.2: while in the HF method the approximation is performed at the beginning on the wavefunction (which, as shown, neglects the correlation effects), the *density functional theory* (DFT) rearranges the Hamiltonian 3.2 in to a different form where the exchange and correlation effects are isolated in to a single integral; this term will be then evaluated through some approximations. So, while in the HF method the equations obtained are not exact because they were derived using an approximated wavefunction, in the DFT the final equations are exact but their resolution requires an approximation.

ELECTRON DENSITY AND HOHENBERG-KOHN THEOREMS While in the HF formalism the key quantity was the Slater determinant, in the DFT this role is played by the electronic density. This last quantity is defined as [81]:

$$n(\mathbf{r}) = \sum_{\sigma} n(\mathbf{r}, \sigma) = \sum_{\sigma} \sum_{i=1}^{N^{\sigma}} |\psi_i^{\sigma}(\mathbf{r})|^2 \tag{3.24}$$

where σ labels the spin. The possibility to recast the many-body hamiltonian through the density is guaranteed by the Hohenberg and Kohn (HK) theorems [57, 81]:

Theorem I: there is a one-to-one correspondence between the external potential V_{ext} *and the electron density* $n_0(\boldsymbol{r})$

Theorem II: For any V_{ext} *it is possible to define a universal function of the energy E[n]; the density and the energy of the ground state can be calculated through a variational method*

The advantage of this approach is that we replaced a quantity that involves 3N degrees of freedom with another one in which only three of them are used.

KOHN AND SHAM EQUATIONS The HK theorems only proof that the electron density can be used in order to solve exactly the many-electron hamiltonian of Eq. 3.2; nothing was stated about the way by which the many-body problem can be rewritten using the density. This work was performed by Kohn and Sham[67] : they proposed to use an auxiliary system of non-interacting particles where the exchange and correlation effects of the many body system are described by a single functional. The hamiltonian of the auxiliary system is defined as [81]

$$\hat{H}^{\sigma}_{aux} = -\frac{1}{2}\nabla^2 + V^{\sigma}\left(\mathbf{r}\right) \tag{3.25}$$

$V^{\sigma}\left(\mathbf{r}\right)$ is an appropriate potential for the single particle system 3.25 which will produce the same density of the interacting system. This can be performed as consequence of the first HK theorem. The energy of the interacting system 3.2 is [81]

$$E_{KS} = \left\langle \hat{T} \right\rangle + \left\langle \hat{V}_{int} \right\rangle + \int d\mathbf{r} V_{ext}\left(\mathbf{r}\right) n\left(\mathbf{r}\right) + E_{II} \tag{3.26}$$

This equation can be rearranged in the following form [81]

$$E_{KS} = T_S + \int d\mathbf{r} V_{ext}\left(\mathbf{r}\right) n\left(\mathbf{r}\right) + E_{Hartree} + E_{II} + E_{xc} \tag{3.27}$$

where [81]

$$E_{Hartree}\left[n\right] = \frac{1}{2}\int d^3r d^3r' \frac{n\left(\mathbf{r}\right) n\left(\mathbf{r'}\right)}{\left|\mathbf{r}-\mathbf{r'}\right|} \tag{3.28}$$

$$E_{xc}\left[n\right] = \left\langle \hat{T} \right\rangle - T_S + \left\langle V_{int} \right\rangle - E_{Hartree} \tag{3.29}$$

$$T_S = -\frac{1}{2}\sum_{\sigma}\sum_{i=1}^{N^{\sigma}} \left\langle \psi_i^{\sigma} | \nabla^2 | \psi_i^{\sigma} \right\rangle = \frac{1}{2}\sum_{\sigma}\sum_{i=1}^{N^{\sigma}} \int d^3r |\nabla \psi_i^{\sigma}\left(\mathbf{r}\right)|^2 \tag{3.30}$$

The expression 3.27 has to be minimized with respect to the density and by imposing the constraint of the orthonormalizaton in order to obtain the potential of the Hamiltonian 3.25: this will give the correct ground state density of the many particles system [81]

$$\frac{\delta E_{KS}}{\delta \psi_i^{\sigma *}\left(\mathbf{r}\right)} = \frac{\delta T_s}{\delta \psi_i^{\sigma *}} + \left[\frac{\delta E_{ext}}{\delta n\left(\mathbf{r},\sigma\right)} + \frac{\delta E_{Hartree}}{\delta n\left(\mathbf{r},\sigma\right)} + \frac{\delta E_{xc}}{\delta n\left(\mathbf{r},\sigma\right)}\right] \frac{\delta n\left(\mathbf{r},\sigma\right)}{\delta \psi_i^{\sigma *}\left(\mathbf{r}\right)} = 0 \tag{3.31}$$

$$\begin{aligned} H^{\sigma}_{KS}\left(\mathbf{r}\right) &= -\frac{1}{2}\nabla^2 + V^{\sigma}_{KS}\left(\mathbf{r}\right) \\ V^{\sigma}_{KS}\left(\mathbf{r}\right) &= V_{ext}\left(\mathbf{r}\right) + \frac{\delta E_{Hartree}}{\delta n\left(\mathbf{r},\sigma\right)} + \frac{\delta E_{ex}}{\delta n\left(\mathbf{r},\sigma\right)} \\ &= V_{ext}\left(\mathbf{r}\right) + V_{hartree}\left(\mathbf{r}\right) + V^{\sigma}_{xc}\left(\mathbf{r}\right) \end{aligned} \tag{3.32}$$

Eq. 3.32 are know as the Kohn and Sham equations: they connect the independent particle system with the interacting one. It is worth to stress that the problem is not solved, but instead, is only rewritten in a way that all our ignorance concerning the many-body problem is put in the E_{xc} term. As for the HF equations, the KS equations have to be resolved in a self-consistent way, but in this case, the problem scales as N^2 instead of N^4. One can ask why the HF equations are still used although they are more computationally expensive: the answer lies in the fact that in the DFT the exchange effect is not distinguished with respect to the correlation effect. In the HF the exchange term exactly cancels the self interacting term, while in the KS equation, since the E_{xc} is approximated, the self interacting term is not exactly suppressed. This is one of the most important drawback in the use of the DFT.

FUNCTIONALS Due to the fact that an exact analytical expression for the E_{xc} functional is not known, different approximations were proposed: the first one is to use the same exchange-correlation energy of an homogeneous electron gas [74]

$$E_{xc}^{LDA} = \int dr n\left(\mathbf{r}\right) \epsilon_{xc}^{hom}(n\left(\mathbf{r}\right)) \tag{3.33}$$

This approximation is known in the literature as the local density approximation (LDA) and it was first proposed by Kohn and Sham. Beside the LDA approximation, which provides good results despite it simplicity; other E_{xc} forms were proposed: in the generalized gradient approximation, proposed by Becke [11], the exchange correlation functional does not depend only on the density but also on its gradient [74]:

$$E_{xc}^{GGA} = \int dr n\left(\mathbf{r}\right) \epsilon_{xc}(n\left(\mathbf{r}\right), \nabla n\left(\mathbf{r}\right)) \tag{3.34}$$

Further proposed improvements introduce an exact exchange term, from HF theory, together with a DFT correlation term. Such methods are called hybrid functional and a review about them can be find in [74, 81].

PLANE WAVE EXPANSION For a periodic system, it is very useful to expand the wavefunction in plane waves according to the Bloch theorem [74]:

$$\psi_i^{\mathbf{k}}\left(\mathbf{r}\right) = \sum_{\mathbf{G}} a_{i,\mathbf{k}+\mathbf{G}} e^{(i(\mathbf{k}+\mathbf{G})\cdot\mathbf{r})} \tag{3.35}$$

With this expansion the KS equation will have the following form [74]

$$\begin{aligned}\sum_{G'}\{\frac{\hbar^2}{2m}\left|\mathbf{k}+\mathbf{G}\right|\delta_{GG'}+V_{ion}\left(\mathbf{G}-\mathbf{G'}\right)+\\+V_{elec}\left(\mathbf{G}-\mathbf{G'}\right)+V_{xc}\left(\mathbf{G}-\mathbf{G'}\right)\}a_{i,\mathbf{k}+\mathbf{G'}}=\epsilon_i a_{i,\mathbf{k}+\mathbf{G'}}\end{aligned} \tag{3.36}$$

in which V_{elec} and V_{ion} represent respectively the electron-electron and the electron-nuclei interaction, while V_{XC} stands for the exchange correlation functional. In principle, an infinite number of **G** reciprocal lattice vectors are involved in this expression; however, the most important quantities can be obtained using plane wave functions with kinetic energy up to limited cut-off. This is defined as [74]

$$E_{cutoff}=\frac{h^2}{2m}\left|\mathbf{k}+\mathbf{G}\right|^2 \tag{3.37}$$

This quantity is strongly dependent on the chemical elements involved. In principle, also the number of the reciprocal lattice vectors **k** has to be infinite in order to produce a continuous grid: in practice, a discrete sampling is sufficient; the most used approach for the choice of **k** is the Monkhorst-Pack scheme [86] in which a uniform grid is used. Usually, a dense grid is required for a small real-space cell, on contrary, for the larger ones, only a small number of **k** points is necessary. If the unitary cell is large enough only the Γ point can be used: this is the so called molecular approximation.

PSEUDOPOTENTIALS A common strategy to reduce the computational cost is to consider only the valence electrons instead of performing an all-electrons calculation. These electrons are the most involved ones in the chemical bonding, however their wavefunctions have rapid oscillations near the nucleus due to the constraint of the orthogonality. Consequently, a very high cutoff is usually required: this increases the required computational resources. A common strategy used to reduce this effort is to replace the true potential with a pseudopential, that gives a wavefunction that is identical to the real one out of the so-called core radius r_c; on the other hand the pseudopotential replaces the real wavefunction with a smoother one within the r_c (see Fig 3.3). If the norm is conserved inside the core region the potential is norm-conserving (NC); otherwise, as proposed by Vanderbilt [129], the norm conservation constraint can be relaxed in order to improve the smoothness of the wavefunction and consequently the computational cost required: this is the case of ultrasoft (US) pseudopotentials. Further details can be found in the Payne et al. review [100]

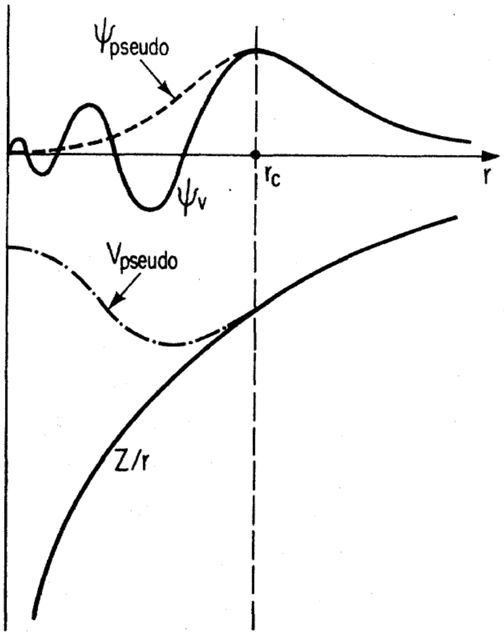

Figure 3.3.: A schematic representation of a pseudoptential as proposed by Payne et al.: out of the r_c region the wavefunction is identical to the real one while inside the r_c region the real wavefunction is replaced with a smoother one . Image taken from [100]

3.3 VIBRATIONAL PROPERTIES THROUGH AB-INITIO METHODS

In the previous sections different techniques were presented which can be used to predict the electronic properties of a material: now we are going to review how its vibrational properties can be also predicted within a first principles approach. The starting point is the following eigenvalue problem that describes the motion of the nuclei [81]:

$$\det\left|\frac{1}{\sqrt{M_I M_J}}\mathbf{D}_{s,\alpha;s';\alpha'}(\mathbf{q}) - \omega_i^2(\mathbf{q})\right| = 0 \tag{3.38}$$

where M_I is the mass of the I nucleus, $\omega_i(\mathbf{q})$ is the frequency of the mode i with wavevector $\mathbf{q}$, and $\mathbf{D}$ is the dynamical matrix defined as [81]

$$\mathbf{D}_{s,\alpha;s',\alpha'}(\mathbf{q}) = \frac{\partial^2 E(\mathbf{r})}{\partial \mathbf{u}_{s,\alpha}(\mathbf{q})\partial \mathbf{u}_{s',\alpha'}(\mathbf{q})} \tag{3.39}$$

In the last expression, α labels the cartesian components and $\mathbf{u}$ stands for the displacement of the atom s . First we are going to review the two most common ab-initio techniques by which the matrix elements 3.39 are evaluated; then we are going to expose the Lazzeri et al. method [73] for the prediction of the Raman spectrum in off-resonance conditions .

FROZEN PHONONS One of the oldest approach used for the evaluation of the dynamical matrix elements (Eq. 3.39) is the frozen phonon method [142]. In this case the derivatives [81]

$$C_{I,\alpha,J,\beta} \simeq -\frac{\delta F_{I,\alpha}}{\delta R_{J,\beta}} \tag{3.40}$$

are obtained numerically by calculating the forces that are produced when a single atom is slightly displaced, keeping fixed the others. Then the dynamical matrix is evaluated through the Fourier transform [2] :

$$\mathbf{D}(\mathbf{q}) = \sum_l \mathbf{C}(\mathbf{R}_l)e^{-i\mathbf{q}\mathbf{R}_l} \tag{3.41}$$

This methods is very simple to implement, but it has the weakness to be computationally expensive if one wants to study the vibrational modes with $\mathbf{q}$ close to Γ because, in this case, large supercells have to be used [114]. In order to overcome this point, Baroni et al. [10] developed a different method to evaluate the dynamical matrix: the density functional perturbation theory (DFPT).

DENSITY FUNCTIONAL PERTURBATION THEORY Instead of being calculated numerically, as in the frozen phonon method, the dynamical matrix elements of Eq. 3.39 can be evaluated by taking advantage of the linear response theory [49] . According to the *Hellmann-Feynman theorem* [44, 60] the derivative of the total energy with respect to the atom position λ is [81, 10]:

$$\frac{\partial E}{\partial \lambda_i} = \frac{\partial E_{II}}{\partial \lambda_i} + \int \frac{\partial V_{ext}(\mathbf{r})}{\partial \lambda_i} n(\mathbf{r}) d\mathbf{r} \tag{3.42}$$

Where E_{II} is the interaction between the nuclei and V_{ext} the electron-nucleus interactions (see Eq. 3.2) This expression can be used to rewrite the dynamical matrix elements 3.39 in a different form [81, 10]:

$$\frac{\partial^2 E}{\partial \lambda_i \partial \lambda_j} = \frac{\partial^2 E_{II}}{\partial \lambda_i \partial \lambda_j} + \int \frac{\partial^2 V_{ext}(\mathbf{r})}{\partial \lambda_i \partial \lambda_j} n(\mathbf{r}) d\mathbf{r} + \int \frac{\partial n(\mathbf{r})}{\partial \lambda_i} \frac{\partial V_{ext}(\mathbf{r})}{\partial \lambda_j} d\mathbf{r} \tag{3.43}$$

This last integral, in which the derivative of density is involved, can be recast in a more interesting fashion [10, 81] :

$$\int \frac{\partial V_{ext}(\mathbf{r}')}{\partial \lambda_i} \frac{\partial n(\mathbf{r})}{\partial V_{ext}(\mathbf{r}')} \frac{\partial V_{ext}(\mathbf{r})}{\partial \lambda_j} d\mathbf{r} d\mathbf{r}' = \int \frac{\partial V_{ext}(\mathbf{r}')}{\partial \lambda_i} \chi(\mathbf{r}, \mathbf{r}') \frac{\partial V_{ext}(\mathbf{r})}{\partial \lambda_j} d\mathbf{r} d\mathbf{r}' \tag{3.44}$$

where χ is the density response function, that is related to the dielectric function by the following relation [10, 81]

$$\begin{aligned} \epsilon^{-1} &= 1 + V_C \chi \\ V_C(q) &= \frac{4\pi e^2}{q^2} \end{aligned} \tag{3.45}$$

A first possible approach consists in the evaluation of χ through the calculation of the inverse of the dielectric function: this method provides the response to all possible perturbations; however this strategy turns out to be too computational expensive. The DFPT, instead, provides a set of self-consistent equations that allow to calculate the response of the system for a monochromatic perturbation. The first equation of this set is obtained from the linearisation of the density, as defined in 3.24, with respect to the wavefunction [10, 81]:

$$\Delta n(\mathbf{r}) = 4\mathrm{Re}\sum_{n=1}^{N/2} \psi_n^*(\mathbf{r})\Delta\psi_n(\mathbf{r}) \tag{3.46}$$

Where Δ is defined as [10, 81]:

$$\Delta^\lambda F = \sum_i \frac{\partial F_\lambda}{\partial \lambda_i}\Delta\lambda_i \tag{3.47}$$

On the other hand $\Delta\psi_n(\mathbf{r})$ can be evaluated through the first-order perturbation theory [10, 81] :

$$(H_{KS} - \epsilon_n)\,|\Delta\psi_n\rangle = -(\Delta V_{KS} - \Delta\epsilon_n)\,|\psi_n\rangle \tag{3.48}$$

$$\Delta V_{KS}(\mathbf{r}) = \Delta V_{ext}(\mathbf{r}) + e^2\int d\mathbf{r}'\frac{\Delta n(\mathbf{r}')}{|\mathbf{r}-\mathbf{r}'|} + \int d\mathbf{r}'\frac{dV_{xc}}{dn(\mathbf{r}')}\Delta n(\mathbf{r}) \tag{3.49}$$

The operator on the left side in the Eq. 3.48 is singular for the eigenvector ψ_n; however, as shown by Baroni et al. in [10], this problem can be solved using the projectors P_v and P_c defined as [81]

$$\begin{aligned} P_v &= \sum_{i=1}^{N} |\psi_i\rangle\langle\psi_i| \\ P_c &= 1 - P_v \end{aligned} \tag{3.50}$$

so that the eq 3.48 becomes [10]

$$(H_{KS} + \alpha P_v - \epsilon_n)\,|\Delta\psi_n\rangle = -P_c(\Delta V_{KS})\,|\psi_n\rangle \tag{3.51}$$

As for the KS and HF equations, Eq. 3.47,3.51 and 3.49 have to be solved in self-consistent way (see Fig 3.4) . Finally it is worth noting that in this approach, contrary to the frozen phonon, no supercell is required.

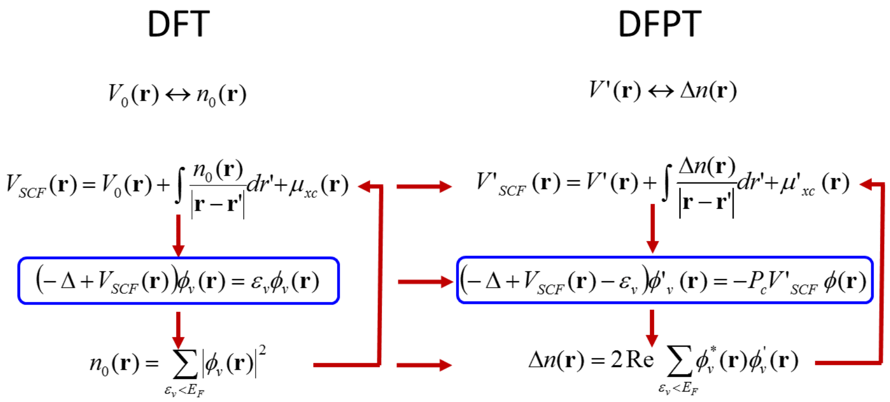

Figure 3.4.: A schematic representation of the main passages of the DFT and of the DFPT as proposed by Baroni. Image taken from [9]

OFF-RESONANCE RAMAN INTENSITY FROM AB-INITIO PRINCIPLES In this final paragraph we are going to briefly review the method proposed by Lazzeri et al. [73] to evaluate from first principles the Raman intensity in off-resonance conditions. Using the Plackzec approximations [18, 78] shown in Chapter 2, the Raman intensity of a mode ω_ν is [73]:

$$I^\nu \propto \left| e_i \cdot \vec{\mathbf{A}}_\nu e_s \right|^2 \frac{1}{\omega_\nu}(n_\nu + 1) \tag{3.52}$$

where e_i and e_s are the incident and outgoing polarization,n the phonon population and $\mathbf{A}$ the Raman tensor defined as [73]:

$$\mathbf{A}^\nu_{lm} = \sum_{k\gamma} \frac{\partial^3 E}{\partial E_l \partial E_m \partial u_{k\gamma}} \frac{w^\nu_{k\gamma}}{\sqrt{M_\gamma}} \tag{3.53}$$

in which E is the electronic energy of the system, $w^\nu_{k\gamma}$ is the eigenvector of the mode ν, $u_{k\gamma}$ is the displacement of the atom γ in the k direction, M_γ the atomic mass and E_l the l cartesian component of the electric field. According to the *Hellman-Feynman theorem* [44, 60], the derivative of the energy with respect to the displacement $u_{k\gamma}$ can be calculated as follows [73]:

$$\frac{\partial E^{el}}{\partial u_{k\gamma}} = 2\mathrm{Tr}\left\{ \rho \frac{\partial v^{ext}}{u_{k\gamma}} \right\} \tag{3.54}$$

where v^{ext} is the external ionic potential. Taking advantage of this last expression, the derivative in the Eq. 3.53 can be rewritten as follows [73] :

$$\frac{\partial^3 E}{\partial E_l \partial E_m \partial u_{k\gamma}} = 2\mathrm{Tr}\left\{ \left(\frac{\partial^2 \rho}{\partial E_l \partial E_m} \right) \frac{\partial v^{ext}}{\partial u_{k\gamma}} \right\} \tag{3.55}$$

The evaluation of this last expression is well defined for molecules; however, it is non-trivial for periodic systems, due to the fact that in this last case the position operator, required by the electric field perturbation, is not well defined [49, 81]. A first tentative to overcome this problem was proposed by Nunes and Gonze [95] using the Berry phase; however, this approach was used only to a one- dimensional system. Lazzeri et al., on the contrary proposed to evaluate the second order derivative in 3.55 with the following expression [73]:

$$\frac{\partial^2 \rho}{\partial \lambda \partial \mu} = \sum_\nu (|P\eta^{\lambda,\mu}_\nu\rangle\langle\psi_\nu| + |P\frac{\partial \psi_\nu}{\partial \lambda}\rangle\langle\frac{\partial \psi_\nu}{\partial \mu}P| - \sum_{\nu'} |\psi_{\nu'}\rangle\langle\frac{\partial \psi_{\nu'}}{\partial \lambda}P|\,|P\frac{\partial \psi_\nu}{\partial \mu}\rangle\langle\psi_\nu| + \text{ c.c} \tag{3.56}$$

in which ν and ν' run over the occupied states, P is the projector on to the empty states $P = (\mathbb{1} - \rho)$ and $|\eta_{\nu}^{\lambda,\mu}\rangle$ is the second derivative of the KS occupied orbitals. Using this approach, Lazzeri et al. obtained the following expressions for the derivatives[73]:

$$|P\frac{\partial\psi_{\nu}}{\partial\lambda}\rangle = G_{\nu}\left[\frac{\partial V^{KS}}{\partial\lambda},\rho\right]|\psi_{\nu}\rangle \tag{3.57}$$

$$|P\eta_{\nu}^{(\lambda,\mu)}\rangle = G_{\nu}\left\{\frac{\partial^2 V^{KS}}{\partial\lambda\partial\mu} + \left[\frac{\partial V^{KS}}{\partial\lambda};\frac{\partial\rho}{\partial\mu}\right] + \left[\frac{\partial V^{KS}}{\partial\mu};\frac{\partial\rho}{\partial\lambda}\right]\right\}|\psi_{\nu}\rangle \tag{3.58}$$

$$G_{\nu} = \sum_{c}\frac{|\psi_c\rangle\langle\psi_c|}{\varepsilon_{\nu} - \varepsilon_c} \tag{3.59}$$

$$\frac{\partial\rho}{\partial\mu} = \sum_{\nu}|P\frac{\partial\psi_{\nu}}{\partial\mu}\rangle\langle\psi_{\nu}| + \text{ c.c.} \tag{3.60}$$

where the commutators $[\frac{\partial V^{KS}}{\partial\lambda},\rho]$ and $\left[\frac{\partial V^{KS}}{\partial\lambda},\partial\rho/\partial\mu\right]$ appear: these ensure that all quantities involved are well defined in a periodic system. Finally it is worth noting that also in this case a set of self-consisted equations were obtained (Eq . 3.56,3.57,3.58,3.58), due to the fact that $\partial V_{KS}/\partial\lambda$ and $\partial^2 V_{KS}/\partial\lambda\mu$ depend on $\partial\rho/\partial\lambda$, $\partial\rho/\partial\mu$ and $\partial\rho^2/\partial\mu\partial\lambda$.

Part II.

Results

4

RAMAN AND IR FINGERPRINTS OF ATOMICALLY PRECISE GNRS

As reviewed in Chapter 1, the growth of atomically controlled nanoribbons represents a very important step for the application of these nanostructures in micro and optoelectronics. Among the different characterization techniques, Raman spectroscopy is currently one of the most suitable non destructive methods to characterize the main features of these systems. However, such characterization has been so far limited only to the observation of the D an G peaks [90, 89] hallmarks of the sp^2 hybrization. Furthermore, solution processed GNRs may present different functionalization configurations: even thought Raman spectroscopy provides very useful information about the width and the edge morphology of these carbon nanostructures, it is insensitive to their functionalization configuration: in both cases the effect of the alkyl chains on the spectrum is mostly a broadening of the radial-like-breathing-mode (RLBM). A more suitable technique for the investigation of this feature is the infrared spectroscopy. Our investigation of the Raman and IR spectra of GNR with different widths and edge morphologies was performed in collaboration with different experimental research group: in this thesis, the Raman results are presented by including the related paper, that is already under review, while the IR results are here exposed in detail (see paragraphs 4.1-4.2)

Raman fingerprints of atomically precise graphene nanoribbons

I. A. Verzhbitskiy,[1,†] Marzio De Corato,[2, 3] Alice Ruini,[2, 3] Elisa Molinari,[2, 3]Akimitsu Narita,[4] Yunbin Hu,[4]
Matthias Georg Schwab,[4, ‡] M. Bruna,[5] D. Yoon, [5] S. Milana,[5] Xinliang Feng,[6] Klaus Müllen,[4] Andrea
C. Ferrari, [5] Cinzia Casiraghi,[1, 7,*] and Deborah Prezzi[3,*]

[1]Physics Department, Free University Berlin, Germany
[2] Dept. of Physics, Mathematics, and Informatics, University of Modena and Reggio Emilia, Modena, Italy
[3] Nanoscience Institute of CNR, S3 Center, Modena, Italy
[4] Max Planck Institute for Polymer Research, Mainz, Germany
[5] Cambridge Graphene Centre, University of Cambridge, Cambridge, CB3 OFA, UK
[6] Center for Advancing Electronics Dresden (cfaed) & Department of Chemistry and Food Chemistry, Technische Universitaet Dresden, Germany
[7] School of Chemistry, University of Manchester, UK

[†] Present address: Physics Department, National University of Singapore, 117542, Singapore
[‡] Present address: BASF SE, Carl-Bosch-Straße 38, 67056 Ludwigshafen, Germany
[*] Corresponding authors: (DP) deborah.prezzi@nano.cnr.it; (CG) cinzia.casiraghi@manchester.ac.uk

Bottom-up approaches have opened the way to the production of ultra-narrow and atomically precise graphene nanoribbons (GNRs), with electronic and optical properties controlled by the specific atomic structure. Combining Raman spectroscopy and ab-initio simulations, we show that width, edge geometry and functional groups strongly influence the Raman spectrum. The low-energy region (well below 1000 cm^{-1}) is particularly sensitive to edge morphology and functionalization, while the D peak dispersion can be used to uniquely fingerprint the presence of GNRs, and differentiates them from other sp^2 carbon nanostructures.

Raman spectroscopy is one of the most used characterization techniques in carbon science and technology[1–7]. In the last decade, the rise of graphene have triggered extensive Raman studies to understand not only phonons, but also electron-phonon, magneto-phonon and electron-electron interactions, as well as the influence of the number and orientation of the layers in few-layer graphene (FLG), electric or magnetic fields, strain, doping, disorder, quality and type of edges, and functional groups[1]. The Raman spectrum of single-layer graphene (SLG) and FLG consists of two sets of peaks: the so-called G and D peaks, which originate from in-plane vibrations and dominate the optical region of graphene and other sp^2 bonded materials[8,9]; the low-energy peaks resulting from the relative motion of the planes, such as the shear[10] (C) and the layer-breathing modes[11–13] (LBMs), which can be used as a direct probe of the number of layers.

The low-energy region, where the C and LBMs are located, is particularly interesting because specific fingerprints have been observed for a variety of carbon allotropes. Most notably, in the case of carbon nanotubes (CNTs), a characteristic peak at low energy, associated to the radial breathing mode (RBM) of all the atoms of the structure, has been widely exploited to determine the tube diameter[14]. Polycyclic aromatic hydrocarbons (PAHs) are also characterized by breathing-like low-energy modes that can be related to their lateral size[15,16]. GNRs –of interest for emerging digital nanoelectronics, optoelectronics and spintronics[17,18]— are also expected to show characteristic Raman features in this spectral region due to their finite width and low symmetry [19–24].

Recently, techniques based on surface-assisted[25] or solution-based[26–28] cyclo-dehydrogenation of tailor-made aromatic polymer precursors have enabled the production of well-defined GNRs, with lateral width well below 10nm and precise structural pattern at the edges[25–30]. Moreover, in the case of GNRs prepared by solution-based processing, the edges are typically functionalized by alkyl chains to improve solubility[28]. Thus, those types of GNRs provide a unique opportunity to study the combined effect of finite width and edge patterns, and to get insights into the evolution of the vibrational properties with lateral dimension. At the same time, such GNRs call for the identification of specific Raman fingerprints, which could be extremely relevant for their characterization and design, similar to what happened in the case of CNTs.

In this respect, experiments on GNRs mostly targeted peaks in the D/G energy region[26,30–32]. However, these features are usually just discussed as a hallmark of sp^2 hybridization, and no further analysis exists so far. A few groups have reported studies on the low-energy GNR Raman bands. Cai et al.[25] reported a sharp (20-30 cm^{-1}) low-energy peak peak at ~400 cm^{-1}, and assigned it to a Radial-Like Breathing Mode[19] (RLBM), where all the atoms of the ribbon move in-plane along to the ribbon width direction, in analogy to the RBM in CNTs. Because of that, the position of this peak is determined by the GNR width only[19–24]. A similar feature was reported in Refs. [28,29] for other GNRs produced by solution-based processing, but much broader (~100 cm^{-1} in width) when compared to Ref. [25], and with several sub-components. More importantly, the peak position is downshifted of ~50 cm^{-1} compared to the position expected from the inverse dependence of the RLBM frequency with the GNR width[19–24]. This may indicate a more complex dependence of the RLBM on GNR width and edge type then previously reported[19–24], and call for further investigations.

Here, we report a combined experimental and theoretical study of the Raman spectrum of ultra-narrow (<2nm) GNRs with well-defined edge structures, produced by solution-based methods. By investigating four GNRs with different width, edge-pattern and location of the alkyl groups, we provide a general understanding of their Raman spectra. We demonstrate that the RLBM can be influenced by the edge termination, and not just by the width. Most notably, we also demonstrate that the D peak dispersion with excitation energy is a further fingerprint of these GNRs, and uniquely differentiates them from other sp^2 carbon systems, such as graphene or CNTs.

Results

We investigated four GNRs, which are functionalized with long alkyl chains ($–C_{12}H_{25}$) to favor their solubility in solvents[29]. The structures in Figure 1a-c represent a series of "cove-shaped" GNRs with the same edge pattern and increasing width, where a benzo ring periodically decorates the zigzag (ZZ) edge. Following Ref. [33], these structures are labeled *n*CNRs, where *n* indicates the width of the ZZ GNR core (here *n* = 4, 6, 8). In addition to those samples, we also investigate a GNR based on the chiral-edged (4,1)-GNR with periodically fused benzo rings. This is called *m*-ANR in Ref. [33] and here shown in Figure 1d. The *m*-ANR has the same width as the 8CNR, but its "chirality" leads to slightly different edge pattern. Note also that the 6CNR has intermediate width between 4CNR and 8CNR, with the same edge pattern, but the alkyl groups are placed in a different location at the edge: 4- and 8CNR are substituted at the outer positions on the benzo rings, while the 6CNR is substituted at the inner position inside the cove-type edge.

Low-energy region of the Raman spectra and radial-like breathing mode. Figure 2a shows the low-energy Raman spectrum of the GNRs in Figure 1. In the case of 4CNR, one broad peak appears at about 230 cm^{-1} (Full Width at Half Maximum, FWHM ~100 cm^{-1}), which comprises at least three contributions. For 6CNR, 8CNR and *m*-ANR, the most intense peak is located around 130-150 cm^{-1}, and its width is sharp for *m*-ANR (~30 cm^{-1}), while it is larger for 8CNR and 6CNR (~80-100 cm^{-1}). Furthermore, depending on the exact structure of the ribbon, the peak disappears at certain excitation energies. For instance, the peak is not seen at energies above 1.96 eV for 4CNR, while for 8CNR it is seen at 1.96 eV. Other peaks with small intensity are also seen in the spectral range 400-700 cm^{-1}, as shown in Figure 2a. This is different from the case of CNTs and armchair GNRs grown on substrate[25], where the low energy region is dominated by a sharp breathing mode, whose frequency is uniquely determined by the CNT/GNR lateral size and described by the zone-folding approximation[23,24].

In order to gain further insights into the origin of the GNRs Raman peaks at low energy, we have computed from first principles the Raman spectra of several GNRs (see Methods), by increasing the structure complexity in a stepwise manner. We first consider perfect ZZ-GNRs, corresponding to the cores of the cove-shaped ribbons studied here (indicated by the shaded areas in Figure 1a-c). We then study cove-shaped GNRs with hydrogen-terminated edges. Finally, we compare the above systems with the case where the edges are functionalized by alkyl chains, as in the real samples, though shorter ($–C_4H_9$ instead of $–C_{12}H_{25}$) to make the calculations more affordable. Figure 3a shows the simulated Raman spectrum of the 8CNR. Let us first focus on the H-passivated 8CNR, hereafter labeled 8CNR+H. The spectrum is characterized by a dominant peak at 183 cm^{-1}, which falls in between the RLBMs of the ZZ-GNRs corresponding to the minimum and maximum width of this cove-shaped GNR, i.e. 209 and 164 cm^{-1} for the 8- and 10-ZZ GNRs, respectively. This behavior, which is common to all the GNRs studied here, can be understood in terms of an effective width model. Indeed, these cove-shaped GNRs present a modulated structure, with variable width (e.g. 4CNR core width is between 0.69nm and 1.13nm). However, we can define an effective width as the weighted average of the different GNR widths (see Supplementary Information), and compare our first principles simulations with the results obtained by using the zone-folding approximation for this effective width. Figure 3b shows that the agreement is within less than 10 cm^{-1} for GNRs wider than 15 Å, as expected for this approximation[23,24]. Besides the RLBM, there are higher frequency modes (470-680 cm^{-1}), combining longitudinal and transverse components: these modes, which are not present in ZZ-GNRs, appear in cove-shaped GNRs in view of the different periodicity along the ribbon axis introduced by the additional benzo rings at the edge.

We next functionalize the edges with short alkyl chains (8CNR + C_4H_9). We observe a further considerable red-shift of the RLBM peak, which moves from 183 to 156 cm^{-1}. This value almost agrees with that obtained for the larger ZZ component of the 8CNR, i.e. 10-ZZ GNR, even though the origin of the shift is rather different, as clarified by our analysis. The breathing does not involve the ribbon only, but also part of the chain that moves in phase with the ribbon atoms (see Supplementary Information). This causes a redshift of the RLBM frequency as a result of an increase in the effective width of the system. We further check the effect of the chains by varying the chain length, as shown in Figure 3d. In addition to the effect explained above, with a redshift that depends on the chain length, we find that, depending on both the chain length and the GNR width, the RLBM can be coupled with several modes of the chain, giving rise to different sub-peaks (see e.g. the case of C_8H_{17}, Figure 3d). This result can explain the broadening of the low frequency peak observed experimentally, which is indeed different for GNRs of different width. The functionalization with alkyl chains also induces a relaxation of the system symmetry, therefore allowing for both a mixing of longitudinal (L), transverse (T) and normal (Z) modes, and the activation of modes otherwise forbidden.

High-energy region of the Raman spectra: D and G peaks, overtones and combination modes. Figure 2b shows the first order Raman spectrum of the ribbons measured at 2.41 eV, with D and G peaks typical of C sp^2 materials[1–6]. However, the G peak, which corresponds to the high frequency E_{2g} phonon at Γ, is up-shifted (~1605 cm^{-1}) and broader if compared to pristine graphene (FWHM ~ 25 cm^{-1}). Similar results were observed in small graphite domains[34] and PAH[6] due to the relaxation of the momentum conservation induced by finite size. Moreover, we do not observe any splitting of the G peak, as usually found instead for CNTs[4,5], where this mode, which is doubly degenerate in graphene[35], splits into a longitudinal-optical (LO) and a transverse-optical (TO) component. Our first principles simulations show that the G peak, located at 1618 cm^{-1} for the 8CNR (Figure 3c), is mainly due to the TO mode, with smaller contributions due to TO overtones (within 10 cm^{-1}); the LO mode is instead inactive in backscattering configuration, as expected in purely ZZ-GNRs[23]. The presence of the side chains do not alter significantly the nature and the energy position of the main features in the high-energy region of the spectrum, which are mostly dictated by the edge morphology, as seen by comparing the curves in Figure 3c.

Figure 2b also shows a prominent D peak which is characterized by a dominant component at about 1310-1330cm^{-1}, with an intensity comparable to that of the G peak, and by one or more shoulders at lower wavenumbers. These features are in agreement with first principles simulations, which show a structured peak in this region, with two main components (at 1336 and 1357 cm^{-1} for the 8CNR, Figure 3c) corresponding to the breathing modes of six-atom rings. This behavior makes the spectrum to resemble that of defective graphene[36–40]. However, there are notable differences that allow us to clearly distinguish our GNRs from defective graphene: the most striking one is found by analyzing the energy dependence of the D peak. In graphene, the D peak –coming from TO phonons around the Brillouin Zone (BZ) edge K— is activated by an inter-valley double resonance process[41] in presence of defects, and it is strongly dispersive with excitation energy due to a Kohn Anomaly at K[42]. The typical D peak dispersion of graphene is ~50 cm^{-1}/eV[43,44]. In the case of GNRs, we measured different D-peak dispersions for the different GNRs investigated (see Supporting Information). In particular, the 8CNR, due to its low band-gap (~1.2 eV[29]), allows performing Raman spectroscopy in a wide range of energies (from 1.3 to 2.54 eV) without any photoluminescence background hiding the Raman peaks (Figure 2c). If we fit the dispersion with two slopes, we get about 7 and 35 cm^{-1}/eV for the low (< 1.8 eV) and high (> 1.8 eV) excitation energy region, respectively. A considerable dispersion is found also for the RLBM (Figure 2c, bottom panel), while the G peak shows a very small dispersion, at the limit of the spectrometer resolution (Figure 2c, top panel). In addition to this, we observe the G+D combination mode and the 2G mode, which are not observed in defective graphene. A systematic comparison between defective graphene and our GNRs is reported in the Supporting Information.

To fully understand these experimental observations, one needs to consider that several factors come into play when we move from graphene to ultra-narrow atomically-precise GNRs. First of all, we have neither Kohn anomalies (see calculated phonon dispersion in Supplementary Information) nor linear electronic dispersion in such GNRs, which have semiconducting character, with an optical response dominated by excitonic effects[45,46], especially for excitation energies close to the optical gap. Second, and more importantly, the K point folds on the Γ point in these cove-shaped GNRs[33]: as such, we do not need a double-resonance process to activate this mode, but just a first-order process like in armchair GNRs, where the D peak is also observed[25]. For the same reason, we are also able to observe the G+D mode. In addition, one would expect a non-dispersive behavior for the D peak, similar to the G peak in graphene. The observed dispersion has thus to be related to some other phenomenon, e.g. disorder induced scattering introduced by the side chains.

Conclusions

We combined experimental and theoretical analysis of the Raman spectra of ultra-narrow, and structurally well-defined graphene nanoribbons with cove-type edges. The low-energy (< 1000 cm-1) region of the GNR Raman spectrum contains the main fingerprints of these materials. By analyzing the differences with respect to other systems, such as an ideal ZZGNR and the same GNR without lateral chains (H passivated), ab-initio simulations show that the number of Raman peaks and their position are crucially affected by edge modifications. The full description of cove-type edge and alkyl chains is fundamental to get an agreement with experiments, since both contribute to the shift and splitting of the peaks as well as to a re-distribution of the Raman intensity. The RLBM is especially sensitive, not simply to the width, but also to the edge modulation and functionalization, making it very different from the ideal cases studied till now, where the RLBM does not show significant dependence on the edge type. As far as the optical region is concerned, the Raman spectra of these GNRs could appear at a first sight similar to those of defective graphene, with D and G peaks of comparable intensity. However, the presence of the D+G combination mode and the observation of a strikingly different D-peak dispersion, as evidenced by a detailed multi-wavelength analysis, allow us to clearly distinguish these GNRs from defected graphene and other graphitic materials.

Methods

Experimental details. Details on the preparation of 4CNR, 8CNR and *m*-ANR are described in Refs. [27–29]. The synthesis of 6CNR will be reported elsewhere. Raman measurements are performed with a combination of different spectrometers (Witec confocal spectrometer, Renishaw InVia and TK64000 by Horiba). A 100x objective was used and the power on the sample was below 0.1 mW to avoid damage. The samples were measured as powder.

Computational approach. Simulations were performed using a first-principle plane-wave pseudopotential implementation of Density-Functional Theory (DFT) and Density-Functional Perturbation Theory (DFPT)[47], as available in the Quantum ESPRESSO package[48]. The local density approximation for the exchange-correlation functional was used. Raman intensities were calculated using the second-order response method in Ref. [49], within the Placzek approximation. Norm-conserving pseudopotentials were employed, with a plane-wave cutoff energy of 70 Ry. A vacuum region of 12 Å in the non-periodic directions was introduced to prevent interaction between periodic images. The atomic positions were fully relaxed until forces were less than 5×10^{-4} a.u. Phonon frequencies and Raman tensor were calculated using a 16×1×1 k-point grid.

Acknowledgments

We acknowledge funding from: the Alexander von Humboldt Foundation in the framework of the Sofja Kovalevskaja Award, endowed by the Federal Ministry for Education and Research of Germany; the ESF project GOSPEL (Ref. No. 09-EuroGRAPHENE-FP-001); the ERC-Co grant NOC-2D; the Italian Ministry of Research through the national projects PRIN-GRAF (Grant No. 20105ZZTSE) and FIRB-FLASHit (Grant No. RBFR12SWOJ); the European Research Council (grant NANOGRAPH); the DFG Priority Program SPP 1459; the Graphene Flagship (Ref. No. CNECT-ICT-604391); the EU project MoQuaS . Computer time was granted by PRACE at the CINECA Supercomputing Center (Grant No. PRA06 1348), and by the Center for Functional Nanomaterials at Brookhaven National Laboratory, supported by the U.S. Department of Energy, Office of Basic Energy Sciences, under contract number DE-SC0012704.

Author contributions

I.A.V., M.B., D.Y., and S.M. performed the Raman measurements, with A.C.F. and C.C. providing supervision. M.D.C., A.R., E.M. and D.P. provided the theoretical framework. A.N., Y.H. and M.G.S. prepared the graphene nanoribbons, under the supervision of X.F and K.M. C.C and D.P wrote the manuscript, with inputs from all authors.

Additional information

Competing financial interests: The authors declare no competing financial interests. Supplementary Information contains: a discussion on effect of the laser power on the first order Raman spectrum of the 4CNR+$C_{12}H_{25}$ ribbon; the comparison between the Raman spectra of the ribbons with different side chains; supplementary figures for the theoretical simulations.

How to cite this article: I. A. Verzhbitskiy et al., Raman fingerprints of atomically precise graphene nanoribbons (to be inserted).

References

1. Ferrari, A. C. & Basko, D. M. Raman spectroscopy as a versatile tool for studying the properties of graphene. *Nat. Nanotech.* **8,** 235–246 (2013).

2. Casiraghi, C. in *Spectroscopic Properties of Inorganic and Organometallic Compounds: Techniques, Materials and Applications, Volume 43,* 29–56 (The Royal Society of Chemistry, 2012).

3. Jorio, A., Saito, R., Dresselhaus, G. & Dresselhaus, M. S. *Raman Spectroscopy in Graphene Related Systems*. (Wiley-VCH Verlag GmbH, 2011).

4. Saito, R., Dresselhaus, G. & Dresselhaus, M. S. *Physical Properties of Carbon Nanotubes*. (Imperial College Press, London, 1998).

5. Reich, S., Thomsen, C. & Maultzsch, J. *Carbon Nanotubes: Basic Concepts and Physical Properties*. (Wiley-VCH Verlag GmbH, 2004).

6. Castiglioni, C., Tommasini, M. & Zerbi, G. Raman spectroscopy of polyconjugated molecules and materials: confinement effect in one and two dimensions. *Phil.~Trans.~R.~Soc.~Lond.~A* **362,** 2425–2459 (2004).

7. Ferrari, A. C. & Robertson, J. Raman spectroscopy of amorphous, nanostructured, diamond--like carbon, and nanodiamond. *Phil.~Trans.~R.~Soc.~Lond.~A* **362,** 2477–2512 (2004).

8. Tuinstra, F. Raman Spectrum of Graphite. *J. Chem. Phys.* **53,** 1126 (1970).

9. Ferrari, A. C. Raman spectroscopy of graphene and graphite: Disorder, electron–phonon coupling, doping and nonadiabatic effects. *Solid State Commun.* **143,** 47–57 (2007).

10. Tan, P. H. *et al.* The shear mode of multilayer graphene. *Nat. Mater.* **11,** 294–300 (2012).

11. Lui, C. H. *et al.* Observation of layer-breathing mode vibrations in few-layer graphene through combination Raman scattering. *Nano Lett.* **12,** 5539–44 (2012).

12. Tan, P.-H. *et al.* Ultralow-frequency shear modes of 2-4 layer graphene observed in scroll structures at edges. *Phys. Rev. B* **89,** 235404 (2014).

13. Wu, J.-B. *et al.* Interface coupling in twisted multilayer graphene by resonant Raman spectroscopy of layer breathing modes. (2015). at <http://arxiv.org/abs/1505.00095>

14. Rao, A. M. *et al.* Diameter-Selective Raman Scattering from Vibrational Modes in Carbon Nanotubes. *Science (80-.).* **275,** 187–191 (1997).

15. Maghsoumi, A., Brambilla, L., Castiglioni, C., Müllen, K. & Tommasini, M. Overtone and combination features of G and D peaks in resonance Raman spectroscopy of the C 78 H 26 polycyclic aromatic hydrocarbon. *J. Raman Spectrosc.* **46,** 757–764 (2015).

16. Di Donato, E. *et al.* Wavelength-dependent Raman activity of D2h symmetry polycyclic aromatic hydrocarbons in the D-band and acoustic phonon regions. *Chem. Phys.* **301,** 81–93 (2004).

17. Terrones, M. *et al.* Graphene and graphite nanoribbons: Morphology, properties, synthesis, defects and applications. *Nano Today* **5,** 351–372 (2010).

18. Yazyev, O. V. A guide to the design of electronic properties of graphene nanoribbons. *Acc. Chem. Res.* **46,** 2319–28 (2013).

19. Zhou, J. & Dong, J. Vibrational property and Raman spectrum of carbon nanoribbon. *Appl. Phys. Lett.* **91,** 173108 (2007).

20. Yamada, M., Yamakita, Y. & Ohno, K. Phonon dispersions of hydrogenated and dehydrogenated carbon nanoribbons. *Phys.~Rev.~B* **77,** 54302 (2008).

21. Vandescuren, M., Hermet, P., Meunier, V., Henrard, L. & Lambin, P. Theoretical study of the vibrational edge modes in graphene nanoribbons. *Phys. Rev. B* **78,** 195401 (2008).

22. Gillen, R., Mohr, M., Thomsen, C. & Maultzsch, J. Vibrational properties of graphene nanoribbons by first-principles calculations. *Phys.~Rev.~B* **80,** 155418 (2009).

23. Gillen, R., Mohr, M. & Maultzsch, J. Raman-active modes in graphene nanoribbons. *Phys.~Status~Solidi~B* **247,** 2941–2944 (2010).

24. Gillen, R., Mohr, M. & Maultzsch, J. Symmetry properties of vibrational modes in graphene nanoribbons. *Phys.~Rev.~B* **81,** 205426 (2010).

25. Cai, J. *et al.* Atomically Precise Bottom-Up Fabrication of Graphene Nanoribbons. *Nature~(London)~* **466,** 470–473 (2010).

26. Dössel, L., Gherghel, L., Feng, X. & Muellen, K. Graphene Nanoribbons by Chemists: Nanometer-Sized, Soluble, and Defect-Free. *Angew.~Chem.~Int.~Ed.~* **50,** 2540–2543 (2011).

27. Schwab, M. G. *et al.* Structurally defined graphene nanoribbons with high lateral extension. *J.~Am.~Chem.~Soc.~* **134,** 18169–18172 (2012).

28. Narita, A. *et al.* Synthesis of structurally well-defined and liquid-phase-processable graphene nanoribbons. *Nat. Chem.* **6,** 126–32 (2014).

29. Narita, A. *et al.* Bottom-up synthesis of liquid-phase-processable graphene nanoribbons with near-infrared absorption. *ACS Nano* **8,** 11622–30 (2014).

30. Schwab, M. G. *et al.* Bottom-Up Synthesis of Necklace-Like Graphene Nanoribbons. *Chem. Asian J.* n/a–n/a (2015). doi:10.1002/asia.201500450

31. Abbas, A. N. *et al.* Deposition, characterization, and thin-film-based chemical sensing of ultra-long chemically synthesized graphene nanoribbons. *J. Am. Chem. Soc.* **136,** 7555–8 (2014).

32. Konnerth, R. *et al.* Tuning the deposition of molecular graphene nanoribbons by surface functionalization. *Nanoscale* **7,** 12807–11 (2015).

33. Osella, S. *et al.* Graphene nanoribbons as low band gap donor materials for organic photovoltaics: quantum chemical aided design. *ACS Nano* **6,** 5539–48 (2012).

34. Ferrari, A. C. & Robertson, J. Interpretation of Raman spectra of disordered and amorphous carbon. *Phys.~Rev.~B* **61,** 14095–14107 (2000).

35. Basko, D. M. Calculation of the Raman G peak intensity in monolayer graphene: role of Ward identities. *New.~J.~Phys.~* **11,** 95011 (2009).

36. Lucchese, M. M. *et al.* Quantifying ion-induced defects and Raman relaxation length in graphene. *Carbon N. Y.* **48,** 1592–1597 (2010).

37. Martins Ferreira, E. H. *et al.* Evolution of the Raman spectra from single-, few-, and many-layer graphene with increasing disorder. *Phys. Rev. B* **82,** 125429 (2010).

38. Cançado, L. G. *et al.* Quantifying defects in graphene via Raman spectroscopy at different excitation energies. *Nano Lett.* **11,** 3190–6 (2011).

39. Eckmann, A. *et al.* Probing the nature of defects in graphene by Raman spectroscopy. *Nano~Lett.~* **12,** 3925–3930 (2012).

40. Eckmann, A., Felten, A., Verzhbitskiy, I., Davey, R. & Casiraghi, C. Raman study on defective graphene: Effect of the excitation energy, type, and amount of defects. *Phys.~Rev.~B* **88,** 35426 (2013).

41. Thomsen, C. & Reich, S. Double Resonant Raman Scattering in Graphite. *Phys.~Rev.~Lett.~* **85,** 5214–5217 (2000).

42. Piscanec, S., Lazzeri, M., Mauri, F., Ferrari, A. C. & Robertson, J. Kohn Anomalies and Electron-Phonon Interactions in Graphite. *Phys. Rev. Lett.* **93,** 185503 (2004).

43. Ferrari, A. C. *et al.* Raman Spectrum of Graphene and Graphene Layers. *Phys.~Rev.~Lett.~* **97,** 187401 (2006).

44. Casiraghi, C. *et al.* Raman spectroscopy of graphene edges. *Nano~Lett.~* **9,** 1433–1441 (2009).

45. Prezzi, D., Varsano, D., Ruini, A., Marini, A. & Molinari, E. Optical properties of graphene nanoribbons: The role of many-body effects. *Phys. Rev. B* **77,** 1–4 (2008).

46. Denk, R. *et al.* Exciton-dominated optical response of ultra-narrow graphene nanoribbons. *Nat. Commun.* **5,** 4253 (2014).

47. Baroni, S., de Gironcoli, S., Dal Corso, A. & Giannozzi, P. Phonons and related crystal properties from density-functional perturbation theory. *Rev.~Mod.~Phys.~* **73,** 515–562 (2001).

48. Giannozzi, P. *et al.* QUANTUM ESPRESSO: a modular and open-source software project for quantum simulations of materials. *J. Phys. Condens. Matter* **21,** 395502 (2009).

49. Lazzeri, M. & Mauri, F. First-Principles Calculation of Vibrational Raman Spectra in Large Systems: Signature of Small Rings in Crystalline S i O 2. *Phys. Rev. Lett.* **90,** 036401 (2003).

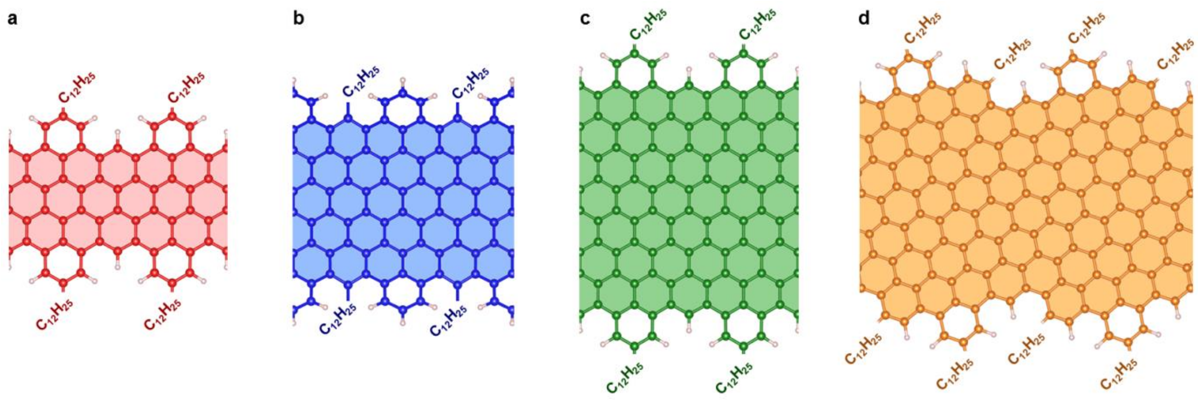

Figure 1 | Structural model of the GNRs. a-d, Ball-and-stick representation of the atomic structure of the cove-shaped GNRs investigate here, that is 4CNR (**a**), 6CNR (**b**), 8CNR (**c**), and *m*-ANR (**d**). The schematics show the characteristic variable width of these GNRs and the location of the alkyl side chains in each case. The shaded areas indicate the corresponding zigzag GNRs.

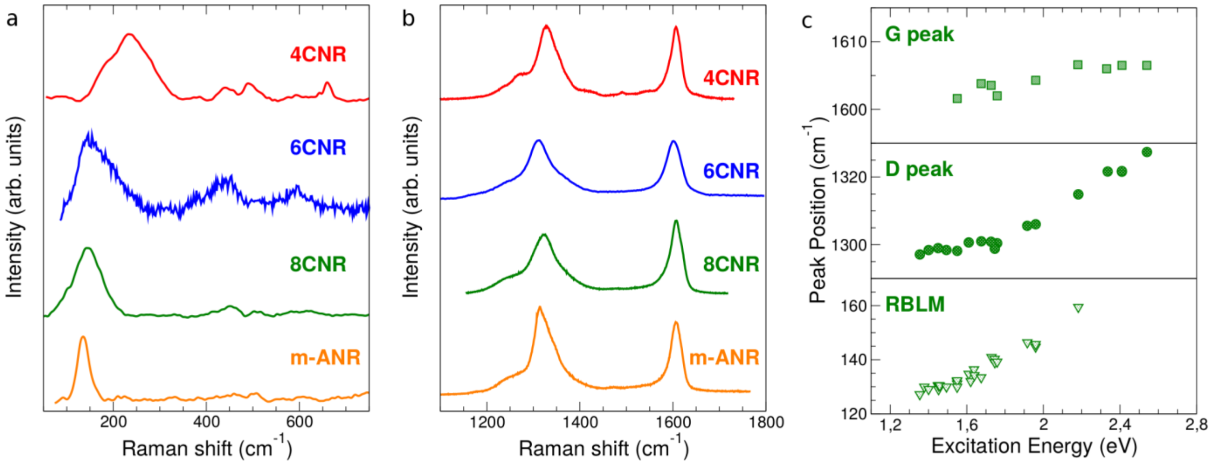

Figure 2 | Raman spectra of cove-shaped GNRs. a, Acoustic and **b,** optical region of the Raman spectrum for the cove-shaped GNRs in Figure 1. The 4CNR and 6CNR were excited at ~2.4 eV, while 8CNR and *m*-ANR at ~1.9 eV. **c,** Peak dispersion of 8CNR as a function of excitation energy for the G (top) and D peaks (middle), as well as for the RLBM (bottom).

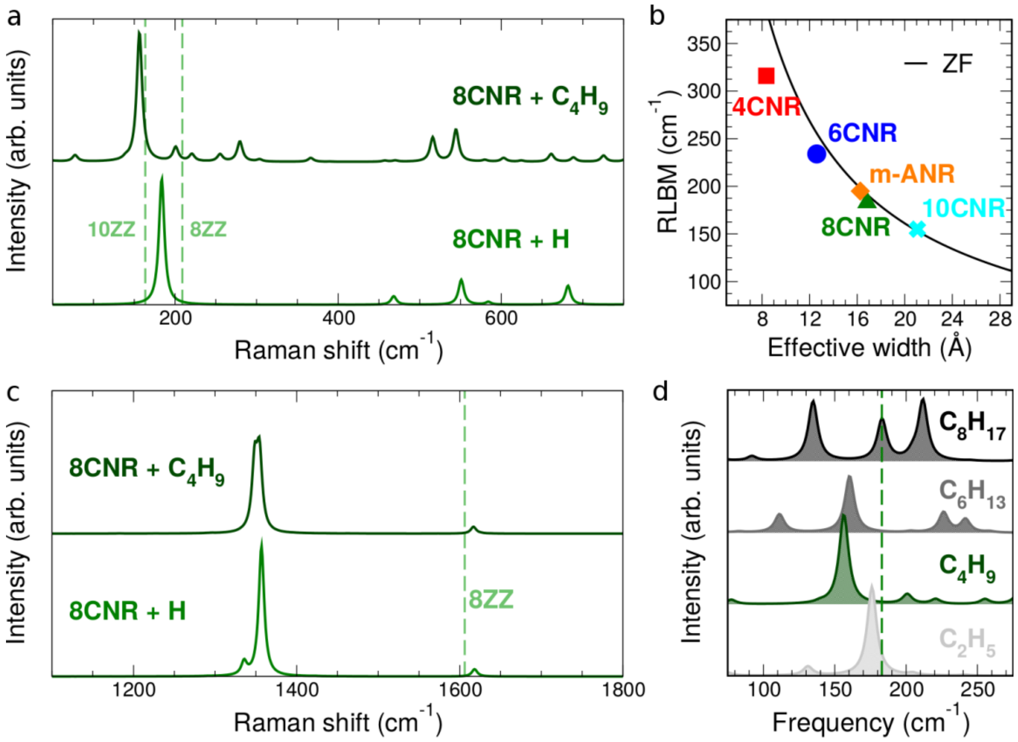

Figure 3 | Simulated vibrational properties of cove-shaped GNRs. a, Acoustic and **c,** optical region of the Raman spectrum of 8CNR. The spectrum is shown for both the hydrogen-terminated (+H, green) and the GNR functionalized with short alkyl chains (+C_4H_9, dark green). The dashed lines indicate the position of the RLBM for 8- and 10-ZGNRs (labeled 8ZZ and 10 ZZ, respectively, light green) and the position of the G peak for 8-ZGNR. **b,** First-principles calculated frequency of the RLBM for a number of different GNRs. This is compared to the result obtained within the zone-folding approximation by using an effective width, as described in the text. **d,** The acoustic region of the Raman spectrum of the 8CNR is shown at varying the chain length, by focusing on the RLBM. The dashed line indicates the frequency of the RLBM for the hydrogen-terminated system.

Supplementary Information

Raman fingerprints of atomically precise graphene nanoribbons

I. A. Verzhbitskiy,[1,†] Marzio De Corato,[2, 3] Alice Ruini,[2, 3] Elisa Molinari,[2, 3]Akimitsu Narita,[4] Yunbin Hu,[4] Matthias Georg Schwab,[4, ‡] M. Bruna,[5] D. Yoon, [5] S. Milana,[5] Xinliang Feng,[6] Klaus Müllen,[4] Andrea C. Ferrari, [5] Cinzia Casiraghi,[1, 7,*] and Deborah Prezzi[3,*]

[1]*Physics Department, Free University Berlin, Germany*

[2] *Dept. of Physics, Mathematics, and Informatics, University of Modena and Reggio Emilia, Modena, Italy*

[3] *Nanoscience Institute of CNR, S3 Center, Modena, Italy*

[4] *Max Planck Institute for Polymer Research, Mainz, Germany*

[5] *Cambridge Graphene Centre, University of Cambridge, Cambridge, CB3 OFA, UK*

[6] *Center for Advancing Electronics Dresden (cfaed) & Department of Chemistry and Food Chemistry, Technische Universitaet Dresden, Germany*

[7] *School of Chemistry, University of Manchester, UK*

† Present address: Physics Department, National University of Singapore, 117542, Singapore

‡ Present address: BASF SE, Carl-Bosch-Straße 38, 67056 Ludwigshafen, Germany

* Corresponding authors: (DP) deborah.prezzi@nano.cnr.it; (CC) cinzia.casiraghi@manchester.ac.uk

Table of Contents

S1. Laser power effects

The Raman spectra of GNRs are extremely sensitive to the laser power, especially for the *m*-ANR ribbon. In this case the D peak strongly changes its shape with increasing laser power, so very low laser powers (<< 0.5 mW) need to be used. Note that the downshift of the G peak position with increasing temperature is in agreement with temperature dependence studies of PAHs and graphene[1]. Using the average value of the G peak dependence on temperature found for PAHs (−0.015 cm^{-1}/^{o}C)[1], one could estimate an increase of up to 270 ^{o}C by increasing the laser power from 0.02 to 0.6 mW.

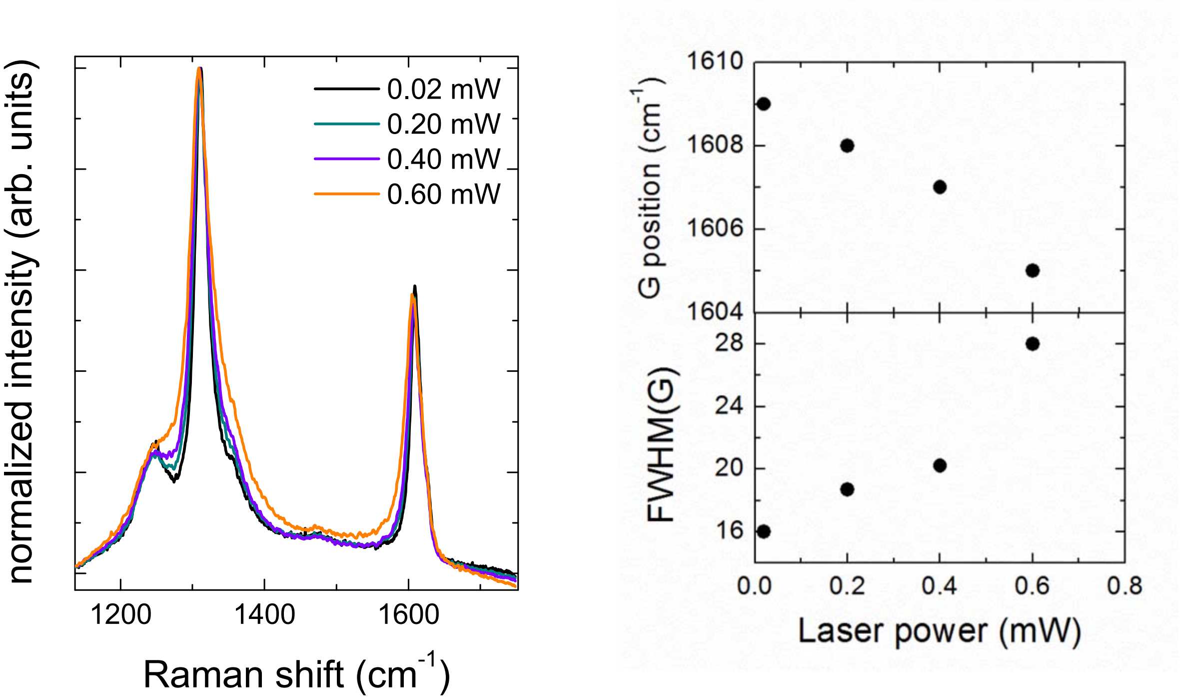

Figure S1 | (left panel) Raman spectra of m-ANR measured for increasing laser power; (right panel) G peak position and FWHM as a function of the laser power.

S2. Multi-wavelength Raman spectroscpy of GNRs vs defective graphene

Although the Raman spectrum of our GNRs looks at a first sight very similar to defective graphene (Figure S2), it shows several unique features that can be used for GNRs identification.

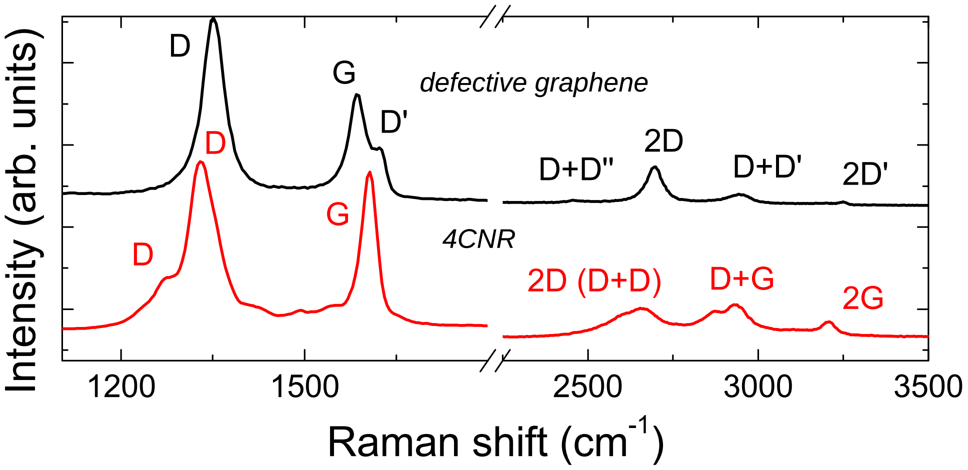

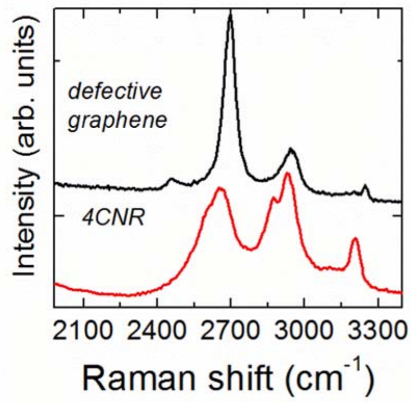

Figure S2 | (top panel) Raman spectrum of 4CNR cove-shaped ribbon and defective graphene, obtained by using hydrogenation; (Bottom panel) Zoom of the high energy region.

In the first order spectrum, the D peak of cove-shape GNRs is typically structured (i.e. composed by at least two components). The G peak is slightly asymmetric and shifted at higher position, compared to defective graphene. Moving to the high order region, because the D peak is structured, the spectrum shows the overtone and combination modes between the different components of the D peak (called 2D and D+D in Figure S2). The spectrum also shows the D+G and 2G peaks, which are not observed in defective graphene (Figure S2).

Figure S3 | First order and acoustic region of 4CNR (top panels) and 8CNR (bottom panels).

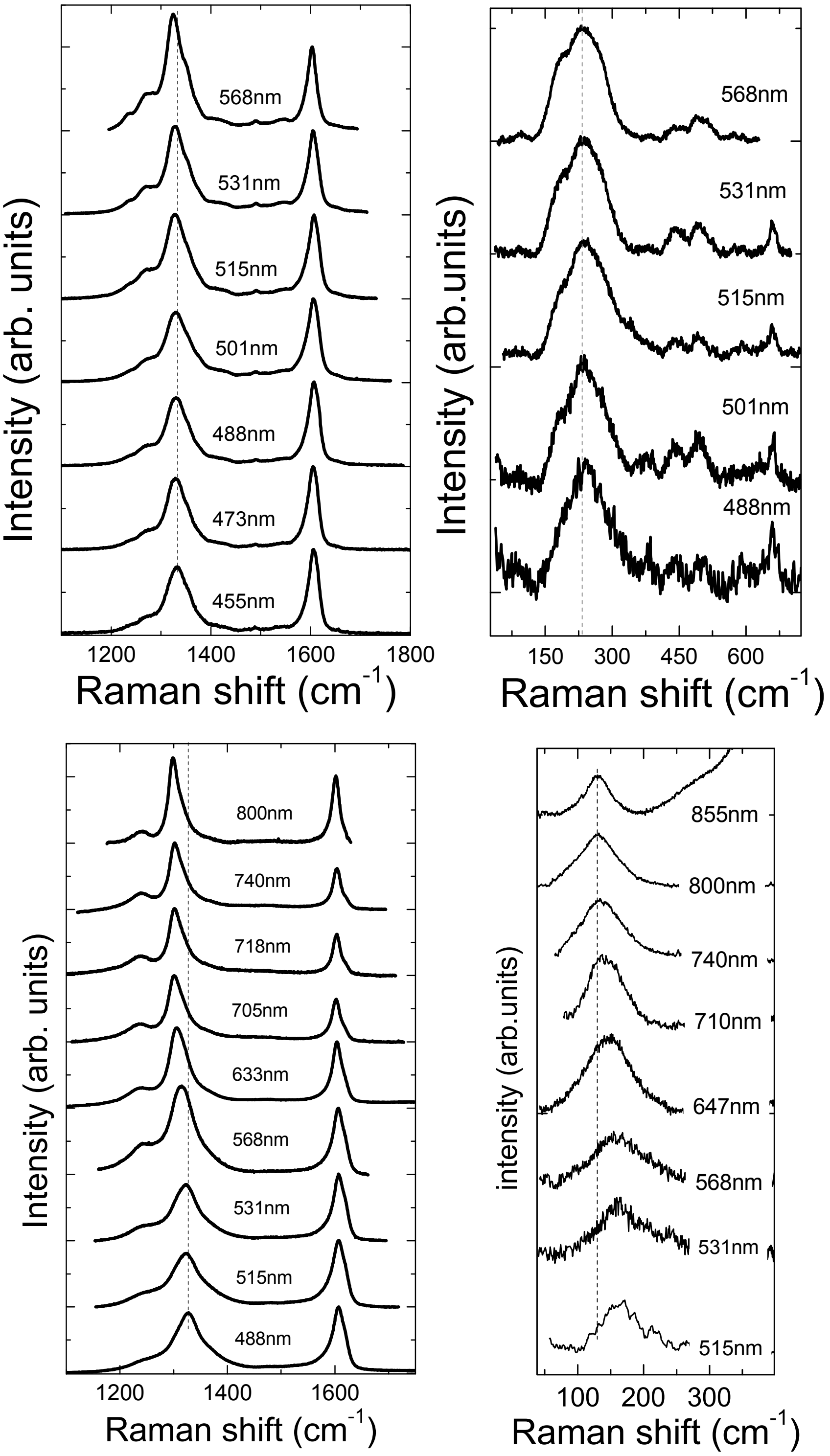

The differences between defective graphene and our GNRs become even more evident when performing multi-wavelength Raman spectroscopy. Figure S3 shows some representative multi-wavelength Raman spectra of 4CNR (top panel) and 8CNR (bottom panel).

The D peak is known to change its position with the excitation energy: the typical D peak dispersion in graphene is ~50 cm^{-1}/eV[2,3]. The D peak of our GNRs is much smaller: this is evident for the 8CNR ribbons (see main text). Figure S4 shows the D peak dispersions measured in all the ribbons investigated in this work: the D peak dispersion changes from 30 to 10 cm^{-1}/eV, depending on the ribbon type. The RLBM shows also considerable dispersion in some of the ribbons (~30 cm^{-1}/eV for 8CNR), as shown in Figure S3.

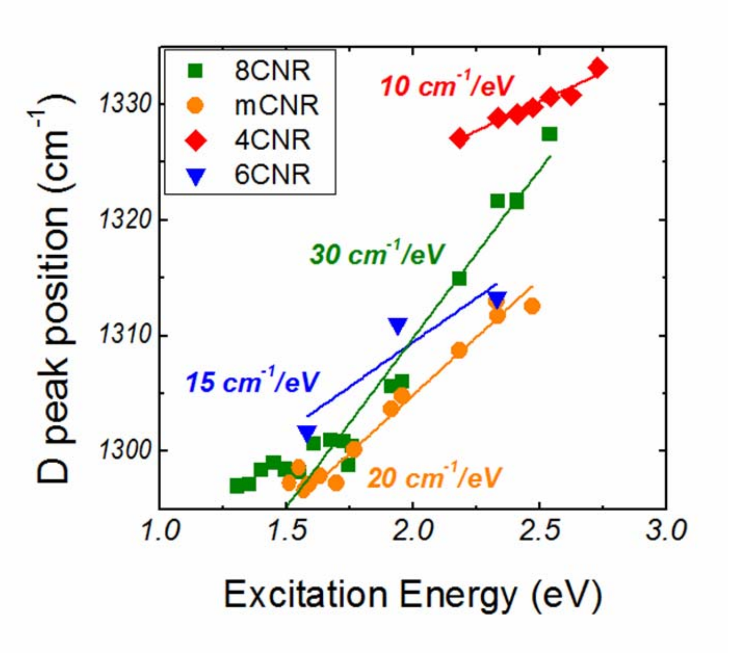

Figure S4 | D peak dispersion for cove-shaped GNRs investigated.

Figure S5 shows a systematic comparison of the D and G peak dispersion of 8CNR with the D and G peak dispersion of defective graphene, with different inter-defect distance (L_D). All the data for defected graphene are taken from Ref.[4].

The effect of an increasing amount of defects on the Raman spectrum of graphene can be described with a phenomenological three-stage model[4,5]. In stage 1) starting from pristine graphene, the Raman spectrum evolves as follows: the D peak appears and the intensity ratio between the D and G peaks [I(D)/I(G)] increases; the D' and D+D' peaks appear; all the peaks broaden and G and D' begin to overlap. In this stage, I(D)/I(G) can be used to estimate the amount of defects[4]. At the end of Stage 1), when the distance between defects L_D ~ 4nm, the G and D' peaks are no more distinguishable and I(D)/I(G) starts decreasing. As the number of defects keeps increasing (hence L_D decreases), the Raman spectrum enters Stage 2), showing a marked decrease in Pos(G); I(D)/I(G) sharply decreases towards zero and second-order peaks are no more well defined. Stage 3) describes amorphous materials with increasing sp^3 content. In this stage the Raman spectrum shows an increase in Pos(G), I(D)/I(G) ratio is close to zero and the G peak becomes dispersive with the excitation energy.

Unlike the case of graphene, where the D peak requires a defect for its activation, in PAHs the vibrations corresponding to the D peak are Raman active and do not require any defect to be seen[6]. The energy dependence of both D and G peak uniquely fingerprints the presence of 1-D GNRs and it is clearly different from the one of defective graphene and PAHs (Figure S5). Note that as representative PAHs we have used $C_{78}H_{26}$, having D_{2h} symmetry (ie elongated geometry, similar to a very short GNRs). All the Raman data related to the $C_{78}H_{26}$ molecule have been taken from Ref.[1]. The Raman spectrum of this molecule is characterized by several D peaks, Figure S5 showing only one of the components. The same applied to the G peak, which has two components in $C_{78}H_{26}$[1].

Note that the G peak also shows a very small dispersion, Figure S5. A closer look at the G peak shows that the peak is also asymmetric and the asymmetry is increasing for increasing laser energy, Figure S6.

Figure S5 | (Left panel) D peak dispersion of 8CNR, defective graphene with different inter-defect distance and $C_{78}H_{26}$. (Right panel) G peak dispersion of 8CNR, defective graphene with different inter-defect distance and $C_{78}H_{26}$.

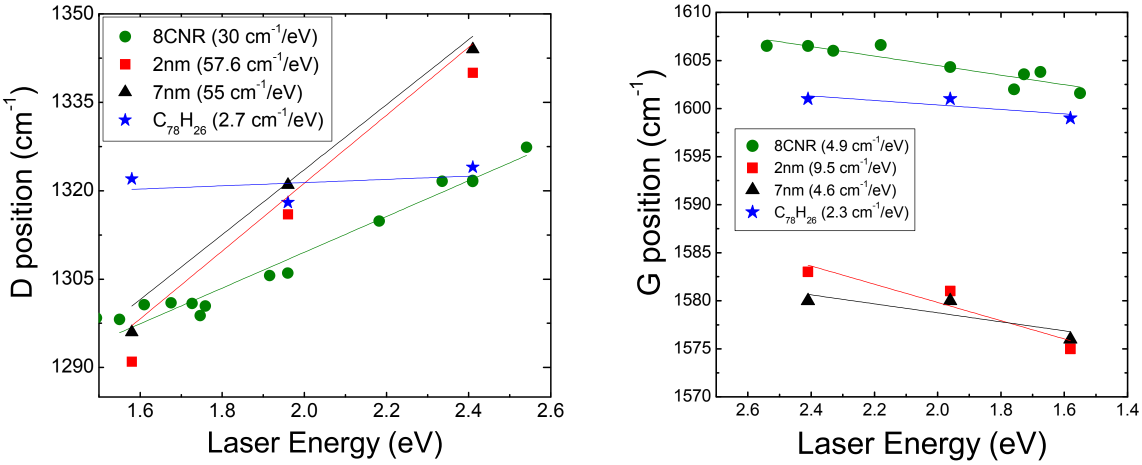

Figure S6 | G peak of 8CNR measured at different excitation wavelengths.

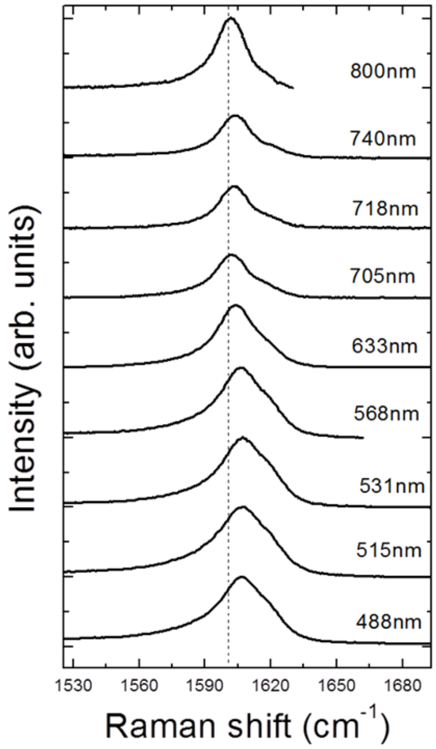

S3. DFPT simulations: width dependence of the RLBM and phonon dispersion of the D peak

Similarly to the case of CNTs[7,8], Pos(RLBM) in armchair and zigzag GNRs is predicted to show an inverse dependence on the GNR width w, which can be formulated as:

$$Pos(RLBM) = \frac{3222\ \text{Å}\ cm^{-1}}{w} \qquad (1)$$

within the zone-folding (ZF) approximation[9]. In the case of cove-shaped graphene GNRs, the width is however not well-defined due to the modulated structure (see Figure S7). The ZF approximation works also for our cove-shaped GNRs, if we define an effective width w_{eff} as the weighted average of the different widths composing the unit cell:

$$w_{eff} = \frac{\sum_{i=1}^{N} w_i a_i}{\sum_{i=1}^{N} a_i}, \qquad (2)$$

where w_i is the width of the i-th component and a_i is its multiplicity (i.e. number of GNR unit cells with the same width, see Figure S7). The comparison of such a ZF approach with DFPT simulations is reported in Figure 3b of the main text, while Figure S7b shows the absolute difference of Pos(RLBM) between DFPT calculations and ZF results, which are obtained by setting the w in Eqn. 1 equal to the minimal (w_{min}), maximal (w_{max}), or effective width (w_{eff}, Eqn. 2) of the GNR.

Figure S8 reports the phonon dispersion for the smaller GNR, i.e. the 4CNR, in the region around the D mode (indicated by a red arrow).

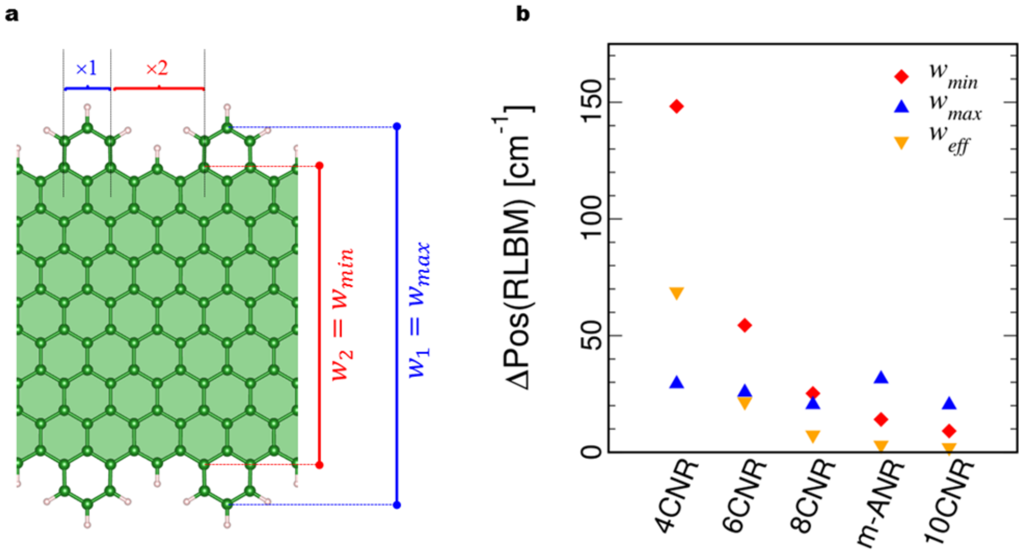

Figure S7 | Defining an effective width for the ZF approximation. a, Ball-and-stick model of the 8CNR, where the width and multiplicity of the different components is highlighted. **b,** Comparison of DFPT and ZF results for Pos(RLBM), as obtained by using the minimal (w_{min}), maximal (w_{max}), or effective width (w_{eff}). ΔPos(RLBM) is the absolute difference between DFPT and ZF Pos(RLBM).

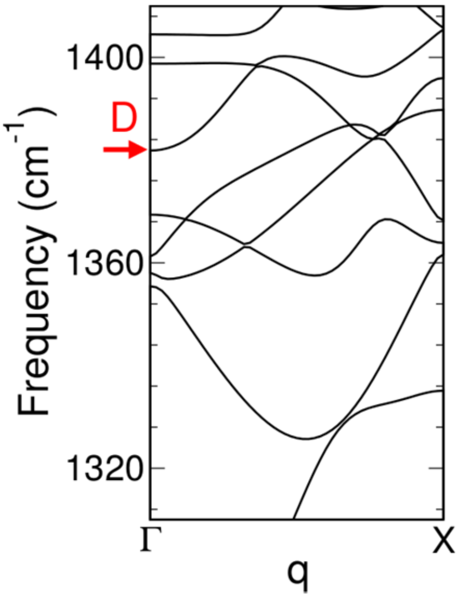

Figure S8 | Phonon dispersion for 4CNR in the D-peak energy region.

References

1. Maghsoumi, A., Brambilla, L., Castiglioni, C., Müllen, K. & Tommasini, M. Overtone and combination features of G and D peaks in resonance Raman spectroscopy of the C 78 H 26 polycyclic aromatic hydrocarbon. *J. Raman Spectrosc.* **46,** 757–764 (2015).

2. Ferrari, A. C. *et al.* Raman Spectrum of Graphene and Graphene Layers. *Phys.~Rev.~Lett.~* **97,** 187401 (2006).

3. Casiraghi, C. *et al.* Raman spectroscopy of graphene edges. *Nano~Lett.~* **9,** 1433–1441 (2009).

4. Cançado, L. G. *et al.* Quantifying defects in graphene via Raman spectroscopy at different excitation energies. *Nano Lett.* **11,** 3190–6 (2011).

5. A.C. Ferrari, J. Robertson, *Resonant Raman spectroscopy of disordered, amorphous, and diamondlike carbon,* Phys. Rev. B **63**, 121405 (2001).

6. Castiglioni, C., Tommasini, M. & Zerbi, G. Raman spectroscopy of polyconjugated molecules and materials: confinement effect in one and two dimensions. *Phil.~Trans.~R.~Soc.~Lond.~A* **362,** 2425–2459 (2004).

7. Saito, R., Dresselhaus, G. & Dresselhaus, M. S. *Physical Properties of Carbon Nanotubes*. (Imperial College Press, London, 1998).

8. Reich, S., Thomsen, C. & Maultzsch, J. *Carbon Nanotubes: Basic Concepts and Physical Properties*. (Wiley-VCH Verlag GmbH, 2004).

9. Gillen, R., Mohr, M. & Maultzsch, J. Symmetry properties of vibrational modes in graphene nanoribbons. *Phys.~Rev.~B* **81,** 205426 (2010).

4.1 BACKGROUND: IR FINGERPRINT OF PAH EDGES

Among the IR modes of a sp^2 carbon system [112, 58, 103], a particular set of them involves the collective wagging of the functionalizating hydrogen atoms: such set of modes is called *out of plane* (OPLA) [28]. The peculiarity of the OPLA modes lies in the fact that their frequencies are strongly correlated to the edge morphology. The four possible edges of a polycyclic aromatic hydrocarbons (PAH) are classified according to the number of hydrogen atoms attached to a single benzene ring (see Fig. 4.1): depending on this number, the OPLA mode will have a different energy in the IR spectrum. As a consequence, one can obtain useful information about the edge morphology of a carbon sp^2 system by investigating the intensity of the peaks localized in the SOLO, DUO, TRIO and QUATRO ranges. This idea was used, for example, by Centrone et al. in Ref. [28] where the relative intensities of the peaks were employed to characterize the distribution of the edge terminations

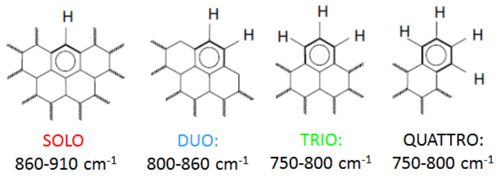

Figure 4.1.: The possible edges of a PAH vs the energy of the IR peak associated to the wagging of H atoms. Image adapted from [28]

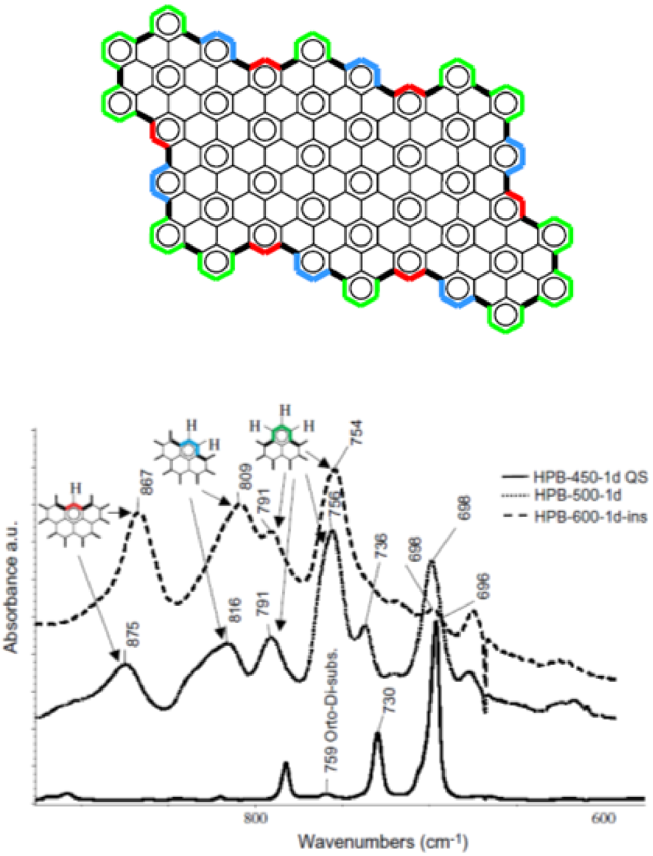

Figure 4.2.: Centrone et al. IR analysis of a PAH: the different edge morphologies give IR peaks, connected to the wagging of H atoms, in different energies ranges.Image taken from [28]

4.2 IR FINGERPRINTS OF SOLUTION PROCESSED FUNCTIONALIZATED GNRS

We adopt the approach described in Ref. [28] to discriminate between different edge functionalizations also in the case of the solution processed GNR described in the previous section. The ball-and-stick models of these different GNR are reported in Fig 4.3 for clarity. According to the nomenclature used for PAH [28], we see (Fig. 4.3) that the configuration of H edge atoms is of SOLO type for the 4CNR and 8CNR samples, while it is of TRIO type for the 6CNR . This is related to the different functionalization with alkyl chains, which are attached to the outer C-rings for 4 and 8 CNR, and to the cove for 6CNR samples. As a consequence, we would expect an intense peak in the SOLO range ($860 - 910$ cm^{-1}) for 4 and 8 CNR while for the 6CNR the most intense peak should be at lower frequencies (TRIO range, $750 - 800$ cm^{-1}). However, the available experimental data (see Fig. 4.7) show several peaks in the $700 - 860$ cm^{-1} range for all the other systems, making the interpretation less straightforward than expected. To gain further insights into this issue, we simulated the IR spectra of these systems from first principles.

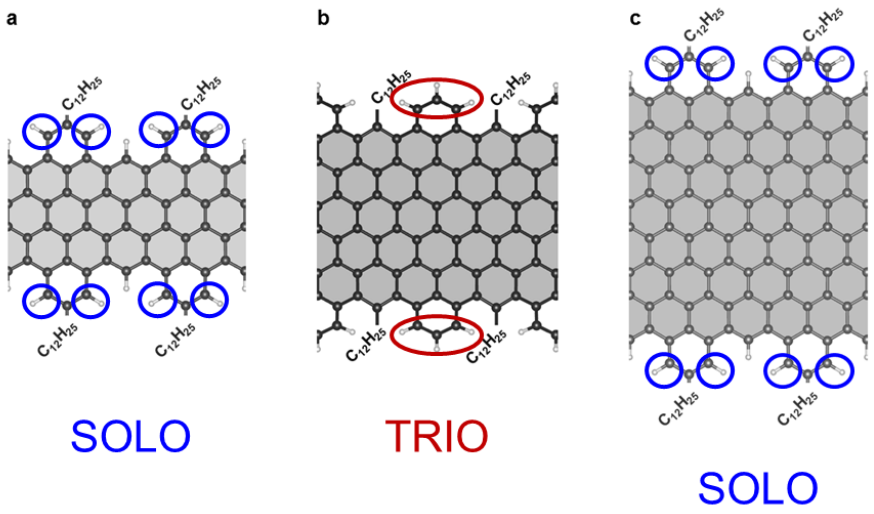

Figure 4.3.: Ball-and-stick representation of the atomic structure of the cove-shaped GNRs investigate here, that is 4CNR (a), 6CNR (b), 8CNR (c). Note the different location of the alkyl side chains

COMPUTATIONAL DETAILS Simulations were performed using a first-principle plane-wave pseudopotential implementation of Density Functional Theory (DFT) and Density Functional Perturbation Theory (DFPT) [10], as available in the Quantum ESPRESSO [50]. The local density approximation for the exchange correlation functional was adopted. Norm conserving pseudopotentials were employed, with a plane-wave cutoff energy of 70 Ry. A vacuum region of 12 Å in the non periodic directions was introduced to prevent interaction between periodic images. The atomic positions were fully relaxed until forces were less than 5×10^{-4} a.u. Phonon frequencies were calculated using a $16 \times 1 \times 1$ k-point grid. As done in our previous paper on Raman, we simulated GNRs with shorter alkyl chains (C_4H_9), with respect to experimental ones ($C_{12}H_{25}$), in order to reduce the computational effort: as shown in Fig. 4.4 this approximation is justified since no change in the major features of the spectrum is observed for alkyl chains longer than C_4H_9.

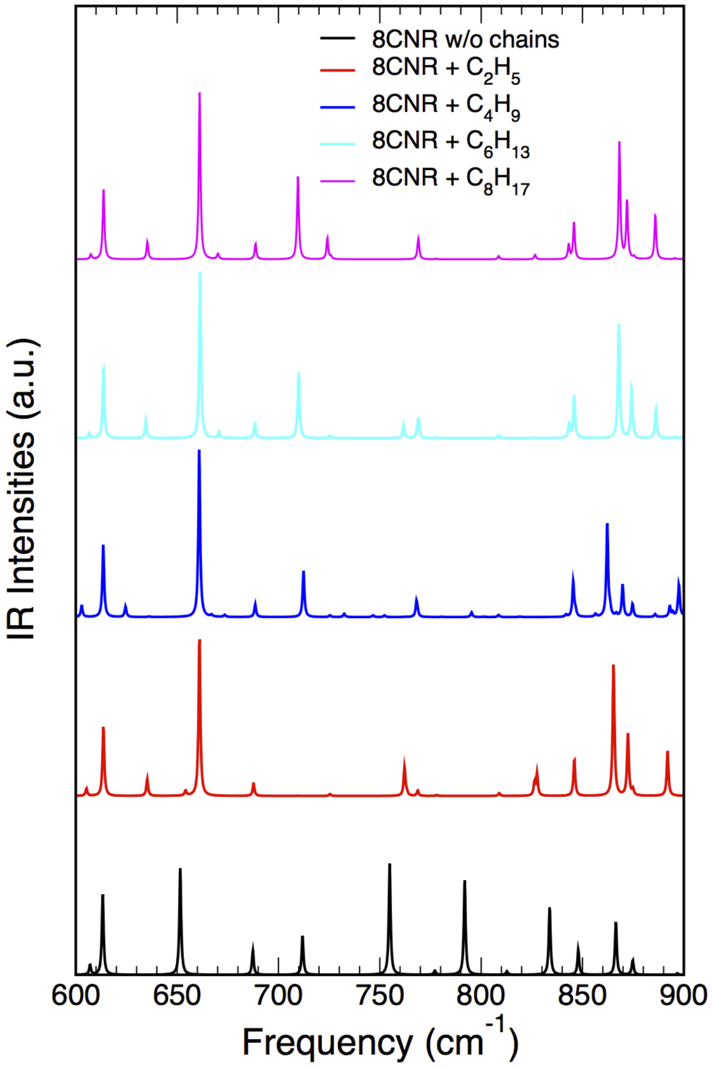

Figure 4.4.: Effects of the length of the alkyl chains on the IR absorption spectrum of 8CNR: starting from the 8CNR+C_4H_9 the major features of the spectrum are converged

RESULTS Fig. 4.5 reports our ab-initio analysis of the IR spectra for the GNR shown in Fig 4.3. Furthermore we also considered the case of the 6CNR+C_4H_9 (edge) to directly compare the two different functionalizations for the same system. We labelled with B the modes in which the GNR backbone is mostly involved, to clearly distinguish them from those involving only the functional atoms or groups. Most of the IR peaks are indeed connected to the displacement of the GNR. However, for each GNR system, there are two peaks connected to the functionalization: the first one is related to the rocking of the alkyl chains, while the second one concerns the wagging of the hydrogen atoms, as expected for the SOLO and TRIO modes. The displacements of these modes are reported in Fig 4.6. Let us first focus on the rocking mode: for the systems in which the alkyl chains are attached in the edge configuration (see Fig. 4.3), this mode is about 710 cm^{-1}, while this mode has a lower frequency (682 cm^{-1}) in the cove configuration. Comparing this prediction with the experimental spectra in Fig. 4.7, it can be seen that, while in the 4CNR(edge) and 8CNR(edge) systems the first most intense peak lies at $718 - 720$ cm^{-1}, in the case of the 6CNR(cove) the first peak has a lower energy (700 cm^{-1}), in agreement with our predictions. As a consequence we can attribute this experimental peak to the rocking of the alkyl chains. Now, we can move to the analysis of the SOLO and TRIO modes: as it can be seen from our simulated spectra, the wagging of the hydrogen atoms has a higher energy in the case of edge configuration ($860 - 862$ cm^{-1}), while in the cove configuration the energy of this mode is redshifted to 762 cm^{-1}, in agreement with the expected values for SOLO and TRIO configuration. However, in the case of 6CNR(cove), a peak connected to a backbone mode is present at 863 cm^{-1}, i.e at the same frequency of the SOLO mode. At the same time, low intensity backbone modes are present for the edge configuration at about $750 - 700$ cm^{-1}. All this makes the characterization rather complicated without knowing the displacements. The comparison with experiments indeed indicates a higher intensity for the TRIO peak in cove configuration for the 6CNR, while the situation is reversed (higher intensity for the SOLO peak) in the 4CNR. In the case of the 8CNR, the intensities are comparable, leaving the attribution less certain.

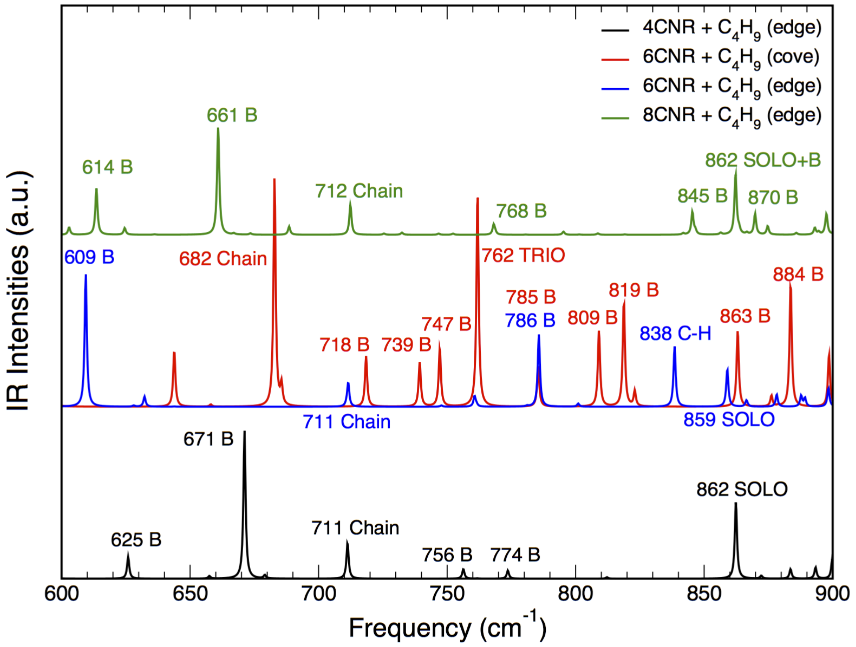

Figure 4.5.: The infrared intensities of the 4CNR(edge), 6CNR(edge), 6CNR(cove) and 8CNR(edge) systems, as calculated from ab-initio principles: the B labels stand for a mode which involves mainly the backbone of the nanoribbon, the Chain, SOLO and TRIO labels indicate the modes shown in Fig 4.6, while the C-H refers to a mode connected to an OPLA mode but with a slightly lower energy with respect to the range reported in the literature (see Fig. 4.1)

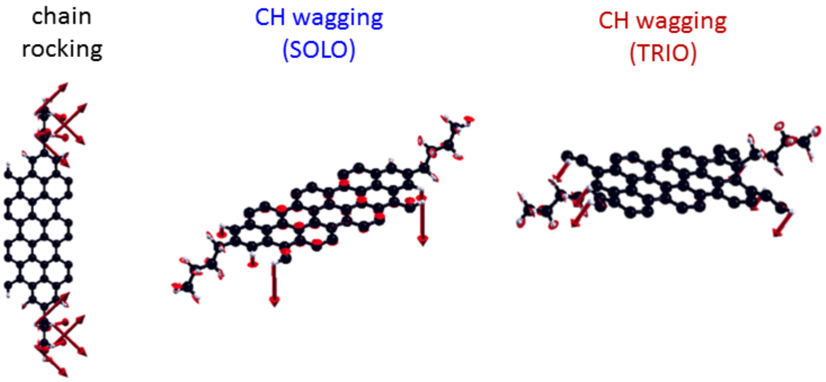

Figure 4.6.: The displacements of the chain, SOLO and TRIO modes. The images were obtained through the visualization software XCrySDen [68]

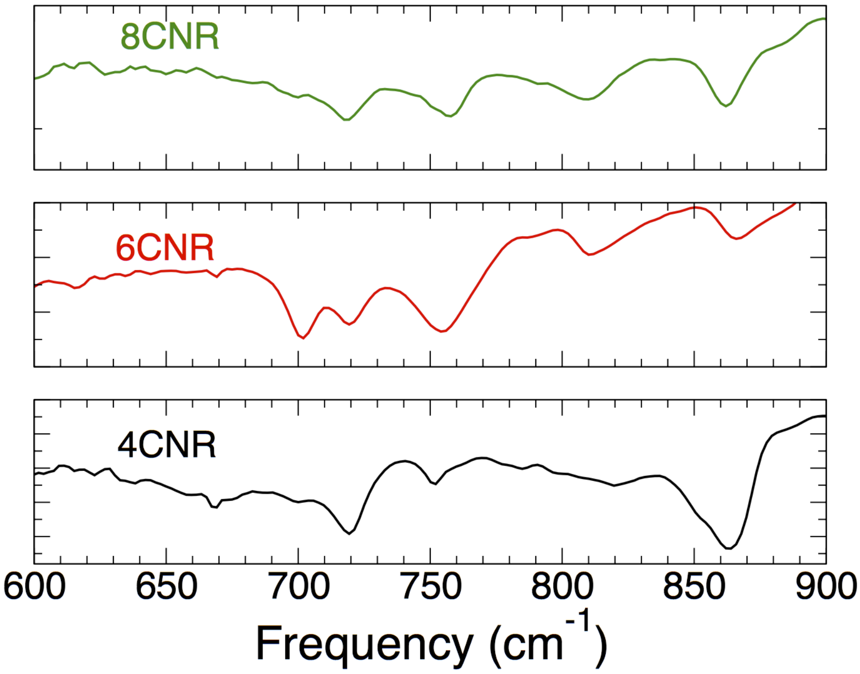

Figure 4.7.: Experimental data on the IR absorption spectra of the 4CNR(edge), 6CNR(cove) and 8CNR(edge) systems. Images are from a private communication: Narita et al. (2015)

5 OPTICAL PROPERTIES OF BILAYER GRAPHENE NANOFLAKES

As introduced in Chapter 1, the electronic and optical properties of GNRs are highly sensitive to the details of the atomic structure: the peculiar edge shape (armchair vs. zigzag) implies different electronic and magnetic properties, and even slight ribbon width variations induce striking variation in the electronic and optical properties [39, 109]. Moreover, the GNR properties can be further modulated by means of organic edge functionalization [34, 32, 33, 31]. Most previous studies were limited to isolated graphene nanostructures (see Chapter 1). However, it is well-known that π-π interaction is often very relevant. For instance it is a driving mechanism to spontaneous aggregation for such structures. We here focus on the effect of π-π coupling on the optical properties of finite graphene nanoribbons. Our study comprises many different bilayered graphene flakes: we study both homogeneous stacking (different geometries for the staking of two identical nanostructures) and heterogeneous stacking (stacking of two different nanostructures). Our investigation confirms that π-π coupling provides an efficient strategy to shape the optical properties of such low dimensional nanostructures.

THE JOURNAL OF PHYSICAL CHEMISTRY C
Article
pubs.acs.org/JPCC

Optical Properties of Bilayer Graphene Nanoflakes

Marzio De Corato,[*,†,‡] Caterina Cocchi,[‡,∥] Deborah Prezzi,[‡] Marilia J. Caldas,[§] Elisa Molinari,[†,‡] and Alice Ruini[*,†,‡]

[†]Dipartimento di Scienze Fisiche, Informatiche, Matematiche, Università di Modena e Reggio Emilia, I-41125 Modena, Italy
[‡]Centro S3, CNR-Istituto Nanoscienze, I-41125 Modena, Italy
[§]Instituto de Física, Universidade de São Paulo, 05508-900 São Paulo, SP, Brazil

S *Supporting Information*

ABSTRACT: The optical properties of coupled graphene nanoflakes are investigated theoretically within the framework of Hartree−Fock based semiempirical methods, with the aim of unraveling the role of $\pi-\pi$ interactions. Two different types of π-stacking are considered, obtained either by coupling two identical flakes with different relative displacement or by coupling flakes having different width or edge functionalization, i.e., with different electronic gap or ionization potential. Our results indicate that a systematic red shift and broadening of lowest excitations occur: an overall widening of the optical absorption range can therefore be expected in an ensemble of flakes. However, the coupling prevents a strong enhancement of the absorption intensity. In the case of a heterogeneous ensemble of flakes, the possibility of introducing low-energy excitations with considerable charge transfer character is also demonstrated by properly exploiting the chemical edge functionalization.

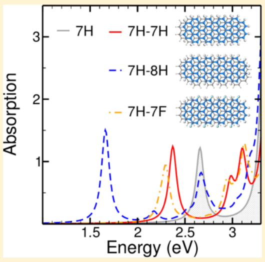

■ INTRODUCTION

Strong noncovalent interactions between π-conjugated systems are strategic in biochemistry, supramolecular chemistry, and materials science. In fact, they typically show up spontaneously and control such diverse phenomena as the vertical base−base interactions which stabilize the double helical structure of DNA,[1] the tertiary structures of proteins,[2,3] the aggregation of polycyclic aromatic hydrocarbons (PAHs),[4,5] and the aromatic molecules in organic crystals[6,7] and in discotic liquid crystals.[8,9] Because of their intriguing photoluminescence phenomena,[10,11] supramolecular π-stacked structures have particular technological relevance for optoelectronic applications.

More recently, the relevance of π-stacking emerged also in graphene[12−15] and its nanostructures,[16−18] such as graphene nanoribbons. The electronic and optical properties of isolated ribbons have been shown to be highly sensitive to the details of the atomic structure: the specific edge shape (armchair vs zigzag) implies different electronic and magnetic properties,[19−21] and even slight ribbon width variations induce striking modifications in the electronic and optical properties.[22−24] In addition, edge functionalization can also be exploited to modulate their properties even further.[25−29] While most previous studies were limited to isolated graphene nanostructures, the effect of $\pi-\pi$ interactions should be considered in view of the fact that they spontaneously occur (e.g., when graphene nanostructures are obtained in solution[30] or by unrolling multiwall carbon nanotubes[16,17]) and with the idea to intentionally exploit the layer stacking as an additional parameter to tune their electronic[31−36] and optical properties.[36,37]

We here focus on the effect of $\pi-\pi$ coupling on the optical properties of finite ribbons, i.e., elongated graphene nanoflakes (GNFs). Our study comprises several bilayer graphene nanoflakes (BGNFs), including both homogeneous stacking (different geometries for the π-stacking between two identical nanostructures) and heterogeneous stacking (π-stacking between two different nanostructures, namely, with different width or with different edge functionalization). For all considered coupled systems, we find that the low-energy optical excitations are red-shifted and broadened with respect to their isolated counterparts. A proper choice of edge functionalization is also demonstrated to give rise to charge-transfer excitations. Our whole analysis confirms that the $\pi-\pi$ coupling impacts the optical properties of GNFs, and it can also provide an efficient strategy to shape the optical properties of such low-dimensional nanostructures.

■ COMPUTATIONAL DETAILS

We investigate a number of bilayer structures, composed of elongated GNFs with armchair edges along the length; the flake ends are shaped to minimize the zigzag region and thus to avoid spin-related effects.[38,39] The bilayer systems are built by stacking two identical flakes (homogeneous stacking), as shown in Figure 1, or two flakes differing from each other by either width or edge functionalization (heterogeneous stacking); see Figure 3. In the following, single and bilayer systems are labeled according to both their width parameter N,[40] which indicates the number of dimers along the zigzag direction (y axis in Figure 1), and their edge terminations. According to this notation, we consider the homogeneously stacked 7H-7H

Received: April 30, 2014
Revised: August 27, 2014
Published: September 9, 2014

dx.doi.org/10.1021/jp504222m | *J. Phys. Chem. C* 2014, 118, 23219−23225

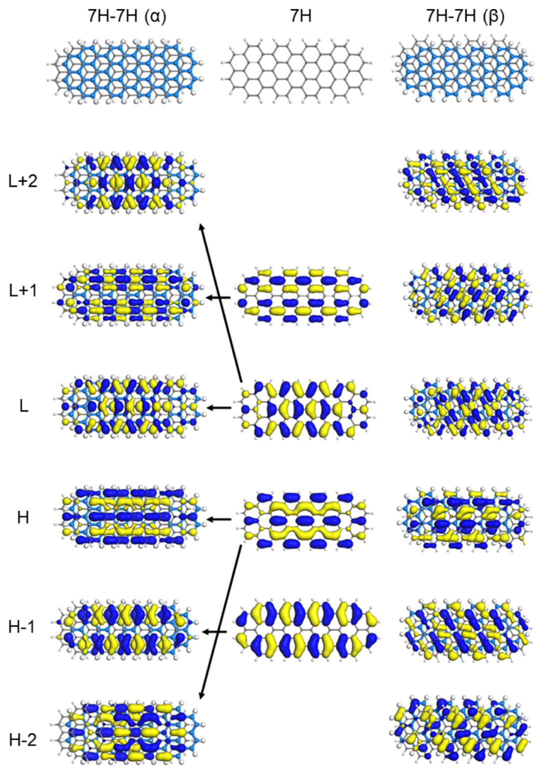

Figure 1. Ball-and-stick models of the 7H GNF and the 7H-7H BGNFs (upper panel), with their related frontier orbitals. The bilayer structures are obtained by combining two N = 7 GNFs in Bernal stacking with different displacements, i.e., α (left panel) and β (right panel); see text. C atoms of the top (bottom) layer are in gray (blue); H atoms are in white. The frontier orbitals are also shown for the single GNF (central panel): for the α stacking the derivation of the BGNF orbitals from the ones belonging to the individual GNF is evident and highlighted with arrows.

BGNF, which is obtained by coupling two hydrogen terminated GNFs with N = 7, hereafter labeled 7H; the heterogeneously stacked 7H-8H and 7H-7F BGNFs, which are obtained by coupling the 7H GNF with the hydrogenated N = 8 one (8H) and with the edge-fluorinated N = 7 one (7F).[41]

The optical properties are computed within the framework of the Hartree−Fock based semiempirical ZINDO method,[42] which is well-tested and reliable for the study of C-conjugated low-dimensional systems[43−48] also in nonbonded $\pi-\pi$ intermolecular conformations.[49] The AM1 model,[50] usually adopted for structural optimization of covalently bonded molecular systems, is however not designed to capture the effect of intermolecular (van der Waals) interactions. Hence, we performed geometry optimizations by means of first-principles density-functional theory (DFT) calculations by using plane-waves basis set, ultrasoft pseudopotentials, the Perdew−Burke−Ernzerhof exchange correlation functional,[51] and van der Waals interactions through the semiempirical DFT-D2 approach by Grimme,[52] as implemented in the Quantum ESPRESSO package.[53] This approach has proven successful for the description of several C-based materials[54] and is employed here for both single and bilayer systems.[55] The plane-wave kinetic-energy cutoff was set to 30 Ry for the wave functions and 240 Ry for the charge density for hydrogen-terminated GNFs and increased to 48 and 384 Ry, respectively, for systems including F. Structures were relaxed using a threshold for the forces on atoms of 10^{-4} Ry/au.

Starting from the DFT-D2 geometries, optical spectra are evaluated by employing the semiempirical ZINDO/S approach with single excitation configuration interaction (CIS).[56] Our convergence tests over the number of occupied and virtual molecular orbitals (MOs) indicate that a CI energy window of at least 4.5 eV below the HOMO and 3.5 eV above the LUMO is required for a reliable characterization of the low-energy optical excitations.

To further analyze the nature of the main optical excitations, we compute the spatial distribution of their electron (e) and hole (h) components, as described in ref 57. Starting from the MOs in the standard LCAO expansion[58]

$$\phi_i(\mathbf{r}) = \sum_j a_{ji}\chi_j(\mathbf{r}) \tag{1}$$

where $\chi_j(\mathbf{r})$ are Slater-type orbital basis functions and a_{ji} are the projection coefficients, the probability density of h and e for the Ith excited state can be expressed as

$$\rho_{\mathrm{h}}^{I}(\mathbf{r}) = \sum_{\alpha\beta} |c_{\alpha\beta}^{I}\cdot\phi_\alpha(\mathbf{r})|^2 \tag{2}$$

$$\rho_{\mathrm{e}}^{I}(\mathbf{r}) = \sum_{\alpha\beta} |c_{\alpha\beta}^{I}\cdot\phi_\beta(\mathbf{r})|^2 \tag{3}$$

Here $c_{\alpha\beta}^{I}$ are CI coefficients weighting the contribution to the Ith excitation of each transition $\alpha \rightarrow \beta$ from occupied (ϕ_α) to virtual (ϕ_β) MOs. The spatial localization of the excitation can then be quantified by integrating $\rho_{\mathrm{e/h}}^{I}(\mathbf{r})$ over a selected region of the total system.[57]

■ RESULTS AND DISCUSSION

Homogeneous Stacking. We first consider a system composed of two identical hydrogenated N = 7 (7H) GNFs. As shown in Figure 1, two different arrangements of the 7H flakes can be identified as compatible with the Bernal stacking typical of graphite, which we label as 7H-7H(α) and 7H-7H(β), following the notation of refs 36 and 59. In the α stacking (Figure 1, upper left panel), one flake is shifted with respect to the other by a single C−C bond length along the x direction; in the β stacking the same displacement is applied along a direction forming an angle of $\pi/3$ with the x axis (Figure 1, upper right panel). The interlayer distance is almost identical for the α and β arrangements (3.310 and 3.312 Å, as evaluated at the flake center), and the α configuration is slightly more stable than the β one (by 0.01 eV). The different packing conformations result mostly in different alignments of the flake edges (see Figure 1), which give rise to different combinations for the molecular orbitals of the BGNFs.

The absorption spectra of the 7H-7H BGNFs for both α and β stackings are shown in Figure 2a, as compared to the spectrum of the single 7H GNF. The interlayer coupling clearly produces a red shift of the first absorption peak of about 0.30 eV for the α stacking and 0.15 eV for the β stacking. Analyzing the one-electron level structure (Figure 1), we see that in both cases the HOMO and LUMO of the bilayer are related to a level splitting that is connected, respectively, to the HOMO and LUMO of the individual flakes. However, while the α stacking preserves the yz reflection symmetry, this is not the case for the β stacking. The different symmetry results in different energy splittings for α and β, similar to the case of

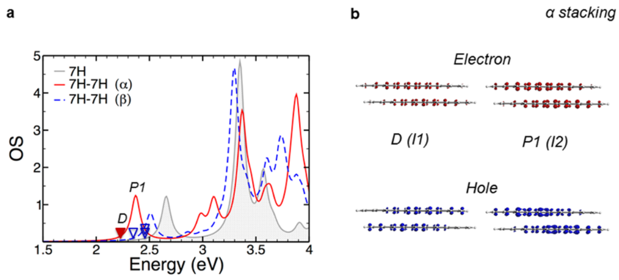

Figure 2. Optical properties of the 7H-7H BGNFs. (a) Absorption spectra for the α (solid red) and β (dashed blue) stacking configurations, compared to the spectrum of the isolated $N = 7$ GNF (gray area). Triangles indicate optically inactive states. For the spectra we use a Lorentzian broadening of 100 meV. (b) Probability densities of the electrons (red) and holes (blue) for the first dark (D) and the first optically active (P1) excitation of the 7H-7H (α) BGNF (D and P1 are also indicated as I1 and I2, according to the notation in Table 1).

infinite bilayer nanoribbons of the $3p + 1$ family.[36] The first optically active excitation (P1) for both α and β configurations is mainly composed of the HOMO → LUMO transition (H → L; see Table 1) and is thus directly derived from that of the single 7H flake. As the HOMO and LUMO orbitals of the BGNFs are homogeneously distributed over the single flakes (see Supporting Information and Figure 1, left panel), the e and h probability densities for this excitation are equally distributed over the two flakes (see Figure 2 for the α stacking).

Table 1. Low Energy Optical Excitations (I) of the 7H-7H (α) BGNF[a]

I	E	OS	$c_{\alpha\beta}^2$		$\mu_\parallel$	$\mu_\perp$
1	2.28	0.00	(0.52)	H − 1 → L	0.00	0.00
			(0.25)	H → L+1		
2	2.37	1.22	(0.83)	H → L	11.46	1.95
3	2.44	0.00	(0.14)	H − 4 → L	0.40	0.01
			(0.22)	H − 1 → L + 2		
			(0.33)	H → L + 3		
4	2.54	0.00	(0.35)	H − 2 → L	0.00	0.00
			(0.52)	H → L + 2		
20	3.37	2.97	(0.51)	H − 2 → L + 2	15.15	1.71
			(0.23)	H − 1 → L + 1		

[a] Energy (E, in eV), oscillator strength (OS), squared CI coefficients ($c_{\alpha\beta}^2$) of relevant transitions ($c_{\alpha\beta}^2 \geq 0.1$), and the projections of the transition dipole moment (μ in D) in the GNF plane (xy plane, $\mu_\parallel$) and perpendicular to it (z direction, $\mu_\perp$).

For both configurations, dark excitations are detected below the first optically active peak, as indicated by triangles in Figure 2a. Again, as for the isolated 7H GNF, they are mainly composed of H − 1 → L and H → L + 1 transitions (see Table 1 for the α stacking and Table S1 in Supporting Information for the β stacking). Indeed, the HOMO − 1 and LUMO + 1 states of the BGNFs are directly related to the splitting of the HOMO − 1 and LUMO + 1 levels of the single flake (see Figure 1). However, while for the α stacking we see only one dark state in this energy region (red triangles in Figure 2), in the case of β stacking three dark states (blue empty triangles) are found, as a consequence of the lower symmetry and different level splittings.

We thus see that a very small difference in the stacking configuration can produce a significant difference in the optical properties. Going further in this investigation, we found that, preserving the symmetry of the α stacking but imparting larger shifts between the GNFs in the x direction, the interlayer coupling weakens and finally vanishes because of insufficient π-overlap area (see Figure S2). In other words, the π-stacking in a realistic ensemble of identical flakes is expected to produce a significant broadening of the low-energy absorption peak, which can be about 0.4 eV for such subnanometer narrow flakes (as evaluated from the energy spread of the lowest peaks in the absorption spectra of differently coupled 7H flakes; see Figure 2).

On the other hand, even if one could expect a strong enhancement of the absorption intensity as compared to the single flakes, this is not the case because of the specific character of the transition dipole moment $\vec{\mu}$ in these GNFs: while $\vec{\mu}$ gains a small intensity in the direction normal to the flakes in the bilayer structures, there is a "ring-by-ring" cancellation in the parallel direction that compensates for the presence of two flakes.

Heterogeneous Stacking. After the homogeneous stacking of identical hydrogenated flakes, we now analyze the coupling of two hydrogenated flakes of different width, namely, $N = 7$ and $N = 8$, resulting in the 7H-8H BGNF displayed in Figure 3a. In Figure 3b we show the AM1 electron affinities and ionization potentials calculated for the isolated flakes. The smaller gap associated with the 8H flake, as expected from the $3p + m$ modulated electronic properties of GNFs,[57,60] suggests that the low-energy optical activity of the bilayer structure will be dominated by the excitations of the 8H flake, as we will confirm in the following.

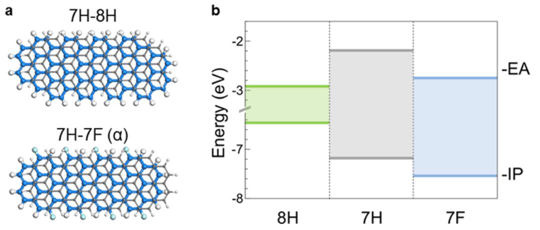

Figure 3. (a) Ball-and-stick model of the 7H-8H and 7H-7F BGNFs. C atoms of the 7H GNF are in gray, and C atoms of the 8H and 7F GNFs are in blue. H atoms are in white and F atoms in light blue. (b) Scheme for the electron affinity (EA) and ionization potential (IP) of the single GNFs considered here, calculated using the AM1 method (see text).

The frontier orbitals of the 7H-8H BGNF (see Figure S1, central panel) are consistent with the level alignment displayed in Figure 3b: we find that the HOMO and LUMO states are mainly localized on the 8H flake, while HOMO − 1 and LUMO + 1 are more localized on the 7H flake. The optical spectrum of the 7H-8H BGNF, shown in Figure 4a, reflects this spatial separation of the frontier orbitals: at first sight, it indeed looks like a simple superposition of the spectra of the individual 7H and 8H GNFs. In fact, the first active excitation P1 derives from the first excited state of the 8H flake, since it is mainly composed of the H → L transition and therefore prevalently localized on the 8H flake, as also shown by the corresponding e/h densities in Figure 4b. Furthermore, the second most prominent peak P3, mainly involving the H − 1 → L + 1 transition, is accordingly more localized on the 7H GNF, thus

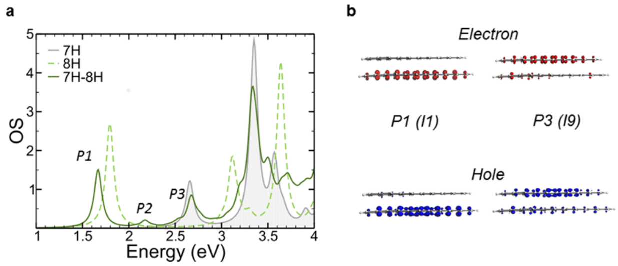

Figure 4. (a) UV−vis spectrum of the 7H-8H BGNF (solid dark green) compared to the spectra of the isolated 7H (gray area) and 8H GNFs (dashed light green). The spectra are obtained by using a Lorentzian broadening of 100 meV. (b) Electron (red) and hole (blue) probability densities for the two main low-energy peaks P1 and P3, indicated in (a) and labeled as *I*1 and *I*9 in Table 2.

retaining the character of the first peak of the 7H GNF, as shown by the e/h densities in Figure 4b. Nonetheless, some subtle features can be directly related to the $\pi-\pi$ coupling between the two flakes, such as the lowering of the oscillator strengths (dipole effect), the slight energy shifts of the main peaks (interaction splitting), and the appearance of other low-energy excitations, such as the new peak P2 at intermediate energy in Figure 4 (corresponding to the *I*3 excitation in Table 2), for which the e/h density is in fact almost equally distributed over the two flakes, as shown in Figure S3. Combining the results of homogeneous and heterogeneous stacking of hydrogenated flakes, we confirm the conclusion that in a more disordered medium, the optical absorption range is expected to be expanded by over 1 eV.

Table 2. Low Energy Optical Excitations (*I*) of the 7H-8H BGNF[a]

I	E	OS	$c_{\alpha\beta}{}^2$		$\mu_{\parallel}$	$\mu_{\perp}$
1	1.66	1.49	(0.89)	H → L	15.36	0.92
2	2.06	0.02	(0.20)	H − 2 → L	1.55	0.06
			(0.31)	H − 1 → L		
			(0.11)	H → L + 1		
			(0.10)	H → L + 3		
3	2.17	0.17	(0.11)	H − 2 → L	4.16	1.74
			(0.45)	H − 1 → L		
			(0.32)	H → L + 1		
9	2.66	0.64	(0.44)	H − 1 → L + 1	7.96	0.30
			(0.12)	H → L + 2		
28	3.32	2.18	(0.10)	H − 2 → L + 1	13.12	0.90
			(0.10)	H − 1 → L + 3		

[a] Energy (E, in eV), oscillator strength (OS), squared CI coefficients ($c_{\alpha\beta}{}^2$) of relevant transitions ($c_{\alpha\beta}{}^2 \geq 0.1$), and the projections of the transition dipole moment (μ, in D) in the GNF plane (xy plane, $\mu_{\parallel}$) and perpendicular to it (z direction, $\mu_{\perp}$).

We next consider the case of a heterogeneous bilayer structure obtained by means of different edge functionalization of the components, namely, the 7H-7F BGNF. Here we focus only on the α configuration, since we find that the differences between α and β alignment are very similar to those discussed for the fully hydrogenated case. As found for single fluorinated GNFs,[60] distortion effects appear also in the bilayer structure: they are mainly localized at the fluorinated edges and are even reduced compared to the isolated system, stating the relevance of intermolecular interactions.

From the scheme of the electron affinity and ionization potential of the individual flakes in Figure 3b, one could expect a corresponding sizable reduction of the optical gap in the BGNF with respect to the single flakes. Indeed, the energies of the first excited states (dark and active, D and P1, respectively) are downshifted by about 0.3 eV with respect to the 7H GNF (see Figure 5a). However, these excitation energies are almost unchanged if compared to the homogeneous 7H-7H(α) stacking (Table 3 and Table 1). This is also the case for the β stacking, as detailed in the Supporting Information. Apparently, the interaction splitting leading to the gap closure in the fully hydrogenated BGNF equals the level alignment effect, which should dominate in the case of the heterogeneous 7H-7F stacking. Analyzing the localization of the frontier orbitals (see Figure S1, right panel), we find that although the LUMO and the LUMO + 1 are mainly localized on the 7F flake, the HOMO and the HOMO − 1 spread over both flakes (the latter to a smaller extent), indicating a sizable rehybridization of the states. This means that the reduction of the optical gap in the 7H-7F case is not only due to the type II level alignment but also due to interaction splitting effects. Furthermore, we can analyze the charge-transfer character of the lowest energy excitations. To this end, we compute the electron spatial localization of the Ith excitation L_e^I, integrating ρ_e^I over a box containing each of the flakes composing the bilayer structure, and analogously for the hole spatial localization L_h^I (see Table 3). We quantify the charge-transfer character of the excitation by computing the difference between electron and hole localization on the same flake. This analysis clearly highlights the difference between the 7H-7H and the 7H-7F systems: in the latter case the hole is mostly localized in the hydrogenated and the electron in the fluorinated flake for the lowest-energy excitations, which present a considerable charge transfer character (see Table 3 and Figure 5b). These results imply that in the case of a mixed ensemble of π-stacked flakes with different width and edge termination, the red shift and widening of the optical absorption range will be accompanied by additional charge transfer effects (similar effects were suggested for different π-coupled systems, e.g., like nanopeapods[61]).

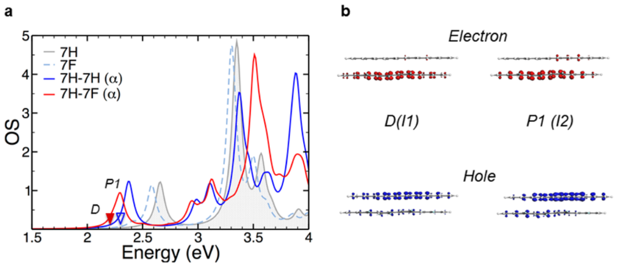

Figure 5. (a) UV−vis spectrum of the 7H-7F BGNF in α alignment (solid red) compared to the spectra of the isolated 7H (gray area) and 7F (dashed light blue) GNFs and of the 7H-7H BGNF (solid blue). For the spectra we use a Lorentzian broadening of 100 meV. The triangles indicate the position of dark states. (b) Electron (red) and hole (blue) probability densities of the first two excitations D and P1 (labeled as *I*1 and *I*2 in Table 3 for the 7H-7F(α) BGNF).

CONCLUSIONS

We studied the effect of π-stacking on the optical properties of elongated graphene nanoflakes with armchair edges. Our study

Table 3. Low Energy Optical Excitations (I) of the 7H-7F (α) BGNF[a]

I	E	OS	$c_{\alpha\beta}^2$		$\mu_{\parallel}$	$\mu_{\perp}$	L_e^{7F}	L_h^{7F}	CT
1	2.24	0.17	(0.29)	$H-1 \rightarrow L$	4.39	0.74	0.78	0.36	0.42
			(0.14)	$H \rightarrow L$					
			(0.27)	$H \rightarrow L+1$					
2	2.30	0.85	(0.71)	$H \rightarrow L$	9.65	2.07	0.75	0.35	0.40
3	2.41	0.00	(0.20)	$H-1 \rightarrow L+2$	0.80	0.14	0.50	0.38	0.12
			(0.11)	$H \rightarrow L+3$					
			(0.19)	$H \rightarrow L+4$					
4	2.50	0.05	(0.29)	$H-2 \rightarrow L$	2.37	0.43	0.45	0.40	0.05
			(0.51)	$H \rightarrow L+2$					
5	2.61	0.01	(0.10)	$H-2 \rightarrow L+1$	1.26	0.00	0.74	0.38	0.36
			(0.20)	$H-1 \rightarrow L$					
			(0.23)	$H \rightarrow L+1$					
27	3.51	3.50	(0.25)	$H-4 \rightarrow L+1$	16.20	0.43	0.60	0.44	0.16
			(0.11)	H-1→L+4					

[a] Energy (E, in eV), oscillator strength (OS), squared CI coefficients ($c_{\alpha\beta}^2$) of relevant transitions ($c_{\alpha\beta}^2 \geq 0.1$), and the projections of the transition dipole moment (μ, in D) in the GNF plane (xy plane, $\mu_{\parallel}$) and perpendicular to it (z direction, $\mu_{\perp}$). Electron and hole localization on the 7F GNF ($L_{e/h}^{7F}$) and charge transfer character (CT); see text.

covered two different types of stacking, namely, the coupling between identical flakes with different relative displacement (homogeneous stacking) and the coupling between different flakes, carrying different electronic properties in terms of electronic gap or ionization potential (heterogeneous stacking). Our findings indicate that in a disordered ensemble of interacting graphene nanoflakes, with different width and edge termination, a significant increase of the optical absorpion range is to be expected. On the other hand, our analysis of the optical excitations and the transition dipole moments allows us to clarify that one should not expect a considerable enhancement of the absorption intensity. Instead, charge transfer excitonic phenomena relevant in optoelectronic applications can be designed by appropriately choosing the chemical functionalization and the layering procedure.

■ ASSOCIATED CONTENT

Ⓢ Supporting Information

Frontier orbitals for both the homogeneous and the heterogeneous BGNFs that are investigated in this paper; the optical absorption results for additional biflake structures, which are obtained by stacking two 7H flakes wih different relative shifts along their main axis; the details of the UV−vis spectra that are not provided in the main text. This material is available free of charge via the Internet at http://pubs.acs.org.

■ AUTHOR INFORMATION

Corresponding Authors

*M.D.C.: e-mail, marzio.decorato@unimore.it.
*A.R.: e-mail, alice.ruini@unimore.it.

Present Address

‖C.C.: Humboldt-Universität zu Berlin, Institut für Physik und IRIS Adlershof, Zum GrossenWindkanal 6, 12489 Berlin, Germany. E-mail: caterina.cocchi@physik.hu-berlin.de.

Notes

The authors declare no competing financial interest.

■ ACKNOWLEDGMENTS

Part of this research was supported by the Italian Ministry of Research through the National Projects PRIN-GRAF (Grant 20105ZZTSE), FIRB-FLASHit (Grant RBFR12SWOJ), and the Program "Progetto Premiale 2012", Project ABNANOTECH; the Italian Ministry of Foreign Affairs through Grant US14GR12; and the Fondazione Cassa di Risparmio di Modena through the "COLDandFEW" project. M.J.C. acknowledges support from FAPESP and CNPq (Brazil). The authors acknowledge CINECA for computational support.

■ REFERENCES

(1) Smungen, W. *Principles of Nucleic Acid Structure*; Springer-Verlag: New York, 1984; pp 132−140.

(2) Burley, S. K.; Petsko, G. A. Weakly Polar Interactions in Proteins. *Adv. Protein Chem.* **1988**, *39*, 125−192 and references therein.

(3) Meyer, E. A.; Castellano, R. K.; Diederich, F. Interactions with Aromatic Rings in Chemical and Biological Recognition. *Angew. Chem., Int. Ed.* **2003**, *42*, 1210−1250.

(4) Desiraju, G. R.; Gavezzotti, A. From Molecular to Crystal Structure: Polynuclear Aromatic Hydrocarbon. *J. Chem. Soc., Chem. Commun.* **1989**, *10*, 621−623 and references therein.

(5) Watson, M. D.; Fechtenkoetter, A.; Muellen, K. Big Is Beautiful—Aromaticity Revisited from the Viewpoint of Macromolecular and Supramolecular Benzene Chemistry. *Chem. Rev.* **2001**, *101*, 1267−1300.

(6) Hoeben, F. J. M.; Jonkheijm, P.; Meijer, E. W.; Schenning, A. P. H. J. About Supramolecular Assemblies of π-Conjugated Systems. *Chem. Rev.* **2005**, *105*, 1491−1546.

(7) Abraham, R. J.; Eivazi, F.; Pearson, H.; Smith, K. M. $\pi-\pi$ Aggregation in Metalloporphyrins: Causative Factors. *J. Chem. Soc., Chem. Commun.* **1976**, 699−701.

(8) Adam, D.; Schuhmacher, P.; Simmerer, J.; Häussling, L.; Siemensmeyer, K.; Etzbachi, K.; Ringsdorf, H.; Haarer, D. Fast Photoconduction in the Highly Ordered Columnar Phase of a Discotic Liquid Crystal. *Nature (London)* **1994**, *371*, 141−143.

(9) Percec, V.; Glodde, M.; Bera, T.; Miura, Y.; Shiyanovskaya, I.; Singer, K.; Balagurusamy, V.; Heiney, P.; Schnell, I.; Rapp, A.; et al. Self-Organization of Supramolecular Helical Dendrimers into Complex Electronic Materials. *Nature (London)* **2002**, *419*, 384−387.

(10) Chen, Z.; Stepanenko, V.; Dehm, V.; Prins, P.; Siebbeles, L. D.; Seibt, J.; Marquetand, P.; Engel, V.; Würthner, F. Photoluminescence and Conductivity of Self-Assembled $\pi-\pi$ Stacks of Perylene Bisimide Dyes. *Chem.—Eur. J.* **2007**, *13*, 436−449.

(11) Liu, R.; Wu, D.; Feng, X.; Müllen, K. Bottom-Up Fabrication of Photoluminescent Graphene Quantum Dots with Uniform Morphology. *J. Am. Chem. Soc.* **2011**, *133*, 15221−15223.

(12) Ohta, T.; Bostwick, A.; Seyller, T.; Horn, K.; Rotenberg, E. Controlling the Electronic Structure of Bilayer Graphene. *Science* **2006**, *313*, 951−954.

(13) Zhang, Y.; Tang, T.-T.; Girit, C.; Hao, Z.; Martin, M. C.; Zettl, A.; Crommie, M. F.; Shen, Y. R.; Wang, F. Direct Observation of a Widely Tunable Bandgap in Bilayer Graphene. *Nature (London)* **2009**, *459*, 820−823.

(14) Mak, K. F.; Lui, C. H.; Shan, J.; Heinz, T. F. Observation of an Electric-Field-Induced Band Gap in Bilayer Graphene by Infrared Spectroscopy. *Phys. Rev. Lett.* **2009**, *102*, 256405.

(15) Hass, J.; De Heer, W.; Conrad, E. The Growth and Morphology of Epitaxial Multilayer Graphene. *J. Phys.: Condens. Matter* **2008**, *20*, 323202.

(16) Jiao, L.; Zhang, L.; Wang, X.; Diankov, G.; Dai, H. Narrow Graphene Nanoribbons from Carbon Nanotubes. *Nature (London)* **2009**, *458*, 877.

(17) Kosynkin, D. V.; Higginbotham, A. L.; Sinitskii, A.; Lomeda, J. R.; Dimiev, A.; Price, B. K.; Tour, J. M. Longitudinal Unzipping of Carbon Nanotubes To Form Graphene Nanoribbons. *Nature (London)* **2009**, *458*, 872.

(18) Jiao, L.; Wang, X.; Diankov, G.; Wang, H.; Dai, H. Facile Synthesis of High-Quality Graphene Nanoribbons. *Nat. Nanotechnol.* **2010**, *5*, 321−325.

(19) Barone, V.; Hod, O.; Scuseria, G. E. Electronic Structure and Stability of Semiconducting Graphene Nanoribbons. *Nano Lett.* **2006**, *6*, 2748−2754.

(20) Son, Y.-W.; Cohen, M. L.; Louie, S. G. Energy Gaps in Graphene Nanoribbons. *Phys. Rev. Lett.* **2006**, *97*, 216803.

(21) Pisani, L.; Chan, J. A.; Montanari, B.; Harrison, N. M. Electronic Structure and Magnetic Properties of Graphitic Ribbons. *Phys. Rev. B* **2007**, *75*, 064418.

(22) Prezzi, D.; Varsano, D.; Ruini, A.; Marini, A.; Molinari, E. Optical Properties of Graphene Nanoribbons: The Role of Many-Body Effects. *Phys. Rev. B* **2008**, *77*, 041404(R).

(23) Prezzi, D.; Varsano, D.; Ruini, A.; Molinari, E. Quantum Dot States and Optical Excitations of Edge-Modulated Graphene Nanoribbons. *Phys. Rev. B* **2011**, *84*, 041401.

(24) Yang, L.; Cohen, M.; Louie, S. Excitonic Effects in the Optical Spectra of Graphene Nanoribbons. *Nano Lett.* **2007**, *7*, 3112−3115.

(25) Cocchi, C.; Ruini, A.; Prezzi, D.; Caldas, M. J.; Molinari, E. Designing All-Graphene Nanojunctions by Covalent Functionalization. *J. Phys. Chem. C* **2011**, *115*, 2969−2973.

(26) Genorio, B.; Znidarsic, A. Functionalization of Graphene Nanoribbons. *J. Phys. D: Appl. Phys.* **2014**, *47*, 094012.

(27) Zhu, X.; Su, H. Excitons of Edge and Surface Functionalized Graphene Nanoribbons. *J. Phys. Chem. C* **2010**, *114*, 17257−17262.

(28) Wagner, P.; Ewels, C.; Adjizian, J.-J.; Magaud, L.; Pochet, P.; Roche, S.; Lopez-Bezanilla, A.; Ivanovskaya, V.; Yaya, A.; Rayson, M.; et al. Band Gap Engineering via Edge Functionalisation of Graphene Nanoribbons. *J. Phys. Chem. C* **2013**, *117*, 26790.

(29) Jippo, H.; Ohfuchi, M. First-Principles Study of Edge-Modified Armchair Graphene Nanoribbons. *J. Appl. Phys.* **2013**, *113*, 183715.

(30) Vo, T. H.; Shekhirev, M.; Kunkel, D. A.; Morton, M. D.; Berglund, E.; Kong, L.; Wilson, P. M.; Dowben, P. A.; Enders, A.; Sinitskii, A. Large-Scale Solution Synthesis of Narrow Graphene Nanoribbons. *Nat. Commun.* **2014**, *5*, 3189.

(31) Kharche, N.; Zhou, Y.; O'Brien, K. P.; Kar, S.; Nayak, S. K. Effect of Layer Stacking on the Electronic Structure of Graphene Nanoribbons. *ACS Nano* **2011**, *5*, 6096−6101.

(32) Feng, C.; Lin, C. S.; Fan, W.; Zhang, R. Q.; Van Hove, M. A. Stacking of Polycyclic Aromatic Hydrocarbons as Prototype for Graphene Multilayers, Studied Using Density Functional Theory Augmented with a Dispersion Term. *J. Chem. Phys.* **2009**, *131*, 194702.

(33) Lima, M. P.; Fazzio, A.; da Silva, A. J. R. Edge Effects in Bilayer Graphene Nanoribbons: Ab Initio Total-Energy Density Functional Theory Calculations. *Phys. Rev. B* **2009**, *79*, 153401.

(34) González, J. W.; Santos, H.; Pacheco, M.; Chico, L.; Brey, L. Electronic Transport through Bilayer Graphene Flakes. *Phys. Rev. B* **2010**, *81*, 195406.

(35) Sahu, B.; Min, H.; Banerjee, S. K. Effects of Magnetism and Electric Field on the Energy Gap of Bilayer Graphene Nanoflakes. *Phys. Rev. B* **2010**, *81*, 045414.

(36) Gundra, K.; Shukla, A. Band Structure and Optical Absorption in Multilayer Armchair Graphene Nanoribbons: A Pariser−Parr−Pople Model Study. *Phys. Rev. B* **2011**, *84*, 075442.

(37) Wright, A. R.; Cao, J. C.; Zhang, C. Enhanced Optical Conductivity of Bilayer Graphene Nanoribbons in the Terahertz Regime. *Phys. Rev. Lett.* **2009**, *103*, 207401.

(38) Shemella, P.; Zhang, Y.; Mailman, M.; Ajayan, P.; Nayak, S. Energy Gaps in Zero-Dimensional Graphene Nanoribbons. *Appl. Phys. Lett.* **2007**, *91*, 042101.

(39) Hod, O.; Barone, V.; Scuseria, G. E. Half-Metallic Graphene Nanodots: A Comprehensive First-Principles Theoretical Study. *Phys. Rev. B* **2008**, *77*, 035411.

(40) Nakada, K.; Fujita, M.; Dresselhaus, G.; Dresselhaus, M. S. Edge State in Graphene Ribbons: Nanometer Size Effect and Edge Shape Dependence. *Phys. Rev. B* **1996**, *54*, 17954.

(41) The structures considered here are approximately 24 Å long and less than 10 Å wide.

(42) Ridley, J.; Zerner, M. An Intermediate Neglect of Differential Overlap Techinique for Spectroscopy: Pyrrole and the Azines. *Theor. Chem. Acta* **1973**, *32*, 111−134.

(43) Kwasniewski, S. P.; Deleuze, M. S.; Francois, J. P. Optical Properties of *trans*-Stilbene Using Semi-Empirical and Time-Dependent Density Functional Theory: A Comparative Study. *Int. J. Quantum Chem.* **2000**, *80*, 672.

(44) Lopata, K.; Reslan, R.; Kowalska, M.; Neuhauser, D.; Govind, N.; Kowalski, K. Excited-State Studies of Polyacenes: A Comparative Picture Using EOMCCSD, CR-EOMCCSD(T), Range-Separated (LR/RT)-TDDFT, TD-PM3, and TD-ZINDO. *J. Chem. Theory Comput.* **2011**, *7*, 3686.

(45) Wetmore, S. D.; Boyd, R. J.; Eriksson, L. A. Electron Affinities and Ionization Potentials of Nucleotide Bases. *Chem. Phys. Lett.* **2000**, *322*, 129−135.

(46) Caldas, M. J.; Pettenati, E.; Goldoni, G.; Molinari, E. Tailoring of Light Emission Properties of Functionalized Oligothiophenes. *Appl. Phys. Lett.* **2001**, *79*, 2505−2507.

(47) Dávila, L. Y. A.; Caldas, M. J. Applicability of MNDO Techniques AM1 and PM3 to Ring-Structured Polymers. *J. Comput. Chem.* **2002**, *23*, 1135.

(48) Kubatkin, S.; Danilov, A.; Hjort, M.; Cornil, J.; Brédas, J.; Stuhr-Hansen, N.; Hedegård, P.; Bjørnholm, T. Single-Electron Transistor of a Single Organic Molecule with Access to Several Redox States. *Nature (London)* **2002**, *32*, 567−569.

(49) Machado, A.; Munaro, M.; Martins, T.; Davila, L.; Giro, R.; Caldas, M.; Atvars, T.; Akcelrud, L. Photoluminescence Studies of Phenanthrene−Azomethyne Conjugated−Nonconjugated Multiblock Copolymer. *Macromolecules* **2006**, *39*, 3398−3407.

(50) Dewar, M. J. S.; Zoebish, E. G.; Healy, E. F.; Stewart, J. J. P. A New General Purpose Quantum Mechanical Molecular Model. *J. Am. Chem. Soc.* **1985**, *107*, 3902−3909.

(51) Perdew, J. P.; Burke, K.; Ernzerhof, M. Generalized Gradient Approximation Made Simple. *Phys. Rev. Lett.* **1996**, *77*, 3865−3868.

(52) Grimme, S. Semiempirical GGA-Type Density Functional Constructed with a Long-Range Dispersion Correction. *J. Comput. Chem.* **2006**, *27*, 1787−1799.

(53) Giannozzi, P.; Baroni, S.; Bonini, N.; Calandra, M.; Car, R.; Cavazzoni, C.; Ceresoli, D.; Charotti, G. L.; Cococcioni, M.; Dabo, I.; et al. Quantum ESPRESSO: A Modular and Open-Source Software Project for Quantum Simulations of Materials. *J. Phys.: Condens. Matter* **2009**, *21*, 395502. See also http://www.quantum-espresso.org.

(54) Barone, V.; Casarin, M.; Forrer, D.; Pavone, M.; Sambi, M.; Vittadini, A. Role and Effective Treatment of Dispersive Forces in Materials: Polyethylene and Graphite Crystals as Test Cases. *J. Comput. Chem.* **2009**, *30*, 934−939.

(55) By comparing PBE-D2 and AM1 optimized geometries for the single GNFs, we find small differences in bond lengths (the largest

difference being 0.025 Å) that induce a slight lowering of optical excitation energies,[60] which however does not affect the overall results.

(56) ZINDO/S calculations are performed using a LCAO basis set, the INDO/1 Hamiltonian, and the Mataga−Nishimoto scheme to evaluate Coulomb integrals, as implemented in the VAMP module included in the Accelrys Materials Studio software, version 6.0 (http://accelrys.com/products/materials-studio). The validation of the ZINDO scheme with respect to ab initio approaches was presented in many previous works (e.g., see refs 43 and 44), while it was discussed in ref 62 for the specific graphene flakes addressed here.

(57) Cocchi, C.; Prezzi, D.; Ruini, A.; Caldas, M.; Molinari, E. Optical Properties and Charge-Transfer Excitations in Edge-Functionalized All-Graphene Nanojunctions. *J. Phys. Chem. Lett.* **2011**, *2*, 1315−1319.

(58) Jensen, F. *Introduction to Computational Chemistry*, 2nd ed.; Wiley: Hoboken, NJ, 2007.

(59) Sahu, B.; Min, H.; MacDonald, A. H.; Banerjee, S. K. Energy Gaps, Magnetism, and Electric-Field Effects in Bilayer Graphene Nanoribbons. *Phys. Rev. B* **2008**, *78*, 045404.

(60) Cocchi, C.; Prezzi, D.; Ruini, A.; Caldas, M. J.; Molinari, E. Electronics and Optics of Graphene Nanoflakes: Edge Functionalization and Structural Distortions. *J. Phys. Chem. C* **2012**, *116*, 17328−17335.

(61) Milko, M.; Puschnig, P.; Blondeau, P.; Menna, E.; Gao, J.; Loi, M. A.; Draxl, C. Evidence of Hybrid Excitons in Weakly Interacting Nanopeapods. *J. Phys. Chem. Lett.* **2013**, *4*, 2664−2667.

(62) Cocchi, C.; Prezzi, D.; Ruini, A.; Benassi, E.; Caldas, M. J.; Corni, S.; Molinari, E. Optical Excitations and Field Enhancement in Short Graphene Nanoribbons. *J. Phys. Chem. Lett.* **2012**, *3*, 924−929.

Marzio De Corato,[*,†,‡] Caterina Cocchi,[‡] Alice Ruini,[*,†,‡] Deborah Prezzi,[‡] Marilia J. Caldas,[¶] and Elisa Molinari[†,‡]

Dipartimento di Scienze Fisiche, Informatiche, Matematiche, Università di Modena e Reggio Emilia, I-41125 Modena, Italy, Centro S3, CNR-Istituto Nanoscienze, I-41125 Modena, Italy, and Instituto de Física, Universidade de São Paulo, 05508-900 São Paulo, SP, Brazil

E-mail: marzio.decorato@unimore.it; alice.ruini@unimore.it

---

[*] To whom correspondence should be addressed

[†] Dipartimento di Scienze Fisiche, Informatiche, Matematiche, Università di Modena e Reggio Emilia, I-41125 Modena, Italy

[‡] Centro S3, CNR-Istituto Nanoscienze, I-41125 Modena, Italy

[¶] Instituto de Física, Universidade de São Paulo, 05508-900 São Paulo, SP, Brazil

Abstract

Keywords: ZINDO, AM1, substitution, UV-vis spectrum, graphene nanoribbons, configuration interaction

This Supporting Info is organized as follows: the first section provides the optical absorption results for additional biflake structures, that are obtained by stacking two 7H flakes wih different relative shifts along their main axis; the frontier orbitals for all the GNFs that are employed to build the biflake configurations investigated in this paper are shown in the second section; the last section reports the details of the UV-VIS spectra which are not provided in the main text.

Effects of the overlap area on the optical properties

In order to understand the relationship between the π-coupling effect and the area the overlap region, we investigated additional configurations for the homogeneous stacking of the 7H flakes, where the symmetry is maintained (α-like stacking) but different relative displacements are considered; we therefore address the 7H-7H α' and 7H-7H α'' configurations (see Fig. Figure 1a-b), where the flakes are displaced by four and eight C-C bond lengths, respectively, along the x direction. In Fig. Figure 1c we compare the absorption spectra of α, α' and α'' BGNFs. For the α' system, we observe that the peak position is only slightly blueshifted compared to the considerable reduction of overlap area. By further increasing the displacement (α''), we find that the energy position of the first peak tends to blueshift back toward the value of the isolated 7H GNF and the oscillator strenght increases toward two times the value of the isolated 7H GNF, both effects indicating an almost negligible coupling in this latter case.

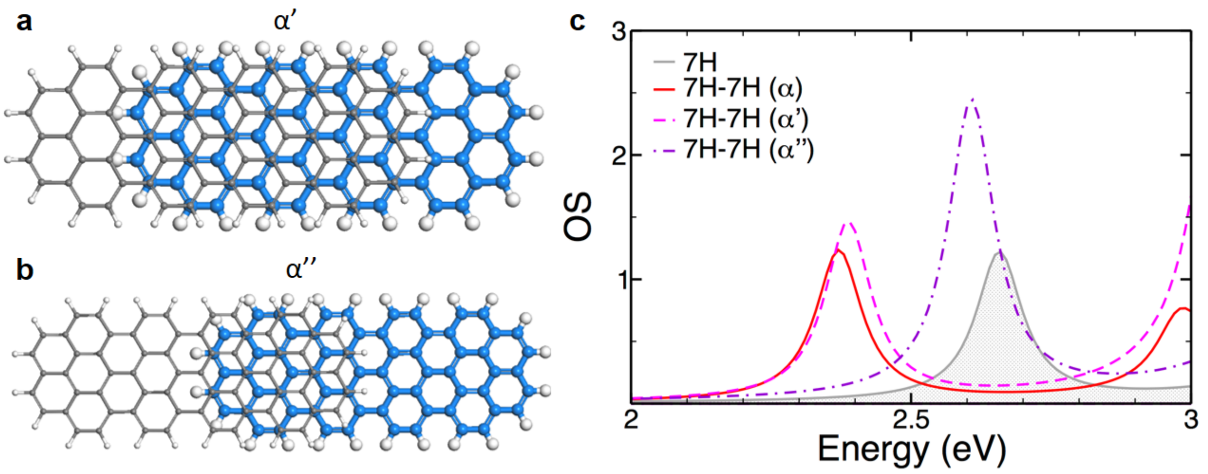

Figure 1: (a,b) Ball-and-stick model of the 7H-7H BGNFs obtained by combining two $N = 7$ GNFs in Bernal stacking, in the α configuration, and shifting one flake by four C-C bond lengths along the x axis with respect to the other one (α') and by eight bond lengths along the x axis with respect to the other one (α''). (c) The absorption spectra obtained for different relative shifts of the flakes composing the α configuration, namely α' (dashed magenta) and α'' (dot-dashed violet). The spectra were obtained by using a Lorentzian broadening of 50 meV.

Frontier orbitals

The frontier orbitals of the biflakes investigated in this work (see main text) are shown in Fig. Figure 2. In the case of the homogeneos stacking, the charge density is equally distributed on the two (identical) flakes, while in the case of the heterogeneous stacking this is not the case: according to the picture emerging from the calculation of electron affinity and ionization potential, we find that for the 7H-8H BGNF both HOMO (HOMO-1) and LUMO (LUMO+1) states are more localized on the 8H (7H) flake, while the electron distribution associated to HOMO and HOMO-1 (LUMO and LUMO+1) is more pronounced on the 7H (7F) flake in the case of the 7H-7F BGNF.

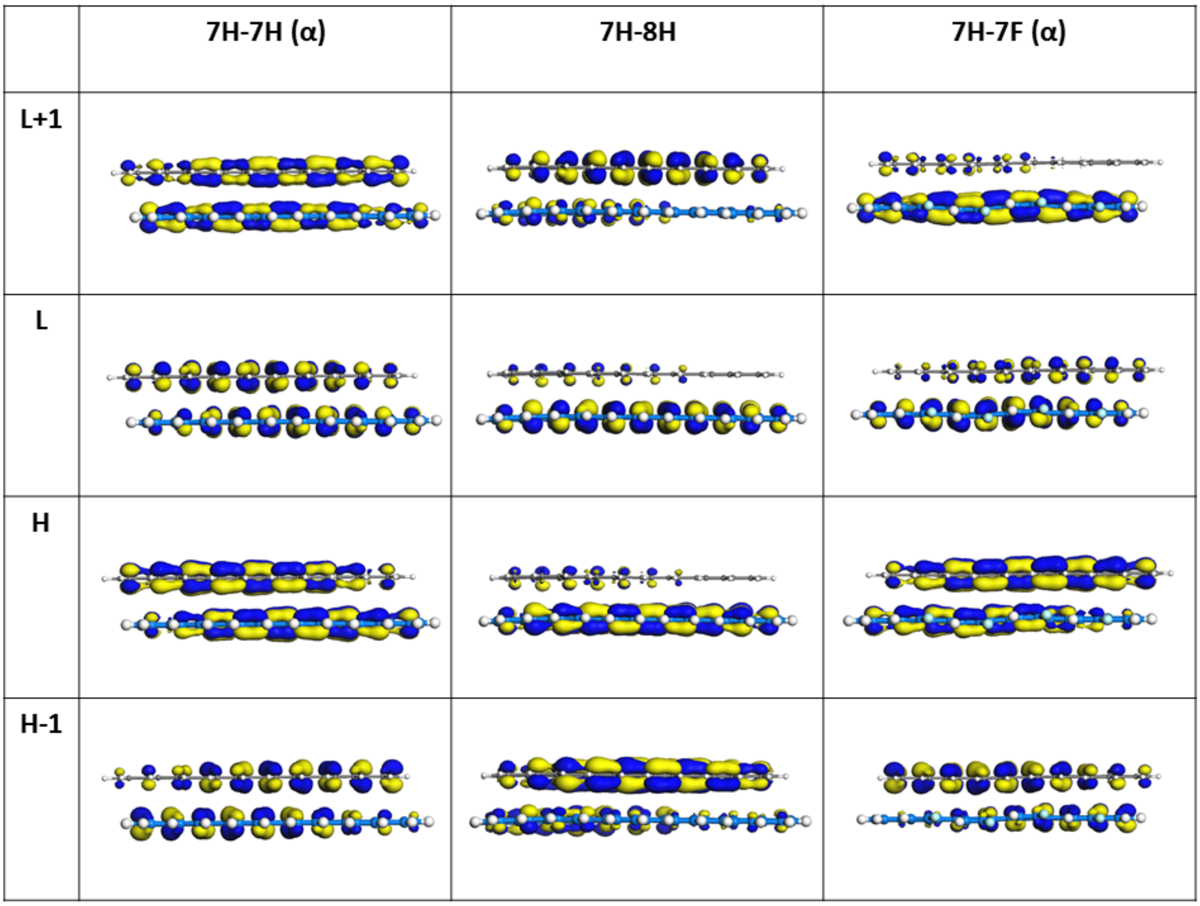

Figure 2: Frontier orbitals for the 7H-7H α, 7H-8H and 7H-7F α bilayer graphene nanoflakes.

Details of the UV-VIS spectra

We report in Table Table 1 the contribution to the most prominent low-energy optical excitations for the 7H-7H β BGNF.

Table 1: Low energy optical excitations (I) of the 7H-7H (β) BGNF: energy (E, in eV), oscillator strength (OS), CI coefficients ($C_{\alpha\beta}$) of relevant transitions ($C_{\alpha\beta} \geq 0.1$), and the projections of the transition dipole moment (μ, in D) in the GNF plane (xy plane, $\mu_{\|}$), and perpendicular to it (z direction, $\mu_{\perp}$).

I	E	OS	$C_{\alpha\beta}$	$\mu_{\|}$	$\mu_{\perp}$
1	2.31	0.00	(0.32) H-1 → L (0.27) H → L+1	0.00	0.00
2	2.44	0.04	(0.19) H-2 → L+1 (0.19) H-1 → L+2 (0.20) H → L+3	1.99	-0.47
3	2.45	0.00	(0.33) H-1 → L (0.44) H → L+1	0.00	0.00
4	2.51	0.73	(0.13) H-1 → L+1 (0.63) H → L	8.65	-1.41
19	3.29	4.14	(0.31) H-2 → L+1 (0.28) H-1 → L+2	18.11	1.74

The optical absorption spectrum for the 7H-7F β BGNFs is reported in Fig. Table 2 and the details of the corresponding excitations are provided in Table Table 2. As for the 7H-7H β BGNF,, a redshift can be recognized also for the 7H-7F β BGNF. This shift, however, is less pronounced with respect to the α case reported in the main text. It is worth noting that in both cases the first active peak is preceded by three dark excitations. Finally, as for the α case, the functionalization with -F seems to enhance the charge transfer character of the excitations.

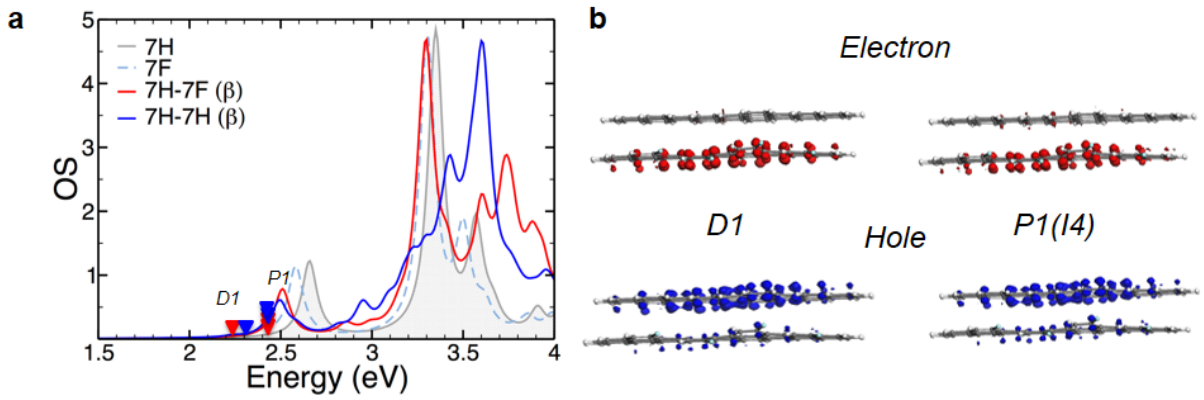

Figure 3: Properties the β configuration: (a) absorption spectra for the 7H-7F and 7H-7H BGNFs in the β (dashed blue) configuration compared to the one of the isolated 7H (grey area) and 7F (dashed light blue) GNF . (b) probability densities of the electrons (red) and holes (blue) for the two first excitations (D1,D2) of 7H-7F (β) BGNF. For the spectra we use a Lorentzian broadening of 50 meV.

Table 2: Low energy optical excitations (I) of the 7H-7F (β) BGNF: energy (E, in eV), oscillator strength (OS), CI coefficients ($C_{\alpha\beta}$) of relevant transitions ($C_{\alpha\beta} \geq 0.1$), and the projections of the transition dipole moment (μ, in D) in the GNF plane (xy plane, $\mu_{\parallel}$), and perpendicular to it (z direction, $\mu_{\perp}$).

I	E	OS	$C_{\alpha\beta}$		$\mu_{\parallel}$	$\mu_{\perp}$	L_e^{7F}	L_h^{7F}	CT
1	2.23	0.02	(0.15) (0.44)	H-1→L H→L	1.58	-0.45	0.79	0.34	0.45
2	2.41	0.06	(0.15) (0.11) (0.16)	H-1→L H-1→L+2 H→L+4	2.62	0.34	0.57	0.41	0.16
3	2.43	0.02	(0.11) (0.15) (0.15) (0.13)	H-2→L H-1→L H-1→L+1 H→L+2	1.47	0.24	0.70	0.45	0.25
4	2.49	0.52	(0.32) (0.14) (0.30)	H-1→L H→L H→L+1	7.28	1.39	0.72	0.33	0.39
5	2.58	0.11	(0.24) (0.30)	H→L H→L+1	3.38	0.59	0.68	0.24	0.44
34	3.60	2.90	(0.18)	H-2→L+4	14.55	0.21	0.48	0.41	0.09

6 LATTICE DYNAMICS OF 2D GRAPHENE/H-BN SUPERLATTICES

The superlattices represent one of the oldest and well-know technique for the realization of quantum confinement. This approach was widely exploited in the past for several bulk semiconductors [85, 24]. As reviewed in Section 1.4 this method was recently re-proposed for 2D systems; however, although many theoretical studies were dedicated to the investigation of the electronic structure of 2D superlattices, little is known about their vibrational properties. In this chapter we are going to present the main results of our theoretical investigation (still in progress) concerning the lattice dynamics of h-BN/Gr superlattices, where we consider both armchair and zig-zag interfaces as shown in Fig. 6.1 .

6.1 COMPUTATIONAL METHODS AND SYSTEM DESCRIPTION

Calculations were performed within the density functional theory (DFT) and the density functional perturbation theory [10] (DFPT), as described in Chapter 3 and implemented in the Quantum-Espresso suite of codes [50]. The local density approximation (LDA) was choosen for the exchange-correlation functional. Norm conserving pseudopotentials were employed, with a plane-wave cutoff energy of 80 Ry. A vacuum region of 12 Å in the non periodic directions was introduced to prevent interaction between periodic images. The atomic positions were fully relaxed until forces were less than 5×10^{-4} a.u. The BZ of the heterojunctions was sampled with a 2×16×1 k-point Monkhorst-Pack grid [86]. We characterize the vibrational properties of two types of superlattices where the interface is along the zig-zag or armchair direction, respectively: the first superlattice is formed by the junction of a 6ZGNR and a 6ZBNNR; the second is composed by the repetition of a 6AGNR

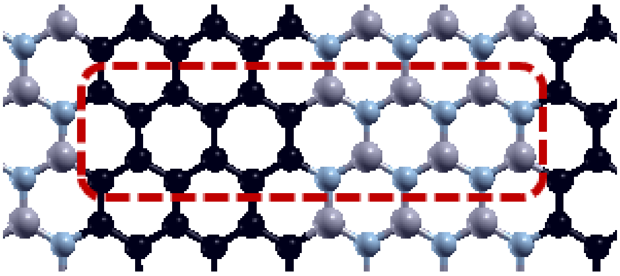

6AGNNR/6ABNNR

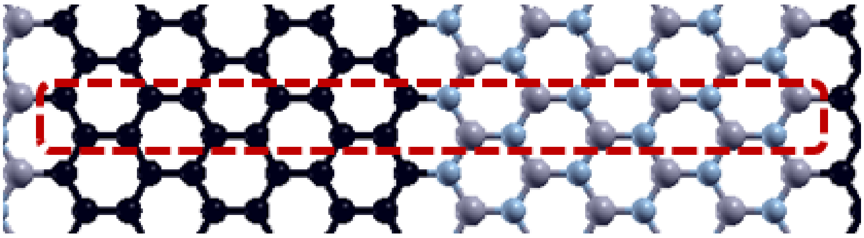

6ZGNR/6ZBNNR

Figure 6.1.: The heterojunctions investigated in this paper: such 2D superlattices can be seen as a combination of two armchair/zig-zag nanoribbons composed by graphene and by h-BN. The respective unitary cells are highlighted with a dashed red line.

and a 6ABNNR. The systems under investigation are shown in Fig. 6.1.

6.2 RESULTS

6ZGNR/6ZBNNR We start our discussion from the longitudinal (L) modes: as shown in Figure 6.2, the LO branches of graphene and h-BN present two gaps. However, these cover two different frequency ranges that do not overlap: as a consequence, no longitudinal interface modes are present in the heterojunction [24, 85]. Some localized modes are instead present in the frequency range 1574 – 1654 cm^{-1} where three non dispersive bands appear in the graphene region (LO_1: 1604 cm^{-1}; LO_2: 1624 cm^{-1}; LO_3: 1626 cm^{-1}), in view of the different ranges spanned by the LO branches in the two materials. All the other longitudinal modes are extended over the whole heterojunction.

The situation for the transverse polarization is rather different: as shown in Fig 6.3, the TO branches of graphene and of h-BN cover two different regions that are not overlapping (h-BN: $1282 - 1385\ \text{cm}^{-1}$; Gr: $1445 - 1611\ \text{cm}^{-1}$). This implies that all the optical modes are localized either on the h-BN component or on the graphene component. However only the highest two ones (TO_3: $1433\ \text{cm}^{-1}$; TO_2: $1421\ \text{cm}^{-1}$) have displacements typical of interfaces modes [24, 85], while the lowest one (TO_1: $1405\ \text{cm}^{-1}$) is unequivocally localized on h-BN. This behaviour is due to the fact that the lattice parameter of h-BN in the heterostructure is smaller with respect to the bulk material [1] . Consequently, the transversal bands of the h-BN are slightly blue-shifted (see solid vs dashed lines for the dispersion computed with the ideal lattice parameter and the lattice parameter obtained in the junction, respectively) and this reduces the gap enough to exclude the mode TO_1. For graphene no significant modifications of the band are instead found.

As we move to the z polarization, we note that the graphene and h-BN branches have partially overlapping gaps which can again give rise to interface modes. As reported in Fig 6.4 only one interface mode is present in this region (ZO_1: $609\ \text{cm}^{-1}$) that involves the B-C bond. One would expect in principle to find also an interface mode related to the N-C bond at a different frequency, being the two interfaces inequivalent. However, the frequency of the latter is expected to be lower since the mass M of N atom is larger with respect to the B one: a first evaluation of the difference between the frequencies ν of these two bonds can be obtained using the relation:

$$\frac{\nu_{C-N}}{\nu_{C-B}} \simeq \frac{\sqrt{M_B}}{\sqrt{M_N}} \tag{6.1}$$

According to this evaluation the frequency of the N-C bond is about $500\ \text{cm}^{-1}$, value that is close to the lower limit of the vibrational gap.

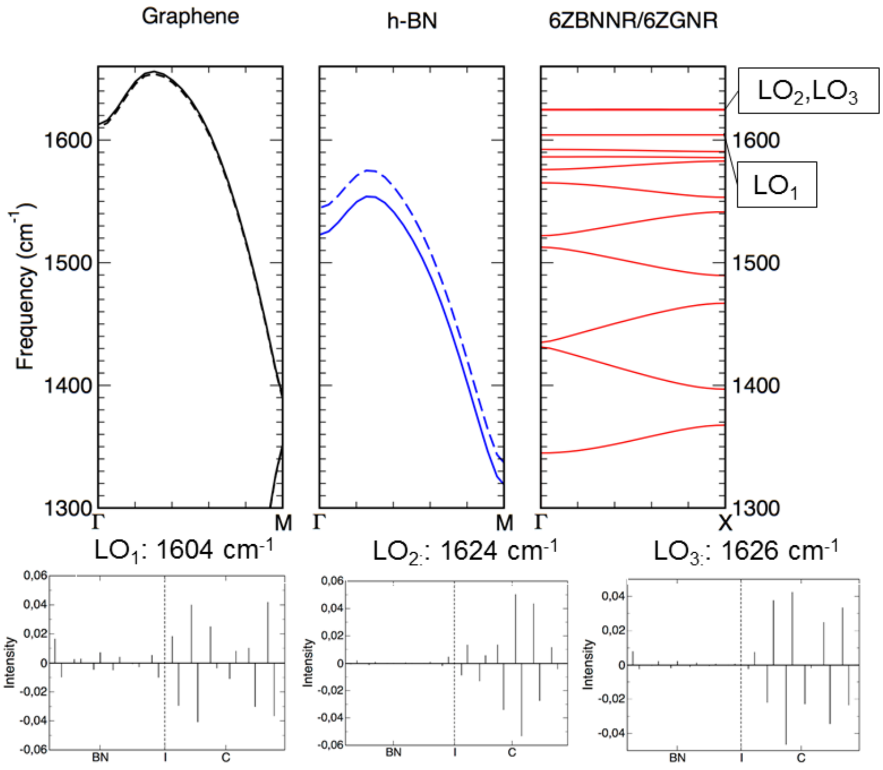

Figure 6.2.: The highest energy part of the longitudinal branches of graphene and of h-BN compared with the longitudinal phonon dispersion of the 6ZGNR/6ZBNNR heterojunction: despite the presence of vibrational gaps in the branches of the bulk materials, no interface mode can be present due to the fact that the gaps are not overlapping; however three localized modes are present (two of them are very close in energy), since the 1574 – 1654 cm^{-1} interval is covered only by the graphene dispersion: this produces the non-dispersive mode LO$_1$,LO$_2$ and LO$_3$ that are localized in the graphene region (see the lowest panel). The dashed lines represent the longitudinal branches of strained graphene and of strained h-BN, obtained with bulk calculations where we imposed the lattice parameter of the heterostructure components [1]

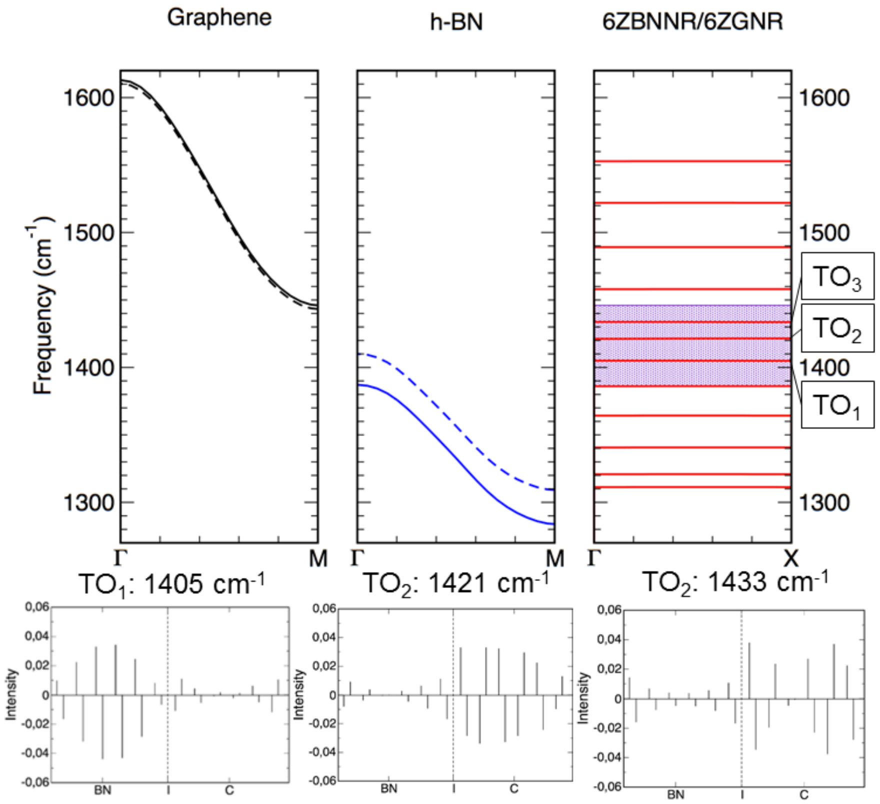

Figure 6.3.: The highest energy part of the transverse branches of graphene and of h-BN compared with the transverse phonon dispersion of the 6ZGNR/6ZBNNR heterostructure: in this case the bands of graphene and of h-BN cover two different frequency intervals (respectively $1445 - 1611$ cm^{-1} and $1282 - 1385$ cm^{-1}) that are not overlapping; as a consequence there is a forbidden frequency range where the interface modes can be present . Concerning the 6ZGNR/6ZBNNR heterojunction, three modes lie within this interval TO$_1$, TO$_2$ and TO$_3$(their displacements are reported in the lower panels): while the TO$_2$ and TO$_3$ modes have displacements that are typical of an interface mode, the TO$_1$ mode is clearly a localized mode in the h-BN lattice. This localized behaviour is explained if one considers the phonon dispersion of a strained h-BN (dashed lines) [1] . As for the longitudinal modes, this effect is negligible for the graphene dispersion.

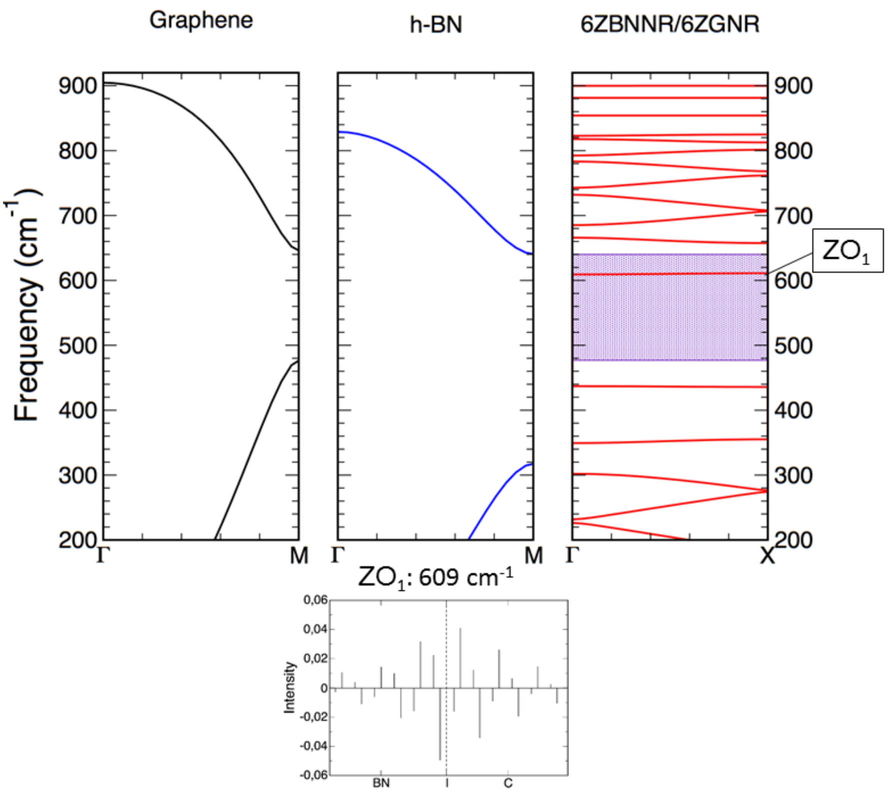

Figure 6.4.: The z branches of graphene and of the h-BN compared with the z phonon dispersion of the 6ZGNR/6ZBNNR heterostructure: in this case the vibrational gap of graphene and of h-BN are overlapping: one interface mode (ZO$_1$) of the heterostructure in this overlap region, whose displacement is reported in the lower panel.

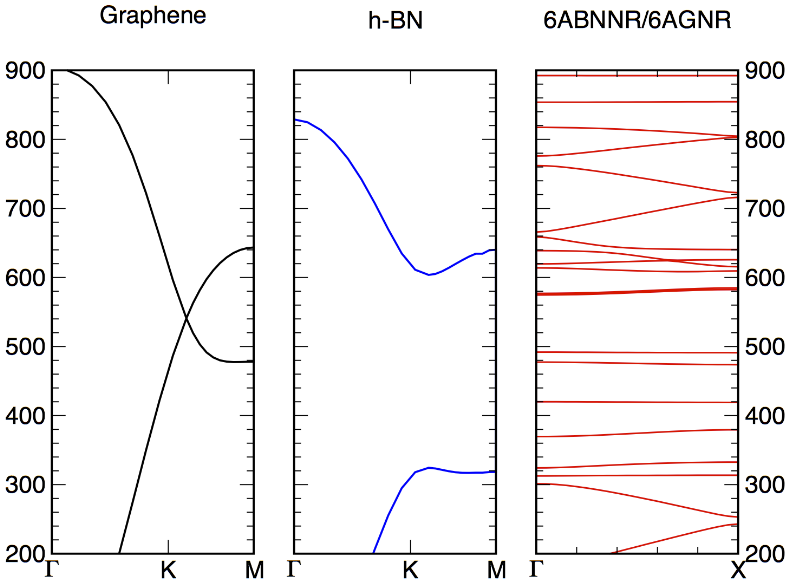

Figure 6.5.: The phonon dispersion polarized along the Z axis for graphene, h-BN and 6AGNR/6ABNNR. Note that, since no gap is present in the phonon disperison of graphene, no interface mode is allowed.

6AGNR/6ABNNR In Figure 6.6 the longitudinal and transverse phonon bands dispersions of graphene and h-BN are reported along the Γ**KM** path corresponding to the armchair interface. While no overlapping gaps are present for the LO and ZO branches, one appears in the TO case (1008 – 1200 cm^{-1}). As a consequence, one expects some transverse interface modes in this region. However, looking to the phonon dispersion of the heterostructure, no flat bands are found in the overlapping range, as confirmed also by the analysis of the displacements. The explanation of this behaviour lies on the fact that the gap modes are located close to the **K** point, where they have an hybrid longitudinal/transverse character. Since the longitudinal component is allowed for any frequency in graphene, the longitudinal component of the hybrid gap modes can propagate in graphene: this excludes the presence of the transverse interface modes which are thus not present at all in the armchair junction.

Raman spectrum of 6AGNR/6ABNNR Contrary to the zig-zag heterostructure, we are able to calculate the Raman spectrum

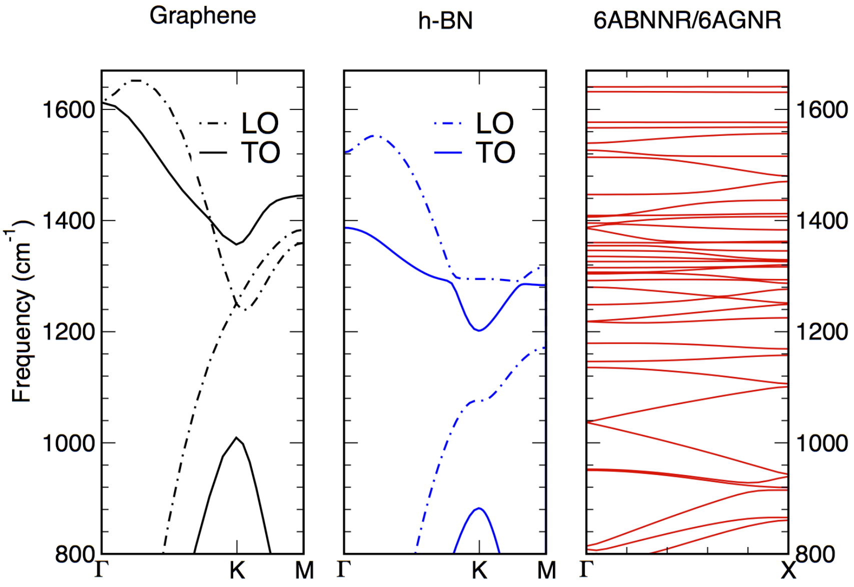

Figure 6.6.: The longitudinal (dashed line) and transverse (solid line) phonon band structure of graphene and of h-BN compared to the phonon dispersion of the heterostructure 6AGNR/6ABNNR: due to the fact near **K** the vibrational modes are not purely longitudinal or transversal and no gap is present in the longitudinal branches of graphene no interface mode is allowed

from first principles for the armchair system (see Fig 6.7): at a first sight we note the presence of the D_c and G_c peaks which are characteristic of a carbon armchair system (see Chapter 1) together with the G_{BN} peak of h-BN [46, 55]; these peaks correspond to longitudinal optical displacements localized respectively in the carbon and in h-BN components without any node (0-LO) . In addition to these peaks, which are characteristic of the bulk materials, further ones appears as result of the h-BN/graphene coupling: the G_{ext} peak, in which the whole heterostructure has a displacement close to the 0-LO mode, and then a peak close to the D_{ext} peak, whose displacement resembles the ring-stretching mode.
Moving to the lower part of the spectrum (inset of Fig 6.7), we can see a very intense peak at 451 cm^{-1}: from its displacement we can attribute it to the radial-like breathing mode (RLBM) of both nanoribbons, which in this case have almost the same width. As shown in Chapter 1, the frequency of this mode can be used to predict the width for each component of the junction:

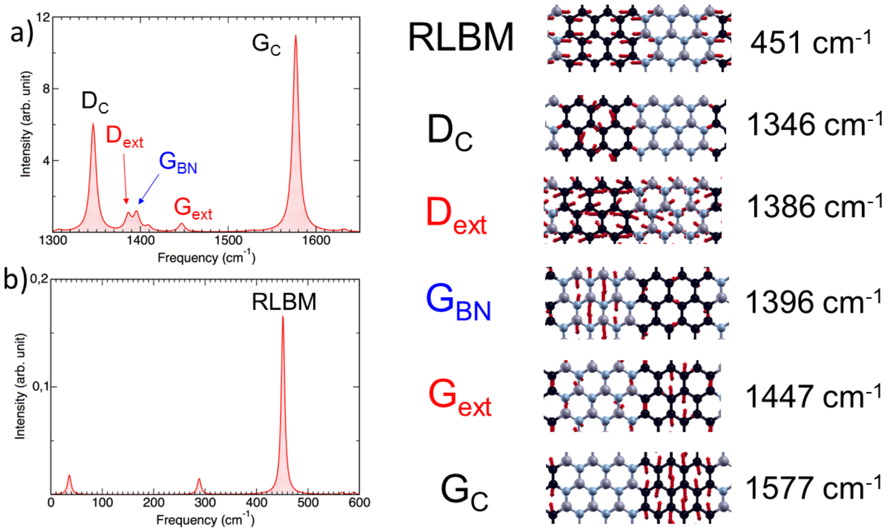

Figure 6.7.: The optical (upper panel) and acoustical (lower panel) raman spectrum of the heterostructure 6AGNR/6ABNNR accompained by the displacement and the energy of the most important peaks

in our case, according to Eq. 1.15, we find a width of 7.14 Å which differs only by 0.21Å with respect to the carbon component and only by 0.26 Å with respect to the h-BN component. It is worth noting that also for the 6ZGNR/6ZBNNR system this mode is present: in this case the predicted width is 11.89 Å value which differs by 0.89 Å with respect to the carbon component and by 1.06 Å with respect to the h-BN component. A detailed analysis of the RLBM of these heterostructure will be the subject of further investigations.

6.3 SUMMARY

We investigate with ab-initio techniques the vibrational properties of h-BN/graphene superlattices with both armchair and zig-zag interfaces: we find that, while for the zigzag case three interface modes are allowed (T: 1434 and 1421 cm^{-1}; Z: 609 cm^{-1}), for the armchair case they are not present. The analysis of the Raman spectrum of the armchair heterostructure showed that this is not only composed by the modes connected to the armchair bulk lattice (D_c and G_c for graphene and G_{BN} for h-BN) but it is also formed by two modes which are produced by the coupling of these 2D lattices (D_{ext} and G_{ext}). It is worth stressing that the presence of the D peak is the easiest marker of the presence of an armchair junction, since it is not allowed in the zig-zag case. Furthermore a prediction of the width of the heterostructure components can be obtained using the frequency of the RLBM as for isolated nanoribbons. We plan to continue this work by investigating the phonon band dispersion and the Raman spectrum of other 2D superlattices such as those composed by different TMDCs.

CONCLUSIONS

This thesis work was devoted to the computational study of different graphene-based nanostructures. Specifically, the following open issues were addressed: a) the interpretation of the Raman and infrared spectra of GNRs with different edge morphologies, b) the effects of π-π coupling on the UV-VIS spectra for elongated armchair graphene nanoflakes, c) the lattice dynamics of 2D superlattices composed by the alternation of h-BN and graphene stripes. Concerning the point b) different coupled systems were considered: these included two identical nanoflakes staked in different configurations, two nanoflakes with different widths and two identical nanoflakes with different functionalizations. From our calculations, based on the HF semi-empirical methods, we point out that the UV-VIS absorption spectrum as well as the charge transfer excitonic phenomena can be tuned by properly choosing the nanoflakes that compose the macromolecular system. As, for issue (a) the Raman and IR vibrational spectra of GNRs were investigated in collaboration with different experimental groups. Our ab-initio calculations on the Raman spectra of GNRs obtained by our experimental collaborators show that the different low energy peaks, especially the radial-like breathing mode (RLBM), are very sensitive to the edge morphology as well as to the edge functionalization. For these nanostructures the well known ZF method that links the width of a purely zig-zag or armchair GNR with the frequency of RLBM does not hold anymore. We then proposed a model through which we are able to correctly consider the role of the edge morphology as well as of the alkyl chains attached at the edges. Through different ab-initio calculations, we also interpret the experimental IR spectra of the same GNRs. Finally, concerning the current work (c) on 2D superlattices, we find that the interface modes are allowed only for the zig-zag junction.

APPENDIX A: THE ROOHTHAAN-HALL EQUATIONS

The HF equation 3.15 are in a integro-differential form: consequently, in order to be solved with the standard techniques, a matrix form is highly suitable. This task was performed independently by Roothaan [110] and by Haal [56] in 1951. For this purpose the spin-orbitals are developed in to a basis of atomic orbitals ϕ_ν according to the linear combination of atomic orbitals (LCAO) approach [74]:

$$f_i(1)\sum_{\nu=1}^{K} c_{\nu i}\phi_\nu(1) = \epsilon_i \sum_{\nu=1}^{K} c_{\nu i}\phi_\nu(1) \tag{A.1}$$

Through some manipulations this last expression can be rewritten as [74]

$$\sum_{\nu=1}^{K} c_{\nu 1}\int dv_1\phi_\mu(1)f_i(1)\phi_\nu(1) = \epsilon_i \sum_{\nu=1}^{K} c_{\nu 1}\int dv_1\phi_\mu(1)\phi_\nu(1) \tag{A.2}$$

where the Fock matrix element [74]

$$F_{\mu\nu} = \int dv_1\phi_\mu(1)f_i(1)\phi_\nu(1) \tag{A.3}$$

can be recast as [74]

$$F_{\mu\nu} = H_{\mu\nu}^{core} + \sum_{\lambda=1}^{K}\sum_{\lambda=1}^{K} P_{\lambda\sigma}\left[(\mu\nu|\lambda\sigma) - \frac{1}{2}(\mu\lambda|\nu\sigma)\right] \tag{A.4}$$

in which [74]

$$P_{\mu\nu} = 2\sum_{i=1}^{N/2} c_{\mu i}c_{\nu i} \tag{A.5}$$

is the charge density polarization matrix. Once defined these quantities the Eq. A.2 can be written as [74]

$$\mathbf{FC} = \mathbf{SCE} \tag{A.6}$$

where [74]

$$\mathbf{C} = \begin{pmatrix} c_{1,1} & c_{1,2} & \dots & c_{1,K} \\ c_{2,1} & c_{2,2} & \dots & c_{1,K} \\ \vdots & \vdots & & \vdots \\ c_{K,1} & c_{K,2} & \dots & c_{K,K} \end{pmatrix} \tag{A.7}$$

$$\mathbf{E} = \begin{pmatrix} \epsilon_1 & 0 & \dots & 0 \\ 0 & \epsilon_1 & \dots & 0 \\ \vdots & \vdots & & \vdots \\ 0 & 0 & \dots & \epsilon_K \end{pmatrix} \tag{A.8}$$

$$\mathbf{S}_{\mu\nu} = \int d\nu_1 \phi_\mu(1)\phi_\nu(1) \tag{A.9}$$

Since the usual diagonalization techniques require the standard form $\mathbf{FC} = \mathbf{CE}$ a further manipulation is needed: this goal can be achieved if the quantities in the Eq. A.6 are rearranged as follows [74] :

$$\begin{aligned} \mathbf{F'C'} =& \mathbf{C'E} \\ \mathbf{F'} =& \mathbf{S}^{-1/2}\mathbf{FS}^{1/2} \\ \mathbf{C'} =& \mathbf{S}^{1/2}\mathbf{C} \end{aligned} \tag{A.10}$$

SEMI-EMPIRICAL METHODS The evaluation of all the matrix elements in Eq. A.4 is very demanding from a computational viewpoint; a common strategy to reduce this price is first to neglect some of them (especially the ones in which many centers are involved), then to parametrize the remaining ones using, for example, the atomic spectroscopic data. This is the idea of the semiempirical methods. The toll paid in this parametrization is that they can be used only for a restricted class of solid/-molecules. It is worth noting that some common approximations for these methods are introduced: first only the valence electrons are taken in to account and second, the overlap matrix $\mathbf{S}$ is put equal to the identity matrix. This last approximation makes Eq. A.6 ready for the diagonalization. A full review on these methods can be found in [60, 74]

BIBLIOGRAPHY

[1] The lattice parameters of h-BN (graphene) inside the heterostructure were calculated by evaluating the distance between two hexagonal unit cells in the middle of h-BN (graphene) strips.

[2] Phonons tutorial shanghai. `http://www.quantum-espresso.org/wp-content/uploads/2013/06/phonons_tutorial_shanghai1.pdf`.

[3] Vibrational Spectroscopy. `http://www.chemie-biologie.uni-siegen.de/ac/be/lehre/ws1213/ir-ramanlong.pdf`.

[4] T. Aizawa, R. Souda, S. Otani, Y. Ishizawa, and C. Oshima. Anomalous bond of monolayer graphite on transition-metal carbide surfaces. *Phys. Rev. Lett.*, 64:768–771, Feb 1990.

[5] Takashi Aizawa, Ryutaro Souda, Yoshio Ishizawa, Hideki Hirano, Taro Yamada, Ken ichi Tanaka, and Chuhei Oshima. Phonon dispersion in monolayer graphite formed on ni(111) and ni(001). *Surface Science*, 237(1):194 – 202, 1990.

[6] Andreas C. Albrecht. On the theory of raman intensities. *The Journal of Chemical Physics*, 34(5), 1961.

[7] Matthew J. Allen, Vincent C. Tung, and Richard B. Kaner. Honeycomb carbon: A review of graphene. *Chemical Reviews*, 110(1):132–145, 2010. PMID: 19610631.

[8] Phaedon Avouris. Graphene: Electronic and photonic properties and devices. *Nano Letters*, 10(11):4285–4294, 2010. PMID: 20879723.

[9] Stefano Baroni. Density functional perturbational theory. `http://stefano.baroni.me/presentations_files/Minneapolis2006-DFPT.pdf`.

[10] Stefano Baroni, Stefano de Gironcoli, Andrea Dal Corso, and Paolo Giannozzi. Phonons and related crystal properties from density-functional perturbation theory. *Rev. Mod. Phys.*, 73:515–562, Jul 2001.

[11] Axel D. Becke. Density-functional thermochemistry. i. the effect of the exchange-only gradient correction. *The Journal of Chemical Physics*, 96(3), 1992.

[12] G. Benedek, G. Brusdeylins, C. Heimlich, J.P. Toennies, and U. Valbusa. Surface phonons in graphite (001). *Surface Science*, 178(1-3):545–552, 1986.

[13] P.F. Bernath. *Spectra of Atoms and Molecules*. Oxford University Press, 2005.

[14] X. Blase, Angel Rubio, Steven G. Louie, and Marvin L. Cohen. Quasiparticle band structure of bulk hexagonal boron nitride and related systems. *Phys. Rev. B*, 51:6868–6875, Mar 1995.

[15] M. Born and K. Huang. *Dynamical Theory of Crystal Lattices*. International series of monographs on physics. Clarendon Press, 1998.

[16] G. Breit. Quantum theory of dispersion. *Rev. Mod. Phys.*, 4:504–576, Jul 1932.

[17] L. Brey and H. A. Fertig. Electronic states of graphene nanoribbons studied with the dirac equation. *Phys. Rev. B*, 73:235411, Jun 2006.

[18] P. Brüesch. *Phonons, theory and experiments*. Number v. 1 in Phonons, Theory and Experiments. Springer-Verlag, 1982.

[19] Sheneve Z. Butler, Shawna M. Hollen, Linyou Cao, Yi Cui, Jay A. Gupta, Humberto R. GutiÃľrrez, Tony F. Heinz, Seung Sae Hong, Jiaxing Huang, Ariel F. Ismach, Ezekiel Johnston-Halperin, Masaru Kuno, Vladimir V. Plashnitsa, Richard D. Robinson, Rodney S. Ruoff, Sayeef Salahuddin, Jie Shan, Li Shi, Michael G. Spencer, Mauricio Terrones, Wolfgang Windl, and Joshua E. Goldberger. Progress, challenges, and opportunities in two-dimensional materials beyond graphene. *ACS Nano*, 7(4):2898–2926, 2013. PMID: 23464873.

[20] Jinming Cai, Pascal Ruffieux, Rached Jaafar, Marco Bieri, Thomas Braun, Stephan Blankenburg, Matthias Muoth, Ari P. Seitsonen, Moussa Saleh, Xinliang Feng, Klaus Mullen, and Roman Fasel. Atomically precise bottom-up fabrication of graphene nanoribbons. *Nature*, 466(7305):470–473, 07 2010.

[21] L. G. Cancado, A. Jorio, E. H. Martins Ferreira, F. Stavale, C. A. Achete, R. B. Capaz, M. V. O. Moutinho, A. Lombardo, T. S. Kulmala, and A. C. Ferrari. Quantifying defects in graphene via raman spectroscopy at different excitation energies. *Nano Letters*, 11(8):3190–3196, 2011. PMID: 21696186.

[22] L. G. Cancado, M. A. Pimenta, B. R. A. Neves, M. S. S. Dantas, and A. Jorio. Influence of the atomic structure on the raman spectra of graphite edges. *Phys. Rev. Lett.*, 93:247401, Dec 2004.

[23] Abraham G. Cano-Marquez, Fernando J. Rodriguez-Macias, Jessica Campos-Delgado, Claudia G. Espinosa-Gonzalez, Ferdinando TristÃąn-Lopez, Daniel Ramirez-GonzÃąlez, David A. Cullen, David J. Smith, Mauricio Terrones, and Yadira I. Vega-Cantu. Ex-mwnts: Graphene sheets and ribbons produced by lithium intercalation and exfoliation of carbon nanotubes. *Nano Letters*, 9(4):1527–1533, 2009.

[24] M. Cardona. Folded, confined, interface, surface, and slab vibrational modes in semiconductor superlattices. *Superlattices and Microstructures*, 5(1):27 – 42, 1989.

[25] Manuel Cardona and Y Yu Peter. *Fundamentals of semiconductors*. Springer, 2005.

[26] C. Casiraghi, A. Hartschuh, H. Qian, S. Piscanec, C. Georgi, A. Fasoli, K. S. Novoselov, D. M. Basko, and A. C. Ferrari. Raman spectroscopy of graphene edges. *Nano Letters*, 9(4):1433–1441, 2009. PMID: 19290608.

[27] A. H. Castro Neto, F. Guinea, N. M. R. Peres, K. S. Novoselov, and A. K. Geim. The electronic properties of graphene. *Rev. Mod. Phys.*, 81:109–162, Jan 2009.

[28] Andrea Centrone, Luigi Brambilla, Thierry Renouard, Lileta Gherghel, Claude Mathis, Klaus Mullen, and

Giuseppe Zerbi. Structure of new carbonaceous materials: The role of vibrational spectroscopy. *Carbon*, 43(8):1593 – 1609, 2005.

[29] Manish Chhowalla, Hyeon Suk Shin, Goki Eda, Lain-Jong Li, Kian Ping Loh, and Hua Zhang. The chemistry of two-dimensional layered transition metal dichalcogenide nanosheets. *Nat Chem*, 5(4):263–275, 04 2013.

[30] Lijie Ci, Li Song, Chuanhong Jin, Deep Jariwala, Dangxin Wu, Yongjie Li, Anchal Srivastava, ZF Wang, Kevin Storr, Luis Balicas, et al. Atomic layers of hybridized boron nitride and graphene domains. *Nature materials*, 9(5):430–435, 2010.

[31] Caterina Cocchi, Deborah Prezzi, Alice Ruini, Enrico Benassi, Marilia J. Caldas, Stefano Corni, and Elisa Molinari. Optical excitations and field enhancement in short graphene nanoribbons. *The Journal of Physical Chemistry Letters*, 3(7):924–929, 04 2012.

[32] Caterina Cocchi, Deborah Prezzi, Alice Ruini, Marilia J. Caldas, and Elisa Molinari. Optical properties and charge-transfer excitations in edge-functionalized all-graphene nanojunctions. *The Journal of Physical Chemistry Letters*, 2(11):1315–1319, 2011. PMID: 26295427.

[33] Caterina Cocchi, Deborah Prezzi, Alice Ruini, Marilia J. Caldas, and Elisa Molinari. Electronics and optics of graphene nanoflakes: Edge functionalization and structural distortions. *The Journal of Physical Chemistry C*, 116(33):17328–17335, 2012.

[34] Caterina Cocchi, Alice Ruini, Deborah Prezzi, Marilia J. Caldas, and Elisa Molinari. Designing all-graphene nanojunctions by covalent functionalization. *The Journal of Physical Chemistry C*, 115(7):2969–2973, 2011.

[35] Chunxiao Cong, Ting Yu, Riichiro Saito, Gene F. Dresselhaus, and Mildred S. Dresselhaus. Second-order overtone and combination raman modes of graphene layers in the range of 1690-2150 cm-1. *ACS Nano*, 5(3):1600–1605, 2011. PMID: 21344883.

[36] E. de Rouffignac, G. P. Alldredge, and F. W. de Wette. Lattice dynamics of graphite slabs. *Phys. Rev. B*, 23:4208–4219, Apr 1981.

[37] D. P. DiVincenzo and E. J. Mele. Self-consistent effective-mass theory for intralayer screening in graphite intercalation compounds. *Phys. Rev. B*, 29:1685–1694, Feb 1984.

[38] VL. Dumitrescu. The prehistory of romania from the earliest times to 1000 b.c. In John Boardman, I. E. S. Edwards, N. G. L. Hammond, and E. Sollberger, editors, *The Cambridge Ancient History*, volume 3, Part 1, pages 1–74. Cambridge University Press, second edition, 1982. Cambridge Histories Online.

[39] Sudipta Dutta and Swapan K. Pati. Novel properties of graphene nanoribbons: a review. *J. Mater. Chem.*, 20:8207–8223, 2010.

[40] Ana Laura Elias, Andres R. Botello-Mendez, David Meneses-Rodriguez, Viviana Jehova Gonzalez, Daniel Ramirez-Gonzalez, Lijie Ci, Emilio Munoz-Sandoval, Pulickel M. Ajayan, Humberto Terrones, and Mauricio Terrones. Longitudinal cutting of pure and doped carbon nanotubes to form graphitic nanoribbons using metal clusters as nanoscalpels. *Nano Letters*, 10(2):366–372, 2010. PMID: 19691280.

[41] A. Fasolino, J. H. Los, and M. I. Katsnelson. Intrinsic ripples in graphene. *Nat Mater*, 6(11):858–861, 11 2007.

[42] A. C. Ferrari, J. C. Meyer, V. Scardaci, C. Casiraghi, M. Lazzeri, F. Mauri, S. Piscanec, D. Jiang, K. S. Novoselov, S. Roth, and A. K. Geim. Raman spectrum of graphene and graphene layers. *Phys. Rev. Lett.*, 97:187401, Oct 2006.

[43] Andrea C. Ferrari and Denis M. Basko. Raman spectroscopy as a versatile tool for studying the properties of graphene. *Nat Nano*, 8(4):235–246, 04 2013.

[44] R. P. Feynman. Forces in molecules. *Phys. Rev.*, 56:340–343, Aug 1939.

[45] Y. Gamo, A. Nagashima, M. Wakabayashi, M. Terai, and C. Oshima. Atomic structure of monolayer graphite formed on ni(111). *Surface Science*, 374(1-3):61 – 64, 1997.

[46] R. Geick, C. H. Perry, and G. Rupprecht. Normal modes in hexagonal boron nitride. *Phys. Rev.*, 146:543–547, Jun 1966.

[47] AK Geim and IV Grigorieva. Van der waals heterostructures. *Nature*, 499(7459):419–425, 2013.

[48] Andre K Geim and Konstantin S Novoselov. The rise of graphene. *Nature materials*, 6(3):183–191, 2007.

[49] P. Giannozzi. An introduction to linear response and to phonon calculations. `http://www.fisica.uniud.it/~giannozz/QE-Tutorial/tutorial_phon.pdf`.

[50] Paolo Giannozzi, Stefano Baroni, Nicola Bonini, Matteo Calandra, Roberto Car, Carlo Cavazzoni, Davide Ceresoli, Guido L Chiarotti, Matteo Cococcioni, Ismaila Dabo, Andrea Dal Corso, Stefano de Gironcoli, Stefano Fabris, Guido Fratesi, Ralph Gebauer, Uwe Gerstmann, Christos Gougoussis, Anton Kokalj, Michele Lazzeri, Layla Martin-Samos, Nicola Marzari, Francesco Mauri, Riccardo Mazzarello, Stefano Paolini, Alfredo Pasquarello, Lorenzo Paulatto, Carlo Sbraccia, Sandro Scandolo, Gabriele Sclauzero, Ari P Seitsonen, Alexander Smogunov, Paolo Umari, and Renata M Wentzcovitch. Quantum espresso: a modular and open-source software project for quantum simulations of materials. *Journal of Physics: Condensed Matter*, 21(39):395502, 2009.

[51] Roland Gillen, Marcel Mohr, and Janina Maultzsch. Raman-active modes in graphene nanoribbons. *physica status solidi (b)*, 247(11-12):2941–2944, 2010.

[52] Roland Gillen, Marcel Mohr, and Janina Maultzsch. Symmetry properties of vibrational modes in graphene nanoribbons. *Phys. Rev. B*, 81:205426, May 2010.

[53] Roland Gillen, Marcel Mohr, Christian Thomsen, and Janina Maultzsch. Vibrational properties of graphene nanoribbons by first-principles calculations. *Phys. Rev. B*, 80:155418, Oct 2009.

[54] Gianluca Giovannetti, Petr A. Khomyakov, Geert Brocks, Paul J. Kelly, and Jeroen van den Brink. Substrate-induced band gap in graphene on hexagonal boron nitride: *Ab initio* density functional calculations. *Phys. Rev. B*, 76:073103, Aug 2007.

[55] Roman V. Gorbachev, Ibtsam Riaz, Rahul R. Nair, Rashid Jalil, Liam Britnell, Branson D. Belle, Ernie W. Hill,

Kostya S. Novoselov, Kenji Watanabe, Takashi Taniguchi, Andre K. Geim, and Peter Blake. Hunting for monolayer boron nitride: Optical and raman signatures. *Small*, 7(4):465–468, 2011.

[56] G. G. Hall. The molecular orbital theory of chemical valency. viii. a method of calculating ionization potentials. *Proceedings of the Royal Society of London A: Mathematical, Physical and Engineering Sciences*, 205(1083):541–552, 1951.

[57] P. Hohenberg and W. Kohn. Inhomogeneous electron gas. *Phys. Rev.*, 136:B864–B871, Nov 1964.

[58] Sacha Hony. *Infrared light on the composition of the dust surrounding carbon-rich stars*. Amsterdam University Press, 2003.

[59] Deep Jariwala, Vinod K. Sangwan, Lincoln J. Lauhon, Tobin J. Marks, and Mark C. Hersam. Emerging device applications for semiconducting two-dimensional transition metal dichalcogenides. *ACS Nano*, 8(2):1102–1120, 2014. PMID: 24476095.

[60] F. Jensen. *Introduction to Computational Chemistry*. Wiley, 2007.

[61] Xiaoting Jia, Jessica Campos-Delgado, Mauricio Terrones, Vincent Meunier, and Mildred S. Dresselhaus. Graphene edges: a review of their fabrication and characterization. *Nanoscale*, 3:86–95, 2011.

[62] Liying Jiao, Li Zhang, Xinran Wang, Georgi Diankov, and Hongjie Dai. Narrow graphene nanoribbons from carbon nanotubes. *Nature*, 458(7240):877–880, 04 2009.

[63] A. Jorio, M.S. Dresselhaus, R. Saito, and G. Dresselhaus. *Raman Spectroscopy in Graphene Related Systems*. Wiley, 2011.

[64] Mikhail I. Katsnelson. Graphene: carbon in two dimensions. *Materials Today*, 10(1-2):20 – 27, 2007.

[65] Keun Soo Kim, Yue Zhao, Houk Jang, Sang Yoon Lee, Jong Min Kim, Kwang S. Kim, Jong-Hyun Ahn, Philip Kim, Jae-Young Choi, and Byung Hee Hong. Large-scale pattern growth of graphene films for stretchable transparent electrodes. *Nature*, 457(7230):706–710, 02 2009.

[66] W. Kohn. Image of the fermi surface in the vibration spectrum of a metal. *Phys. Rev. Lett.*, 2:393–394, May 1959.

[67] W. Kohn and L. J. Sham. Self-consistent equations including exchange and correlation effects. *Phys. Rev.*, 140:A1133–A1138, Nov 1965.

[68] Anton Kokalj. Xcrysden-a new program for displaying crystalline structures and electron densities. *Journal of Molecular Graphics and Modelling*, 17(3-4):176 – 179, 1999.

[69] Dmitry V. Kosynkin, Amanda L. Higginbotham, Alexander Sinitskii, Jay R. Lomeda, Ayrat Dimiev, B. Katherine Price, and James M. Tour. Longitudinal unzipping of carbon nanotubes to form graphene nanoribbons. *Nature*, 458(7240):872–876, 04 2009.

[70] A. Kuc, N. Zibouche, and T. Heine. Influence of quantum confinement on the electronic structure of the transition metal sulfide ts_2. *Phys. Rev. B*, 83:245213, Jun 2011.

[71] Konstantin N. Kudin, Bulent Ozbas, Hannes C. Schniepp, Robert K. Prud'homme, Ilhan A. Aksay, and Roberto Car. Raman spectra of graphite oxide and functionalized graphene sheets. *Nano Letters*, 8(1):36–41, 2008. PMID: 18154315.

[72] LD Landau. Zur theorie der phasenumwandlungen ii. *Phys. Z. Sowjetunion*, 11:26–35, 1937.

[73] Michele Lazzeri and Francesco Mauri. First-principles calculation of vibrational raman spectra in large systems: Signature of small rings in crystalline sio_2. *Phys. Rev. Lett.*, 90:036401, Jan 2003.

[74] Andrew R. Leach. *Molecular Modelling: Principles and Applications*. Prentice Hall, 2001.

[75] Xiaolin Li, Xinran Wang, Li Zhang, Sangwon Lee, and Hongjie Dai. Chemically derived, ultrasmooth graphene nanoribbon semiconductors. *Science*, 319(5867):1229–1232, 2008.

[76] Elliott H. Lieb. Two theorems on the hubbard model. *Phys. Rev. Lett.*, 62:1201–1204, Mar 1989.

[77] Zheng Liu, Lulu Ma, Gang Shi, Wu Zhou, Yongji Gong, Sidong Lei, Xuebei Yang, Jiangnan Zhang, Jingjiang Yu, Ken P. Hackenberg, Aydin Babakhani, Juan-Carlos Idrobo, Robert Vajtai, Jun Lou, and Pulickel M. Ajayan. In-plane heterostructures of graphene and hexagonal boron nitride with controlled domain sizes. *Nat Nano*, 8(2):119—124, 02 2013.

[78] D.A. Long. *The Raman Effect: A Unified Treatment of the Theory of Raman Scattering by Molecules*. Wiley, 2002.

[79] M.M. Lucchese, F. Stavale, E.H. Martins Ferreira, C. Vilani, M.V.O. Moutinho, Rodrigo B. Capaz, C.A. Achete, and A. Jorio. Quantifying ion-induced defects and raman relaxation length in graphene. *Carbon*, 48(5):1592 – 1597, 2010.

[80] D. L. Mafra, G. Samsonidze, L. M. Malard, D. C. Elias, J. C. Brant, F. Plentz, E. S. Alves, and M. A. Pimenta. Determination of la and to phonon dispersion relations of graphene near the dirac point by double resonance raman scattering. *Phys. Rev. B*, 76:233407, Dec 2007.

[81] Richard M. Martin. *Electronic Structure: Basic Theory and Practical Methods*. Cambridge University Press, 2004.

[82] J. Maultzsch, S. Reich, C. Thomsen, H. Requardt, and P. Ordejón. Phonon dispersion in graphite. *Phys. Rev. Lett.*, 92:075501, Feb 2004.

[83] K. H. Michel and B. Verberck. Phonon dispersions and piezoelectricity in bulk and multilayers of hexagonal boron nitride. *Phys. Rev. B*, 83:115328, Mar 2011.

[84] M. Mohr, J. Maultzsch, E. Dobardžić, S. Reich, I. Milošević, M. Damnjanović, A. Bosak, M. Krisch, and C. Thomsen. Phonon dispersion of graphite by inelastic x-ray scattering. *Phys. Rev. B*, 76:035439, Jul 2007.

[85] Elisa Molinari. Phonons and electron-phonon interaction in low-dimensional structures. In Elias Burstein and Claude Weisbuch, editors, *Confined Electrons and Photons*, volume 340 of *NATO ASI Series*, pages 161–203. Springer US, 1995.

[86] Hendrik J. Monkhorst and James D. Pack. Special points for brillouin-zone integrations. *Phys. Rev. B*, 13:5188–5192, Jun 1976.

[87] Angshuman Nag, Kalyan Raidongia, Kailash P. S. S. Hembram, Ranjan Datta, Umesh V. Waghmare, and C. N. R. Rao. Graphene analogues of bn: Novel synthesis and properties. *ACS Nano*, 4(3):1539–1544, 2010. PMID: 20128601.

[88] Ayato Nagashima, Kenji Nuka, Hiroshi Itoh, Takeo Ichinokawa, Chuhei Oshima, and Shigeki Otani. Electronic states of monolayer graphite formed on tic(111) surface. *Surface Science*, 291(1-2):93 – 98, 1993.

[89] Akimitsu Narita, Xinliang Feng, Yenny Hernandez, Søren A. Jensen, Mischa Bonn, Huafeng Yang, Ivan A. Verzhbitskiy, Cinzia Casiraghi, Michael Ryan Hansen, Amelie H. R. Koch, George Fytas, Oleksandr Ivasenko, Bing Li, Kunal S. Mali, Tatyana Balandina, Sankarapillai Mahesh, Steven De Feyter, and Klaus Müllen. Synthesis of structurally well-defined and liquid-phase-processable graphene nanoribbons. *Nat Chem*, 6(2):126–132, 02 2014.

[90] Akimitsu Narita, Ivan A. Verzhbitskiy, Wout Frederickx, Kunal S. Mali, Soeren Alkaersig Jensen, Michael Ryan Hansen, Mischa Bonn, Steven De Feyter, Cinzia Casiraghi, Xinliang Feng, and Klaus Mullen. Bottom-up synthesis of liquid-phase-processable graphene nanoribbons with near-infrared absorption. *ACS Nano*, 8(11):11622–11630, 2014. PMID: 25338208.

[91] R. J. Nemanich, S. A. Solin, and Richard M. Martin. Light scattering study of boron nitride microcrystals. *Phys. Rev. B*, 23:6348–6356, Jun 1981.

[92] A. H. Castro Neto and K. Novoselov. Two-dimensional crystals: Beyond graphene. *Materials Express*, 1(1):10–17, 2011-03-01T00:00:00.

[93] Wataru Norimatsu, Koichiro Hirata, Yuta Yamamoto, Shigeo Arai, and Michiko Kusunoki. Epitaxial growth of boron-doped graphene by thermal decomposition of b 4 c. *Journal of Physics: Condensed Matter*, 24(31):314207, 2012.

[94] K. S. Novoselov, D. Jiang, F. Schedin, T. J. Booth, V. V. Khotkevich, S. V. Morozov, and A. K. Geim. Two-dimensional atomic crystals. *Proceedings of the National Academy of Sciences of the United States of America*, 102(30):10451–10453, 2005.

[95] R. W. Nunes and Xavier Gonze. Berry-phase treatment of the homogeneous electric field perturbation in insulators. *Phys. Rev. B*, 63:155107, Mar 2001.

[96] Silvio Osella, Akimitsu Narita, Matthias Georg Schwab, Yenny Hernandez, Xinliang Feng, Klaus Mullen, and David Beljonne. Graphene nanoribbons as low band gap donor materials for organic photovoltaics: Quantum chemical aided design. *ACS Nano*, 6(6):5539–5548, 2012. PMID: 22631451.

[97] Chuhei Oshima and Ayato Nagashima. Ultra-thin epitaxial films of graphite and hexagonal boron nitride on solid surfaces. *Journal of Physics: Condensed Matter*, 9(1):1, 1997.

[98] Amir Pakdel, Yoshio Bando, and Dmitri Golberg. Nano boron nitride flatland. *Chem. Soc. Rev.*, 43:934–959, 2014.

[99] B. Partoens and F. M. Peeters. From graphene to graphite: Electronic structure around the k point. *Phys. Rev. B*, 74:075404, Aug 2006.

[100] M. C. Payne, M. P. Teter, D. C. Allan, T. A. Arias, and J. D. Joannopoulos. Iterative minimization techniques for *ab initio* total-energy calculations: molecular dynamics and conjugate gradients. *Rev. Mod. Phys.*, 64:1045–1097, Oct 1992.

[101] Rudolf Peierls. Quelques propriétés typiques des corps solides. In *Annales de l'institut Henri Poincaré*, volume 5, pages 177–222, 1935.

[102] Tsvi Piran. *Statistical mechanics of membranes and surfaces*. World Scientific, 2004.

[103] Valerio Pirronello, Jacek Krelowski, and Giulio Manicò. *Solid state astrochemistry*, volume 120. Springer Science & Business Media, 2012.

[104] S. Piscanec, M. Lazzeri, Francesco Mauri, A. C. Ferrari, and J. Robertson. Kohn anomalies and electron-phonon

interactions in graphite. *Phys. Rev. Lett.*, 93:185503, Oct 2004.

[105] Plato, E. Hamilton, and H. Cairns. *The Collected Dialogues of Plato, Including the Letters*. Bollingen Series (General) Series. Princeton University Press, 1961.

[106] J. M. Pruneda. Origin of half-semimetallicity induced at interfaces of c-bn heterostructures. *Phys. Rev. B*, 81:161409, Apr 2010.

[107] DeanC. R., YoungA. F., MericI., LeeC., WangL., SorgenfreiS., WatanabeK., TaniguchiT., KimP., ShepardK. L., and HoneJ. Boron nitride substrates for high-quality graphene electronics. *Nat Nano*, 5(10):722–726, 10 2010.

[108] S. Reich, A. C. Ferrari, R. Arenal, A. Loiseau, I. Bello, and J. Robertson. Resonant raman scattering in cubic and hexagonal boron nitride. *Phys. Rev. B*, 71:205201, May 2005.

[109] Kyle A. Ritter and Joseph W. Lyding. The influence of edge structure on the electronic properties of graphene quantum dots and nanoribbons. *Nat Mater*, 8(3):235–242, 03 2009.

[110] C. C. J. Roothaan. New developments in molecular orbital theory. *Rev. Mod. Phys.*, 23:69–89, Apr 1951.

[111] Angel Rubio. Hybridized graphene: nanoscale patchworks. *Nature materials*, 9(5):379–380, 2010.

[112] S. Hony, C. Van Kerckhoven, E. Peeters, A. G. G. M. Tielens, D. M. Hudgins, and L. J. Allamandola. The ch out−of−plane bending modes of pah molecules in astrophysical environments. *AA*, 370(3):1030–1043, 2001.

[113] Riichiro Saito, Gene Dresselhaus, Mildred S Dresselhaus, et al. *Physical properties of carbon nanotubes*, volume 35. World Scientific, 1998.

[114] E. Scalise. *Vibrational Properties of Defective Oxides and 2D Nanolattices: Insights from First-Principles Simulations*. Springer Theses. Springer International Publishing, 2014.

[115] Frank Schwierz. Graphene transistors. *Nat Nano*, 5(7):487–496, 07 2010.

[116] J. Serrano, A. Bosak, R. Arenal, M. Krisch, K. Watanabe, T. Taniguchi, H. Kanda, A. Rubio, and L. Wirtz. Vibrational properties of hexagonal boron nitride: Inelastic x-ray scattering and *Ab Initio* calculations. *Phys. Rev. Lett.*, 98:095503, Mar 2007.

[117] Susanne Siebentritt, Roland Pues, Karl-Heinz Rieder, and Alexander M. Shikin. Surface phonon dispersion in graphite and in a lanthanum graphite intercalation compound. *Phys. Rev. B*, 55:7927–7934, Mar 1997.

[118] J. C. Slater. The theory of complex spectra. *Phys. Rev.*, 34:1293–1322, Nov 1929.

[119] Caterina Soldano, Ather Mahmood, and Erik Dujardin. Production, properties and potential of graphene. *Carbon*, 48(8):2127 – 2150, 2010.

[120] Young-Woo Son, Marvin L. Cohen, and Steven G. Louie. Energy gaps in graphene nanoribbons. *Phys. Rev. Lett.*, 97:216803, Nov 2006.

[121] Young-Woo Son, Marvin L Cohen, and Steven G Louie. Half-metallic graphene nanoribbons. *Nature*, 444(7117):347–349, 2006.

[122] P. H. Tan, W. P. Han, W. J. Zhao, Z. H. Wu, K. Chang, H. Wang, Y. F. Wang, N. Bonini, N. Marzari, N. Pugno, G. Savini, A. Lombardo, and A. C. Ferrari. The shear mode of multilayer graphene. *Nat Mater*, 11(4):294–300, 04 2012.

[123] Qing Tang and Zhen Zhou. Graphene-analogous low-dimensional materials. *Progress in Materials Science*, 58(8):1244 – 1315, 2013.

[124] Hal Tasaki. The hubbard model - an introduction and selected rigorous results. *Journal of Physics: Condensed Matter*, 10(20):4353, 1998.

[125] Mauricio Terrones. Materials science: Nanotubes unzipped. *Nature*, 458(7240):845–846, 04 2009.

[126] C. Thomsen and S. Reich. Double resonant raman scattering in graphite. *Phys. Rev. Lett.*, 85:5214–5217, Dec 2000.

[127] F. Tuinstra and J. L. Koenig. Raman spectrum of graphite. *The Journal of Chemical Physics*, 53(3), 1970.

[128] P. Umari and Alfredo Pasquarello. Infrared and raman spectra of disordered materials from first principles. *Diamond and Related Materials*, 14(8):1255 – 1261, 2005. {SMAC} '04 Conference Proceeding S.I.Proceedings of the 5th Specialist Meeting on Amorphous Carbon.

[129] David Vanderbilt. Soft self-consistent pseudopotentials in a generalized eigenvalue formalism. *Phys. Rev. B*, 41:7892–7895, Apr 1990.

[130] Pedro Venezuela, Michele Lazzeri, and Francesco Mauri. Theory of double-resonant raman spectra in graphene: Intensity and line shape of defect-induced and two-phonon bands. *Phys. Rev. B*, 84:035433, Jul 2011.

[131] R.P. Vidano, D.B. Fischbach, L.J. Willis, and T.M. Loehr. Observation of raman band shifting with excitation wavelength for carbons and graphites. *Solid State Communications*, 39(2):341 – 344, 1981.

[132] Philip Richard Wallace. The band theory of graphite. *Physical Review*, 71(9):622, 1947.

[133] Qing Hua Wang, Kourosh Kalantar-Zadeh, Andras Kis, Jonathan N. Coleman, and Michael S. Strano. Electronics and optoelectronics of two-dimensional transition metal dichalcogenides. *Nat Nano*, 7(11):699–712, 11 2012.

[134] Xinran Wang and Hongjie Dai. Etching and narrowing of graphene from the edges. *Nat Chem*, 2(8):661–665, 08 2010.

[135] J.L. Wilkes, R.E. Palmer, and R.F. Willis. Phonons in graphite studied by eels. *Journal of Electron Spectroscopy and Related Phenomena*, 44(1):355 – 360, 1987.

[136] F. Withers, O. Del Pozo-Zamudio, A. Mishchenko, A. P. Rooney, A. Gholinia, K. Watanabe, T. Taniguchi, S. J. Haigh, A. K. Geim, A. I. Tartakovskii, and K. S. Novoselov. Light-emitting diodes by band-structure engineering in van der waals heterostructures. *Nat Mater*, 14(3):301—306, 03 2015.

[137] F. Wooten. *Optical properties of solids*. Academic Press, 1972.

[138] Mingsheng Xu, Tao Liang, Minmin Shi, and Hongzheng Chen. Graphene-like two-dimensional materials. *Chemical Reviews*, 113(5):3766–3798, 2013. PMID: 23286380.

[139] Megumi Yamada, Yoshihiro Yamakita, and Koichi Ohno. Phonon dispersions of hydrogenated and dehydrogenated carbon nanoribbons. *Phys. Rev. B*, 77:054302, Feb 2008.

[140] Jun Yan, Yuanbo Zhang, Philip Kim, and Aron Pinczuk. Electric field effect tuning of electron-phonon coupling in graphene. *Phys. Rev. Lett.*, 98:166802, Apr 2007.

[141] Heejun Yang, Jinseong Heo, Seongjun Park, Hyun Jae Song, David H. Seo, Kyung-Eun Byun, Philip Kim, InKyeong Yoo, Hyun-Jong Chung, and Kinam Kim. Graphene barristor, a triode device with a gate-controlled schottky barrier. *Science*, 336(6085):1140–1143, 2012.

[142] M. T. Yin and Marvin L. Cohen. Theory of lattice-dynamical properties of solids: Application to si and ge. *Phys. Rev. B*, 26:3259–3272, Sep 1982.

[143] Yong-Hong Zhao, Feng Yang, Jian Wang, Hong Guo, and Wei Ji. Continuously tunable electronic structure of transition metal dichalcogenides superlattices. *Sci. Rep.*, 5, 02 2015.

[144] Wenpeng Zhu, Hongtao Wang, and Wei Yang. Evolution of graphene nanoribbons under low-voltage electron irradiation. *Nanoscale*, 4:4555–4561, 2012.

ACKNOWLEDGMENT

> Dicebat Bernardus Carnotensis nos esse quasi nanos gigantium humeris insidentes, ut possimus plura eis et remotiora videre, non utique proprii visus acumine, aut eminentia corporis, sed quia in altum subvehimur et extollimur magnitudine gigantea.
>
> John of Salisbury
> (1120-1180)

First of all I would like to express the deepest thanks to the people that during every single day of these three years not only worked with me but also educated me to a better approach in to science and above all in to life: Dr. Deborah Prezzi and Prof. Alice Ruini. I will be always grateful and debtor for their teachings and support. I am really thankful also to prof. Elisa Molinari for her patient teachings about the lattice dynamics and for her fundamental contributions to the overall work. Dr. Caterina Cocchi patiently taught me the theory of semi-empirical methods and how to use them in the Material Studio software; furthermore, together with prof. Marilia Caldas, she kindly supported me in the first part of my Ph.D work where I undertaken the optical properties of graphene nanoflakes. As the foundation makes possible the overall construction, this Ph.D work was also made possible by the people and professors that, previously, provided me the necessary knowledge: first my parents Riccardo e Silvia, then prof. Paolo Bartesaghi and prof. Luca Montecchi that were my high school teachers, finally prof. Giorgio Benedek, prof. Marco Bernasconi and Dr. Ottorino Ori that were my supervisors during my master thesis work. A special thank is also due to all people that here in Modena shared with me this adventure: Dr. Ilaria Siloi, Luca Bursi, Federico Grasselli, Paolo Restuccia, Andrea Beggi and Erfran

Mafakheri. Thanks also to my Milan and Roana friends: Alfonso, Giuseppe (aka Peppe), Federico, Eleonora, Davide, Tommaso, Giacomo, Corrado, Miriam,Giulia, Ylenia, Francesco, Natale, Nerina, Luca, Maria Luisa, Mattia C., Roberto, Chiara B., Mimmo, Caterina, Alessio, Stefano, Chiara C., Claudia, Elisa, Giorgia, Alessandro A., Alessandro C., Matteo, Sofia, Giulio, Mattia F. and Noemi. Finally, and most importantly, I want to thank my girlfriend (and I hope my future wife) Erika Mangano for all her support during these eight years.